Development of Novel Photocatalysts and Co-catalysts for Photocatalytic Conversion of CO_2 by H_2O

Rui PANG

2019

Preface

The use of fossil fuels such as oil and coal has promoted the rapid industrial development, however, with the excessive utilization of fossil energy, it not only caused a shortage of energy storage, but also produced a series of environmental problems, such as atmospheric and marine pollution, and global warming. The International Panel on Climate Change predicted that CO_2 as one of the main greenhouse gases in the atmosphere would reach up to 590 ppm by 2100, and the global mean temperature would rise by 1.9 ºC, which may cause disastrous consequences such as ice melting, rise in sea level, and change of ecosystems. For the sustainable development of human beings, it is urgently needed to mitigate CO_2 emission and produce energy in more environmentally friendly and efficient technique. The capture, storage, and conversion of CO_2 into other useful chemical compounds, such as CO, HCOOH, HCHO, CH_3OH, and CH_4 is considered as one of the promising strategies to solve the above-mentioned problems. Various technologies, such as thermochemical, photoelectrochemical, electrochemical, photochemical, and biological conversion of CO_2 have been developed to reduce CO_2 into chemical feedstocks. Among them, the photocatalytic conversion of CO_2 by H_2O to hydrocarbon fuels at ambient temperature and pressure using solar light (so-called “artificial photosynthesis”) is a promising technique to solve the environmental problems and produce energy without secondary pollution.

Since the discovery of photocatalytic conversion of CO_2 into hydrocarbons over semiconductors under light irradiation in the late 1970s, the technical and theoretical research on the photocatalytic conversion of CO_2 has made great progress after about 40 years of development. However, the photocatalytic efficiencies for the conversion of CO_2 into hydrocarbon fuels are not satisfactory because the reactions of CO_2 reduction by H_2O are uphill reaction processes ($\Delta G > 0$) that need to input high energy due to the stability of CO_2 molecule.

In the present thesis, the author focuses on highly active and selective photocatalytic conversion of CO_2 by H_2O over various heterogeneous catalysts. Particularly, the effects of s on the photocatalytic performance for the conversion of CO_2 were studied. The author developed a Ag-Cr core-shell-structured (Ag@Cr) co-catalyst that modified on the photocatalyst surface could significantly improve the photocatalytic activity and selectivity for the conversion of CO_2 into CO with

H_2O as an electron donor. In the Ag@Cr co-catalyst, Ag acted as an active site for the photocatalytic conversion of CO_2 into CO, and the $Cr(OH)_3{\cdot}xH_2O$ layer on the surface of Ag core increased the CO_2 adsorption and suppressed the backward reaction for the reduction of CO_2 ($CO + O_2 \rightarrow CO_2$). Although the formation rate of CO was not stable during the photoirradiation due to the dissolution of Cr^{3+} in $Ag@Cr/Ga_2O_3$, this loss could be compensated by reloading supplementary Cr^{3+} in $Ag@Cr/Ga_2O_3$. Interestingly, the author found that $Ag/SrNb_2O_6$ nanorods exhibited a high CO formation rate and high selectivity toward CO evolution for the photocatalytic conversion of CO_2 at low CO_2 concentrations, which provides meaningful insight into the practical application of the photocatalytic conversion of CO_2 into other feedstocks.

The studies demonstrated in this thesis were performed at Department of Molecular Engineering, Graduate School of Engineering, Kyoto University from 2015 to 2018 under the supervision of Professor Tsunehiro Tanaka. The author expresses her sincere gratitude to Professor Tsunehiro Tanaka for his exact guidance, suggestive commands, and constructive criticism throughout this work. In addition, the author should make special acknowledgements to Associate Professor Kentaro Teramura for his patient direction, strict and heartwarming advices, careful reviewing of the manuscripts and constant encouragement. Sincere appreciation should go to Associate Professor Saburo Hosokawa for his constructive advices, patient discussion and stimulating comments. The author deeply thanks to Assistant Professor Hiroyuki Asakura for his incisive suggestion, helpful discussions and grateful guidance. Cordial thanks are given to Professor Hisao Yoshida at Kyoto University, Professor Tetsuya Shishido at Tokyo Metropolitan University, Professor Tomoko Yoshida at Osaka City University, Associate Professor Kazuhiko Maeda at Tokyo Institute of Technology, Assistant Professor Tomoaki Takayama at Tokyo Institute of Technology, Assistant Professor Akira Yamamoto at Kyoto University, and Postdoctoral researcher Zheng Wang at Tokyo University for their valuable suggestions and comments at the conferences. The author should express deeply thanks to seniors, Assistant Professor Shoji Iguchi at Tokyo Institute of Technology, Assistant Professor Kosuke Beppu at Ryukoku University, and Postdoctoral researcher Zeai Huang at National Institute of Advanced Industrial Science and Technology (AIST) for their kind advices to experiments, instructive suggestions, and patient discussions when they were in the laboratory led by Professor Tsunehiro Tanaka.

The author thanks Mr. Kazuki Tamai, Mr. Soichi Kikkawa, Ms. Shuying Wang, for their kindhearted helps and discussions in this study. The author also thanks the graduated master course members, Mr. Satoshi Yonekawa, Mr. Ryohei Tada, Mr. Ryusuke Sakai, Mr. Takuya Shibano, Mr. Yousuke Terao, Mr. Yudai Hasegawa, Mr. Hironobu Hayashi, Mr. Raizo Maeda, and Mr. Kazuya Matsuki, Mr. Kazutaka Hori, Mr. Tomoya Ushio, Mr. Shogo Matsumoto, Mr. Akito Demizu, Mr. Kazuho Murakami, and Mr. Tetsuo Onuki, who helped me in the various measurements and experiments, their kind and humor made me feel the warmth of Tanaka lab. The author also thanks Ms. Sumika Yoshizawa, Mr. Shotaro Kidera, Mr. Yuto Nakatani, Mr. Yudai Oshino, Mr. Masaatsu Ishida, Mr. Kenya Onishi, Mr. Hiroyuki Tanaka, Ms. Maho Kirihara, Mr. Chikara Watanabe, Mr. Masashige Morishita, Ms. Sayaka Soma, Mr. Rinsuke Suzuki, Mr. Takahiro Endo, Ms. Kyoto Fujita, and Mr. Ryosuke Yamada for their help and friendship. The author is grateful to Mr. Hiroyuki Tatsumi who has cooperated the photocatalytic conversion of CO_2 over Ag-Cr/Ga_2O_3 in chapter 3 for his diligent opinion and helpful discussions. The author is grateful to all the students who participated in this study. Profound thanks should also give to Secretary Ms. Mami Nishio and Ms. Yuko Yoshitake for their kind aids in official affairs. The author is also grateful to all the members of the laboratory led by Professor Tsunehiro Tanaka.

XAFS measurements in this thesis were performed at a public beamline (BL01B1) at SPring-8 with the approval of JASRI (Proposal No. 2018A1670). The author is grateful to all the staff at SPring-8 for their cooperation and assistance.

Finally, the author sincerely thanks all the family members, particularly her parents for their supporting, understanding, and encouragement. Special thanks should go to the State Scholarship of China Scholarship Council for funding during the doctoral period.

PANG

Kyoto

December 2018

CONTENTS

General introduction

Basic principles of photocatalytic conversion of CO_2 by H_2O

Anthropogenic greenhouse gas emissions since the pre-industrial era have driven large increases in atmospheric concentrations of CO_2, which will have a drastic impact on the global climate, environment, and economy if additional efforts to reduce these emissions are not made.[1] To mitigate CO_2 emissions and address both energy and environmental issues, photocatalytic conversion of CO_2 into other feedstocks such as CO, HCOOH, HCHO, and CH_4 using solar energy (known as artificial photosynthesis) has been considered one of the best strategies.[2, 3]

Since the pioneering work on the photocatalytic conversion of CO_2 to HCOOH and CH_3OH over semiconductors by Halmann[4] and Inoue et al.,[5] semiconductor-based heterogeneous photocatalysts as simple and environmentally friendly photocatalysts have received widespread attention.[6-8] However, the photocatalytic conversion of CO_2 usually requires high energy inputs to activate the linear CO_2 molecule owing to the high C=O bond energy (750 kJ mol^{-1}).[8, 9] Notably, the proton-assisted multi-electron reductions of CO_2 (Eqn. 2–6, vs. normal hydrogen electrode (NHE) at pH 7.00) show much more moderate potential than the one-electron reduction of CO_2 (Eqn. 1, vs. NHE at pH 7.00).[10-12]

$$CO_2 + e^- \rightleftharpoons CO_2^{\cdot -} \qquad E^{o\prime} = -1.85\ V \qquad (1)$$

$$CO_2 + 2H^+ + 2e^- \rightleftharpoons HCOOH \qquad E^{o\prime} = -0.61\ V \qquad (2)$$

$$CO_2 + 2H^+ + 2e^- \rightleftharpoons CO + H_2O \qquad E^{o\prime} = -0.52\ V \qquad (3)$$

$$CO_2 + 4H^+ + 4e^- \rightleftharpoons HCHO + H_2O \qquad E^{o\prime} = -0.48\ V \qquad (4)$$

$$CO_2 + 6H^+ + 6e^- \rightleftharpoons CH_3OH + H_2O \qquad E^{o\prime} = -0.38\ V \qquad (5)$$

$$CO_2 + 8H^+ + 8e^- \rightleftharpoons CH_4 + 2H_2O \qquad E^{o\prime} = -0.24\ V \qquad (6)$$

$$2H_2O + 4h^+ \rightleftharpoons O_2 + 4H^+ \qquad E^{o\prime} = +0.82\ V \qquad (7)$$

$$2H^+ + 2e^- \rightleftharpoons H_2 \qquad E^{o\prime} = -0.41\ V \qquad (8)$$

Band theory has commonly been used to explain the photoreaction thermodynamics and kinetics of a semiconductor. Figure 1 shows the main processes during the photocatalytic conversion of CO_2 over semiconductor-based heterogeneous photocatalysts. (1) The first process is light harvesting; the photocatalyst absorbs enough light energy to generate electron-hole pairs. (2) The second process is charge separation; the photogenerated electrons and holes migrate from the inside of the bulk photocatalyst to the surface. Generally, most of the photogenerated electrons and holes recombine before they migrate to the photocatalyst surface, and therefore, it is more difficult for reactions in which many electrons (e.g., four or eight electrons) are consumed to occur than two-electron reactions. (3) The third process is a redox reaction; the photogenerated electrons react with adsorbed CO_2 species and protons (H^+) to produce hydrocarbon products (Eqn. 2–6), and the photogenerated holes are consumed by oxide species, such as added sacrificial reagents or H_2O.

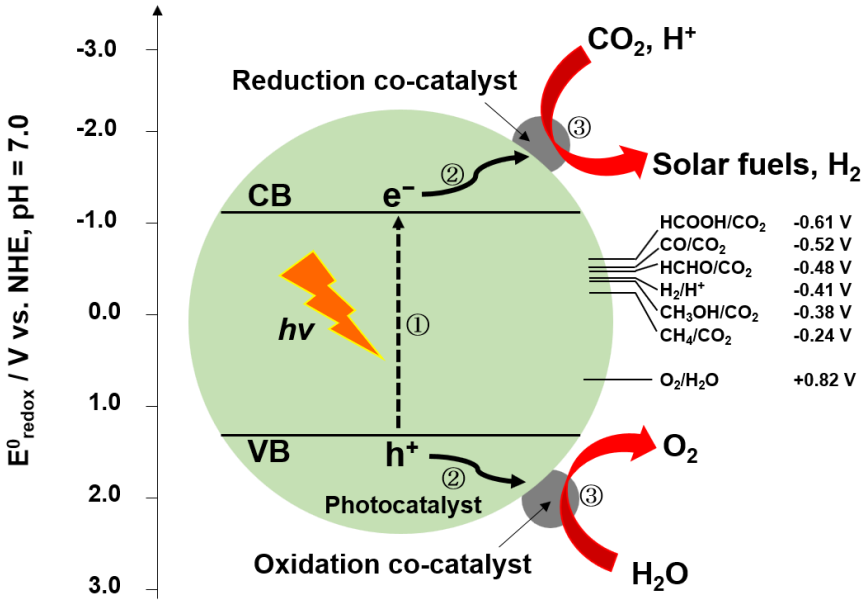

Figure 1. Schematic illustration of probable mechanism of photocatalytic conversion of CO_2 over a semiconductor-based photocatalyst for solar fuel production.

As a ubiquitous substance on Earth, H_2O is an ideal electron donor and H^+ source for the photocatalytic conversion of CO_2. In this case, H_2O not only provides H^+ for the reduction of CO_2, but also is oxidized to O_2 by the photogenerated holes (Eqn. 7). However, there is a dilemma with the use

of H_2O as an electron donor; because the redox potential of H^+ to H_2 with two electrons is more favorable, the generation of H_2 from H^+ (Eqn. 8) is always preferred to the generation of hydrocarbons from CO_2 and H^+ when H_2O is used as an electron donor. Consequently, it is necessary to monitor the evolution of H_2 and determine the selectivity of the photogenerated electrons during the photocatalytic conversion of CO_2 by H_2O (Eqn. 9).[13]

$$\text{Selectivity} = (2\boldsymbol{R}_{\mathbf{HCOOH}} + 2\boldsymbol{R}_{\mathbf{CO}} + 4\boldsymbol{R}_{\mathbf{HCHO}} + 6\boldsymbol{R}_{\mathbf{CH3OH}} + 8\boldsymbol{R}_{\mathbf{CH4}})/$$

$$(2\boldsymbol{R}_{\mathbf{HCOOH}} + 2\boldsymbol{R}_{\mathbf{CO}} + 4\boldsymbol{R}_{\mathbf{HCHO}} + 6\boldsymbol{R}_{\mathbf{CH3OH}} + 8\boldsymbol{R}_{\mathbf{CH4}} + 2\boldsymbol{R}_{\mathbf{H2}}) \quad (9)$$

where $\boldsymbol{R}_{\mathbf{x}}$ represents the formation rate of product x.

Additionally, a stoichiometric amount of O_2 as the oxidation product and hydrocarbons and/or H_2 as reduction products should be obtained, which would confirm that H_2O functions as the electron donor (Eqn. 10).[13]

$$\text{Consumed } e^-/h^+ = (2\boldsymbol{R}_{\mathbf{HCOOH}} + 2\boldsymbol{R}_{\mathbf{CO}} + 4\boldsymbol{R}_{\mathbf{HCHO}} + 6\boldsymbol{R}_{\mathbf{CH3OH}} + 8\boldsymbol{R}_{\mathbf{CH4}} + 2\boldsymbol{R}_{\mathbf{H2}})/4\boldsymbol{R}_{\mathbf{O2}} \quad (10)$$

If the photocatalytic conversion of CO_2 by H_2O proceeds stoichiometrically, then the value of e^-/h^+ should be equal to 1.

Accordingly, a suitable photocatalyst for the photocatalytic conversion of CO_2 by H_2O should fulfill the following demands: (1) adsorption of reactants such as H^+, CO_2, or carbon species, and desorption and diffusion of products into the system from the active site after the photocatalytic reaction; (2) proper conduction band (CB) and valence band (VB) edges to drive both CO_2 reduction and H_2O oxidation; and (3) efficient charge separation/trapping for the photocatalytic redox reactions. On the basis of these considerations, the photocatalytic efficiency of the conversion of CO_2 by H_2O can be improved by following the methods described below.

Surface engineering

Since the photocatalytic reaction is a surface reaction, the surface states of photocatalysts determine the CO_2/H_2O adsorption/activation and charge migration kinetics, which, in turn, greatly affect the photocatalytic performance in the conversion of CO_2.[14] Unlike the linear CO_2 molecule, CO_2

that is chemically adsorbed on a photocatalyst surface (mainly carbonate and/or bicarbonate species) has a bent O-C-O bond, which will be beneficial for the activation of CO_2.[15] Generally, CO_2 acts as a Lewis acid and bonds easily with Lewis bases such as alkaline earth oxides/hydroxides, amines, and amides.[16] Many studies have been launched towards improving CO_2 adsorption by modifying the photocatalyst surface with a CO_2 adsorbent.[17-19] For instance, Meng et al. reported that surface modification of TiO_2 with NaOH can enhance CO_2 adsorption and activation and led to highly effective photocatalytic conversion of CO_2 into CH_4.[20] Liao et al. found that amine groups on TiO_2 surfaces enable "C-N" bonding with CO_2 to form carbamates, which improved CO_2 adsorption for photoconversion into hydrocarbon fuels.[21] Our group also confirmed that the presence of a low amount of MO (M = Ca, Sr, Ba) can enhance the photocatalytic activity and selectivity in the conversion of CO_2 by H_2O into CO.[22] Additionally, rare earth compounds are also good candidates to be used as CO_2 adsorbents on photocatalyst surfaces. Recently, Huang et al.[23] and Tatsumi et al.[24] in our group reported that modification of the surface of Ga_2O_3 with rare earth species enhanced the formation rate of CO and selectivity toward CO evolution in the photocatalytic conversion of CO_2 by H_2O. If $NaHCO_3$ additives are introduced, the rare earth (RE) species on the Ga_2O_3 surface will transform them into carbonate hydrates ($RE_2(CO_3)_3 \cdot nH_2O$) and/or hydroxycarbonates ($RE_2(OH)_{2(3-x)}(CO_3)_x \cdot nH_2O$), which decompose upon photoirradiation, as shown in Figure 2.[23, 24] The rare earth species functions as a CO_2 capture and storage material that greatly improves the photocatalytic efficiency of the conversion of CO_2 by H_2O into CO.

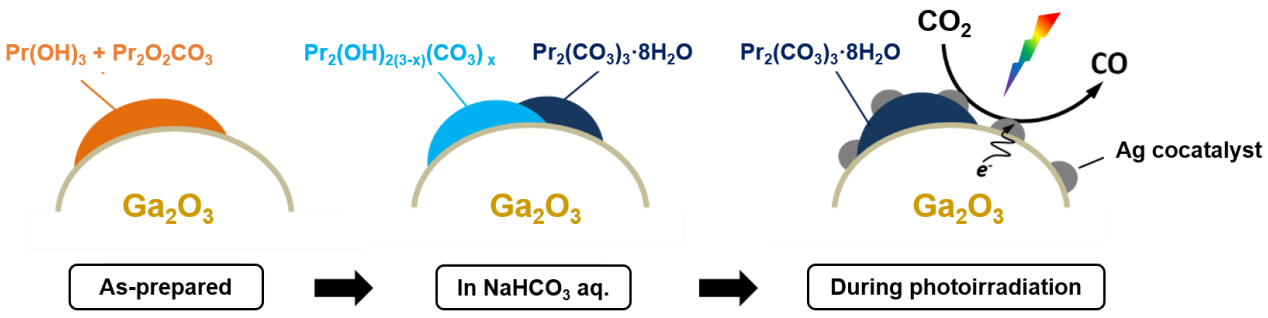

Figure 2. Formation of Pr species as a CO_2 capture and storage material in an aqueous solution of $NaHCO_3$ during the photocatalytic conversion of CO_2 in ref. 23.

Moreover, surface engineering can also be conducted by altering the surface defects (such as oxygen vacancies (V_o)) on a photocatalyst.[25, 26] It has been found that the presence of Ti^{3+} species or V_o facilitates charge transport and CO_2 adsorption in TiO_2.[27, 28] Yin et al. reported that slightly hydrogenated H-TiO_2 with a high ratio of trapped holes (O^- centers) and proper surface defects exhibited enhanced photocatalytic efficiency for CO_2 reduction compared to that of pristine TiO_2. However, highly hydrogenated H-TiO_2 with many bulk defects had significantly fewer O^- centers and enhanced non-radiative recombination; consequently, the photocatalytic efficiency was strongly decreased.[26]

The above surface engineering can significantly enhance the photocatalytic activity and selectivity in the photocatalytic conversion of CO_2 by enhancing the CO_2 adsorption and/or charge transport. However, there are still some controversial points that need to be clarified, such as (1) how the CO_2 adsorbent connects with the active sites for the enhanced activity and selectivity during the photocatalytic conversion of CO_2, since the CO_2 adsorbent generally does not act as the active site, and (2) how to process the surface photoreactions, the identity of the intermediate species, and the effect of H_2O on the photoreaction process with the surface modification.

Morphology engineering

Various micro-/nanostructured materials such as nanoparticles (zero-dimensional), nanorods/tubes/wires (one-dimensional), nanosheets (two-dimensional), and those with further exotic topologies such as nanoflowers, porous materials, and hierarchical photocatalysts can offer more active sites, better CO_2 adsorption, and faster charge transfer than bulk materials can. Therefore, it is expected that the photocatalytic efficiency in the conversion of CO_2 can be improved remarkably by constructing micro-/nanostructured photocatalysts. Zou's group reported that Zn_2GeO_4 nanoribbons with a high surface area (28 $m^2\ g^{-1}$) showed better photocatalytic performance in the conversion of CO_2 to CH_4 than did Zn_2GeO_4 prepared using a solid-state method (surface area: 1 $m^2\ g^{-1}$).[29] Moreover, in their subsequent work, they demonstrated that metal-organic frameworks such as ZIF-8 can effectively adsorb CO_2 dissolved in H_2O, which increased the photocatalytic activity in the conversion of CO_2 into CH_3OH.[30] Xie et al. successfully synthesized $SrNb_2O_6$ with nanoplate morphology using a hydrothermal method.[31] The $SrNb_2O_6$ nanoplates gave a higher CO formation rate and exhibited higher

selectivity toward CO evolution in the photocatalytic conversion of CO_2 using H_2O vapor compared to bulk $SrNb_2O_6$ and $SrNb_2O_6$ nanoparticles and nanorods. This is because the two-dimensional nanoplate structure and high surface area significantly enhanced the separation of photogenerated electron-hole pairs and CO_2 chemisorption. Layered double hydroxides (LDHs) composed of $[M^{2+}_{1-x}M^{3+}_{x}(OH)_2]^{x+}$ cationic sheets with intercalated anions have been exploited for the photocatalytic conversion of CO_2 because of their good CO_2 adsorption capacities and high surface areas. Zhao et al. prepared ultrathin Zn-containing LDH nanosheets that exhibited much better photocatalytic activity in the conversion of CO_2 into CO in the presence of H_2O vapor compared to a bulk LDH.[32] This is because the formation of Zn^{+}-V_o complexes in the ultrathin ZnAl-LDH nanosheets served as trapping sites to promote the adsorption of CO_2 and facilitated the electron transfer to the reactant. In a previous work by our group, a Mg-Al-LDH-loaded Ga_2O_3 photocatalyst was also reported to be highly active in the photocatalytic conversion of CO_2 by H_2O into CO.[33] The modification of the Ga_2O_3 surface with Mg-Al LDHs increased the specific surface area, which resulted in more CO_2 adsorption sites and concentrated the CO_2 species near the Ag co-catalyst. Therefore, the photocatalytic activity and selectivity in the conversion of CO_2 by H_2O into CO were significantly enhanced compared to those obtained with bare Ga_2O_3.

It should be noted that smaller particles do not always correspond to high photocatalytic efficiency. If the feature size of the particles, particularly of spherical particles, is comparable to the electron mean free path, a strong quantum confinement effect appears, increasing the recombination probability of the photogenerated electron-hole pairs.[34] Moreover, micro-/nanomorphization of a photocatalyst is accompanied by changes in its surface, structural, and interface properties, and further investigation and understanding of the CO_2 adsorption, activation, and charge transfer mechanisms of micro-/nanostructured photocatalysts are critical in both theory and practice.

Band-structure engineering

Generally, oxides or oxide/hydroxide composites containing d^0 (e.g., Ti^{4+}, Zr^{4+}, Ta^{5+}, and Nb^{5+} oxides) or d^{10} (e.g., In^{3+}, Ga^{3+}, and Ge^{4+} oxides) electronic configuration cations are candidates for the photocatalytic conversion of CO_2 by H_2O. The typical photocatalysts used for the photocatalytic conversion of CO_2 by H_2O under similar conditions reported recently are shown in Table 1. Notably,

most of these photocatalysts show wide band gaps that only respond in the ultraviolet (UV) region. To extend the absorption range of photocatalysts into the visible region, their band gaps can be narrowed by lowering the CB level and/or raising the VB level. As reported in earlier papers, cation doping (such as with Cu,[35, 36] Co,[37] Ni,[38] Ce,[39] Ag,[40, 41] or Cr[42]) can be used to adjust the VB level, and anion doping (such as with C,[43] N,[44] S,[45] or P[46]) can be used to raise the VB maximum by introducing these anions into the O sites.[4] For example, I-doped TiO_2 in which I^{5+} replaced Ti^{4+} showed significantly enhanced photocatalytic conversion of CO_2 by H_2O into CO.[47] N-doped $InTaO_4$ gave approximately twice the formation rate of methanol given by the undoped one in the photocatalytic conversion of CO_2 by H_2O, as compared with the undoped one.[48] TiO_2 catalysts co-doped with V and W showed enhanced photocatalytic activity in the conversion of CO_2 to CO and CH_4 compared to pristine and single-metal-doped TiO_2 catalysts.[49] The authors believe that V^{4+} doping enhances the visible-light absorption of TiO_2 by introducing an intermediate state within the band gap of TiO_2, while the V_2O_5 on the surface of TiO_2 and W^{6+} doped in the TiO_2 lattice promote the separation of photogenerated electron-hole pairs. Ye's group reported that ordered mesoporous cobalt-doped TiO_2 improved the visible light activity in the photocatalytic conversion of CO_2 by H_2O into CO and CH_4.[37] The doping of Co species increases the visible-light absorption and promotes the formation of oxygen vacancies, which is beneficial for enhancing the photocatalytic selectivity toward CH_4 evolution under visible-light irradiation.

As mentioned above, although narrowing the band gap of a photocatalyst is beneficial to visible-light absorption, it simultaneously suppresses the redox potentials. This inevitably gives rise to an implicit conflict between wide-range light absorption and adequate redox capability. Thus, it is necessary to fabricate a photocatalyst with a suitable band gap and sufficient CB and VB levels for the simultaneous reduction of CO_2 and oxidation of H_2O.

Table 1 Summary of photocatalysts for the conversion of CO_2 using H_2O as an electron donor under similar experimental conditions.

Catalyst	Weight / g	Light source	Co-catalyst	Additive	Activity / μmol h^{-1}			Selec. toward CO / %	Ref.
					H_2	O_2	CO		
$BaLa_4Ti_4O_{15}$	0.3	400 W Hg lamp	2.0 wt.% Ag	None	10.0	16.0	22.0	68.8	50
$NaTaO_3$:Ba	1.0	400 W Hg lamp	3.0 wt.% Ag	0.1 M $NaHCO_3$	31.0	170[a]	318	91.0	51
$CaTiO_3$	0.3	100 W Hg lamp	3.5 wt.% Ag	1.0 M $NaHCO_3$	3.10	25.0	54.0	94.0	52
$Na_2Ti_6O_{13}$	0.2	100 W Hg lamp	1.0 wt.% Ag	0.5 M $NaHCO_3$	1.60	0.700[a]	4.60	74.0	53
$La_2Ti_2O_7$	1.0	400 W Hg lamp	1.0 wt.% Ag	0.1 M $NaHCO_3$	4.09	5.30	5.20	51.5	54
$ZnGa_2O_4$	1.0	400 W Hg lamp	1.0 wt.% Ag	0.1 M $NaHCO_3$	8.50	74.3	155	95.0	55
$ZnGa_2O_4/Ga_2O_3$	1.0	400 W Hg lamp	1.0 wt.% Ag	0.1 M $NaHCO_3$	16.9	70.1	117	87.4	56
SrO/Ta_2O_5	1.0	400 W Hg lamp	3.0 wt.% Ag	0.1 M $NaHCO_3$	3.80	5.10	6.80	64.2	22
$KCaSrTa_5O_{15}$	0.5	400 W Hg lamp	0.5 wt.% Ag	0.1 M $NaHCO_3$	15.0	46.0	97.0	86.7	57
$ZnTa_2O_6$	1.0	400 W Hg lamp	1.0 wt.% Ag	0.1 M $NaHCO_3$	25.1	18.6	19.3	43.4	58
$Sr_2KTa_5O_{15}$	1.0	400 W Hg lamp	1.0 wt.% Ag	0.1 M $NaHCO_3$	8.30	34.3	65.5	88.8	59
$K_2YTa_5O_{15}$	1.0	400 W Hg lamp	1.0 wt.% Ag	0.1 M $NaHCO_3$	16.2	43.2	91.9	85.0	60
$Sr_{1.6}K_{0.37}Na_{1.43}Ta_5O_{15}$	1.0	400 W Hg lamp	1.0 wt.% Ag	0.1 M $NaHCO_3$	16.0	53.7	94.6	85.5	61
Mg-Al LDH/Ga_2O_3	1.0	400 W Hg lamp	1.0 wt.% Ag	0.1 M $NaHCO_3$	131	167	212	61.7	33
Pr/Ga_2O_3	0.5	400 W Hg lamp	1.0 wt.% Ag	0.1 M $NaHCO_3$	64.7	150	249	79.4	23
Yb-Zn/Ga_2O_3	0.5	400 W Hg lamp	1.0 wt.% Ag	0.1 M $NaHCO_3$	37.6	103	150	80.0	24

[a] Estimated from the figure mentioned in the paper.

Co-catalyst loading

Generally, high activity and selectivity are difficult to achieve in the photocatalytic conversion of CO_2 by H_2O over a bare photocatalyst. This is because of the facile recombination of electron-hole pairs before they are transferred to the surface for redox reactions and low surface reaction efficiency. Suitable co-catalysts loaded onto light-harvesting semiconductors can act as both electron sinks and proton reduction sites, thereby greatly enhancing the photocatalytic efficiency of the conversion of CO_2 by H_2O.[62] Since Hori et al. reported that metal electrodes (such as Au, Ag, Cu, and Zn) showed high selectivity toward CO evolution in the electrochemical reduction of CO_2,[63] noble metals (such as Pt,[64-66] Au,[67-69] Ag,[50-52, 57, 70] and Pd[71, 72]), non-noble metals (such as Cu[73, 74]), and their alloys or compounds (such as Au/Cu,[75] Cu/Pt,[76] Cu/Pd,[72] and Au/Pt[77]) have been widely used as co-catalysts in the photocatalytic conversion of CO_2. In addition, certain metal oxides (such as CuO_x,[78] RuO_x,[79] NiO_x,[80] CoO_x,[81] and MCo_2O_4 (M = Zn or Mn)[82]) have also been reported as co-catalysts that have been loaded onto semiconductors to enhance the photocatalytic efficiency of CO_2 conversion. Among them, Ag is considered to be the most effective co-catalyst toward CO evolution for the photocatalytic conversion of CO_2 by H_2O. Kudo et al.[50] reported for the first time that $ALa_4Ti_4O_{15}$ (A = Ca, Sr, Ba) photocatalysts loaded with a Ag co-catalyst showed higher activities and selectivities in the photocatalytic conversion of CO_2 to CO and HCOOH with H_2O acting as an electron donor than those loaded with other co-catalysts (NiO_x, Ru, Cu, Au). Consequently, various Ag-loaded photocatalysts have been reported for highly selective photocatalytic CO_2 conversion with H_2O as an electron donor.[51, 52, 57, 70] The photocatalytic conversion of CO_2 by H_2O over $NaTaO_3$:A (A = Ca, Sr, or Ba) loaded with a Ag co-catalyst gave much higher CO formation rates than did those loaded with other metals, such as Ni, Cu, Ru, Pd, and Au, as the co-catalyst.[51] Our group also found many photocatalysts that exhibit high selectivity toward CO evolution in the photocatalytic conversion of CO_2 by H_2O, such as Ag-modified $ZnGa_2O_4/Ga_2O_3$,[56, 83] $ZnGa_2O_4$,[55] $Sr_2KTa_5O_{15}$,[59] Mg-Al LDH/Ga_2O_3,[24] and $K_2RETa_5O_{15}$,[60] and detailed results are provided in Table 1.

Crystal facet engineering

Owing to the anisotropy properties of crystals, different facets of crystallized photocatalysts have

different surface energies, surface active sites, adsorption properties, and band structures.[84] Various studies have indicated that different facets of TiO_2 show different photocatalytic activities and selectivities in the conversion of CO_2.[85-89] For example, Ye et al. observed that the {010} facet with the best CO_2^-, M-CO_3^-, and HCO_3^- adsorption showed better photocatalytic performance in the conversion of CO_2 into CH_4 by H_2O than the {101} and {001} facets.[86] $ZnGa_2O_4$ nanocubes with exposed {100} facets exhibited improved performance in the photocatalytic reduction of CO_2 into CH_4 under UV-visible light irradiation compared to mesoporous $ZnGa_2O_4$, which has a larger specific surface area. Theoretical calculations indicated that the light-hole effective mass on the {100} facets of $ZnGa_2O_4$ corresponds to high hole mobility, which contributes to efficient water oxidation to provide the protons for promoting the photoreduction of CO_2 into hydrocarbon fuels. The authors from the same group further reported that single-crystal Zn_2GeO_4 nanorods with dominant (110) crystal faces also exhibited improved photocatalytic activity in CO_2 reduction, owing to the high specific surface area and low number of crystal defects.[90]

It should be noted that the distributions and morphologies of co-catalysts on different exposed facets also affect the photocatalytic performance in the conversion of CO_2. A Pt co-catalyst loaded on the {010} facets of TiO_2 can enhance the photoinduced carrier separation efficiency more effectively than on the {001} facets, therefore resulting in a photoactivity higher than that of Pt loaded on the {001} facets of TiO_2, although the {010} facets show stronger CO_2 adsorption than the {001} facets.[91] Li et al. also reported that the particle size and distribution of Ag on the exposed facets of brookite TiO_2 quasi nanocubes showed significant influences on the photocatalytic activity and selectivity in the conversion of CO_2 into CO/CH_4.[89]

Hybrid photocatalysts

The photocatalytic activity and selectivity in the conversion of CO_2 can be improved through various approaches such as surface, morphology, band gap, and crystal facet engineering of single-semiconductor-based photocatalysts. However, much attention has also been paid to the construction of hybrid photocatalysts, such as semiconductor heterojunctions and Z-scheme systems, to further increase the photocatalytic efficiency in the conversion of CO_2.[14, 92] In addition to the various well-known oxides and oxysalt-based hybrid photocatalysts, such as TiO_2/ZnO,[93] α-Fe_2O_3/Cu_2O,[94] and

Pt@CdS/TiO_2.[95] Recently, carbon nanostructures (such as graphene oxide,[96] carbon nanotubes,[97] and carbon quantum dots[98]) and g-C_3N_4-based[99-101] hybrid photocatalysts have also been employed extensively to enhance the photocatalytic activity and selectivity in the conversion of CO_2 by H_2O. For instance, a g-C_3N_4/$NaNbO_3$ nanowire heterojunction photocatalyst was developed to remarkably enhance the evolution rate of CH_4 for the photocatalytic conversion of CO_2 by H_2O.[100] The heterojunction of g-C_3N_4 with $NaNbO_3$ greatly enhances the absorption of visible light and transfer of photogenerated electron-hole pairs. However, it should be noted that the selection of the carbon source in the photocatalytic conversion of CO_2 is extremely important when carbon-based materials are used. In addition to conducting blank experiments, $^{13}CO_2$ isotopic labeling is also a good technique to confirm whether carbon-containing products are derived from the introduced CO_2 rather than from carbonaceous impurities.

Outline of the present thesis

This thesis focused on improve the photocatalytic performance in the conversion of CO_2 with H_2O as an electron donor. Particularly, the effects of co-catalysts on the photocatalytic activity and selectivity for the conversion of CO_2 to CO evolution. Six chapters are consisted in this thesis.

Chapter 1 investigates the photocatalytic conversion of CO_2 by H_2O over two strontium niobates ($SrNb_2O_6$ and $Sr_2Nb_2O_7$) synthesized by a flux method. After modification with a Ag co-catalyst, $SrNb_2O_6$ with a nanorod structure exhibited higher photocatalytic activity and selectivity toward CO evolution as compared to $Sr_2Nb_2O_7$ with a nanoflake structure and $SrNb_2O_6$ with a nanoparticle structure. The separation of the reduction sites from the oxidation sites was observed on the $SrNb_2O_6$ nanorod under the photoirradiation, which contributed to the decrease in the recombination of the photogenerated carriers; hence, Ag/$SrNb_2O_6$ nanorods exhibit good activity and selectivity for the photocatalytic conversion of CO_2.

Chapter 2 shows that Ag/$SrNb_2O_6$ nanorods exhibited a high CO formation rate and high selectivity toward CO evolution in aqueous solutions containing bicarbonate ions even without CO_2 bubbling. Both the formation rate of CO and selectivity toward CO evolution increased with the concentration of HCO_3^-. According to the experimental results and analytical chemistry calculations,

it was concluded that the CO_2 (aq) obtained by the dissociation of HCO_3^- was the actual reactant for the photocatalytic conversion of CO_2. Interestingly, the presence of HCO_3^- showed a great influence on the photocatalytic activity and selectivity for the conversion of CO_2, although it is not the direct reactant for the photocatalytic conversion of CO_2.

Chapter 3 describes that a core-shell structure Ag-$Cr(OH)_3{\cdot}xH_2O$ dual co-catalyst loaded Ga_2O_3 significantly improved the formation rate of CO and selectivity toward CO evolution, compared with bare Ga_2O_3, Ag/Ga_2O_3, and Cr/Ga_2O_3. The backward reaction tests, which produced CO_2 from CO and O_2 in H_2O, indicated that the modification of $Cr(OH)_3{\cdot}xH_2O$ thin layer on the surface of Ag co-catalyst drastically suppressed the backward reaction for the photocatalytic conversion of CO_2.

In chapter 4, the functions of Ag and Cr species in Ag-Cr/Ga_2O_3 during the photocatalytic conversion of CO_2 were investigated. Ag acted as an active site for the photocatalytic conversion of CO_2 into CO, and the $Cr(OH)_3{\cdot}xH_2O$ layer on the surface of Ag@Cr/Ga_2O_3 changed to $Cr(OH)_x(CO_3)_y$, which increased the CO_2 adsorption on the Ag active site. The Ag@Cr core-shell-structured co-catalyst modification method provides a general strategy for significantly improving the efficiency of the photocatalytic conversion of CO_2 into CO by H_2O.

Chapter 5 presents that the formation rate of CO for the photocatalytic conversion of CO_2 by H_2O over Ag@Cr/Ga_2O_3 decreased with increasing photoirradiation time. It is found that Cr^{3+} in Ag@Cr/Ga_2O_3 was oxidized to soluble Cr^{6+} during the photocatalytic conversion of CO_2 in a $NaHCO_3$ aqueous solution under UV light irradiation. The decrease of CO evolved showed a good dependence on the dissolution rates of Cr^{3+}, which indicated that the dissolution of Cr^{3+} on the surface of Ag@Cr/Ga_2O_3 leads to a decrease in the formation rate of CO. However, this loss could be compensated by reloading supplementary Cr^{3+} in Ag@Cr/Ga_2O_3.

In chapter 6, a Ca modification technique was proposed for highly efficient photocatalytic conversion of CO_2 by H_2O into CO. When a small amount of calcium was modified on Ga_2O_3, both CaO and $CaGa_4O_7$ were formed on the surface of Ga_2O_3, which is beneficial for simultaneously improving photocatalytic activity and selectivity for the conversion of CO_2 to CO by H_2O. However, excessive Ca modification caused only $CaGa_4O_7$ loaded on the Ga_2O_3 surface, which decreased the formation rate of CO and selectivity toward CO evolution because $CaGa_4O_7$ only showed activity for the water splitting.

References

1. R. K. Pachauri, M. R. Allen, V. R. Barros, J. Broome, W. Cramer, R. Christ, J. A. Church, L. Clarke, Q. Dahe and P. Dasgupta, *Climate change 2014: synthesis report. Contribution of Working Groups I, II and III to the fifth assessment report of the Intergovernmental Panel on Climate Change*, IPCC, 2014.
2. J. Barber, *Chem. Soc. Rev.*, 2009, **38**, 185-196.
3. M. Mikkelsen, M. Jørgensen and F. C. Krebs, *Energy Environ. Sci.*, 2010, **3**, 43-81.
4. M. Halmann, *Nature*, 1978, **275**, 115-116.
5. T. Inoue, A. Fujishima, S. Konishi and K. Honda, *Nature*, 1979, **277**, 637-638.
6. W. Tu, Y. Zhou and Z. Zou, *Adv. Mater.*, 2014, **26**, 4607-4626.
7. M. Marszewski, S. Cao, J. Yu and M. Jaroniec, *Mater. Horiz.*, 2015, **2**, 261-278.
8. S. N. Habisreutinger, L. Schmidt-Mende and J. K. Stolarczyk, *Angew. Chem. Int. Ed.*, 2013, **52**, 7372-7408.
9. J. Mao, K. Li and T. Peng, *Catal. Sci. Technol.*, 2013, **3**, 2481-2498.
10. Y.-P. Yuan, L.-W. Ruan, J. Barber, S. C. J. Loo and C. Xue, *Energy Environ. Sci.*, 2014, **7**, 3934-3951.
11. J.-M. Lehn and R. Ziessel, *Proc. Natl. Acad. Sci. U.S.A.*, 1982, **79**, 701-704.
12. J. L. White, M. F. Baruch, J. E. Pander Iii, Y. Hu, I. C. Fortmeyer, J. E. Park, T. Zhang, K. Liao, J. Gu, Y. Yan, T. W. Shaw, E. Abelev and A. B. Bocarsly, *Chem. Rev.*, 2015, **115**, 12888-12935.
13. K. Teramura and T. Tanaka, *Phys. Chem. Chem. Phys.*, 2018, **20**, 8423-8431.
14. K. Li, B. Peng and T. Peng, *ACS Catalysis*, 2016, **6**, 7485-7527.
15. K. Teramura, T. Tanaka, H. Ishikawa, Y. Kohno and T. Funabiki, *J. Phys. Chem. B*, 2004, **108**, 346-354.
16. I. Bhugun, D. Lexa and J.-M. Savéant, *J. Phys. Chem.*, 1996, **100**, 19981-19985.
17. S. Xie, Y. Wang, Q. Zhang, W. Fan, W. Deng and Y. Wang, *Chem. Commun.*, 2013, **49**, 2451-2453.
18. S. Xie, Y. Wang, Q. Zhang, W. Deng and Y. Wang, *ACS Catalysis*, 2014, **4**, 3644-3653.
19. L. Liu, C. Zhao, H. Zhao, D. Pitts and Y. Li, *Chem. Commun.*, 2013, **49**, 3664-3666.

20. X. Meng, S. Ouyang, T. Kako, P. Li, Q. Yu, T. Wang and J. Ye, *Chem. Commun.*, 2014, **50**, 11517-11519.
21. Y. Liao, S. W. Cao, Y. Yuan, Q. Gu, Z. Zhang and C. Xue, *Chem. – Eur. J.*, 2014, **20**, 10220-10222.
22. K. Teramura, H. Tatsumi, Z. Wang, S. Hosokawa and T. Tanaka, *Bull. Chem. Soc. Jpn.*, 2015, **88**, 431-437.
23. Z. Huang, K. Teramura, H. Asakura, S. Hosokawa and T. Tanaka, *J. Mater. Chem. A*, 2017, **5**, 19351-19357.
24. H. Tatsumi, K. Teramura, Z. Huang, Z. Wang, H. Asakura, S. Hosokawa and T. Tanaka, *Langmuir*, 2017, **33**, 13929-13935.
25. M. Manzanares, C. Fàbrega, J. O. Ossó, L. F. Vega, T. Andreu and J. R. Morante, *Appl. Catal. B*, 2014, **150**, 57-62.
26. Y. Yan, M. Han, A. Konkin, T. Koppe, D. Wang, T. Andreu, G. Chen, U. Vetter, J. R. Morante and P. Schaaf, *J. Mater. Chem. A*, 2014, **2**, 12708-12716.
27. X. Pan, M.-Q. Yang, X. Fu, N. Zhang and Y.-J. Xu, *Nanoscale*, 2013, **5**, 3601-3614.
28. W. Pipornpong, R. Wanbayor and V. Ruangpornvisuti, *Appl. Surf. Sci.*, 2011, **257**, 10322-10328.
29. Q. Liu, Y. Zhou, J. Kou, X. Chen, Z. Tian, J. Gao, S. Yan and Z. Zou, *J. Am. Chem. Soc.*, 2010, **132**, 14385-14387.
30. Q. Liu, Z.-X. Low, L. Li, A. Razmjou, K. Wang, J. Yao and H. Wang, *J. Mater. Chem. A*, 2013, **1**, 11563-11569.
31. S. Xie, Y. Wang, Q. Zhang, W. Deng and Y. Wang, *Chem. Commun.*, 2015, **51**, 3430-3433.
32. Y. Zhao, G. Chen, T. Bian, C. Zhou, G. I. Waterhouse, L. Z. Wu, C. H. Tung, L. J. Smith, D. O'Hare and T. Zhang, *Adv. Mater.*, 2015, **27**, 7824-7831.
33. S. Iguchi, Y. Hasegawa, K. Teramura, S. Kidera, S. Kikkawa, S. Hosokawa, H. Asakura and T. Tanaka, *Sustainable Energy Fuels*, 2017, **1**, 1740-1747.
34. Y. Kayanuma, *Phys. Rev. B*, 1988, **38**, 9797.
35. O. Ola and M. M. Maroto-Valer, *Catal. Sci. Technol.*, 2014, **4**, 1631-1637.
36. P. Richardson, M. L. Perdigoto, W. Wang and R. J. Lopes, *Appl. Catal. B*, 2012, **126**, 200-207.
37. T. Wang, X. Meng, G. Liu, K. Chang, P. Li, Q. Kang, L. Liu, M. Li, S. Ouyang and J. Ye, *J.*

Mater. Chem. A, 2015, **3**, 9491-9501.

38. B. S. Kwak, K. Vignesh, N.-K. Park, H.-J. Ryu, J.-I. Baek and M. Kang, *Fuel*, 2015, **143**, 570-576.
39. L. Matějová, K. Kočí, M. Reli, L. Čapek, A. Hospodková, P. Peikertová, Z. Matěj, L. Obalová, A. Wach and P. Kuśtrowski, *Appl. Catal. B*, 2014, **152**, 172-183.
40. K. Kočí, K. Matějů, L. Obalová, S. Krejčíková, Z. Lacný, D. Plachá, L. Čapek, A. Hospodková and O. Šolcová, *Appl. Catal. B*, 2010, **96**, 239-244.
41. S. Krejčíková, L. Matějová, K. Kočí, L. Obalová, Z. Matěj, L. Čapek and O. Šolcová, *Appl. Catal. B*, 2012, **111**, 119-125.
42. O. Ola and M. M. Maroto-Valer, *Appl. Catal., A*, 2015, **502**, 114-121.
43. S. K. Parayil, A. Razzaq, S.-M. Park, H. R. Kim, C. A. Grimes and S.-I. In, *Appl. Catal., A*, 2015, **498**, 205-213.
44. Z. Zhang, Z. Huang, X. Cheng, Q. Wang, Y. Chen, P. Dong and X. Zhang, *Appl. Surf. Sci.*, 2015, **355**, 45-51.
45. X. Meng, Q. Yu, G. Liu, L. Shi, G. Zhao, H. Liu, P. Li, K. Chang, T. Kako and J. Ye, *Nano Energy*, 2017, **34**, 524-532.
46. E. E. Barton, D. M. Rampulla and A. B. Bocarsly, *J. Am. Chem. Soc.*, 2008, **130**, 6342-6344.
47. Q. Zhang, Y. Li, E. A. Ackerman, M. Gajdardziska-Josifovska and H. Li, *Appl. Catal., A*, 2011, **400**, 195-202.
48. C.-W. Tsai, H. M. Chen, R.-S. Liu, K. Asakura and T.-S. Chan, *J. Phys. Chem. C*, 2011, **115**, 10180-10186.
49. Z. Xiong, Z. Lei, S. Ma, X. Chen, B. Gong, Y. Zhao, J. Zhang, C. Zheng and J. C. Wu, *Appl. Catal. B*, 2017, **219**, 412-424.
50. K. Iizuka, T. Wato, Y. Miseki, K. Saito and A. Kudo, *J. Am. Chem. Soc.*, 2011, **133**, 20863-20868.
51. H. Nakanishi, K. Iizuka, T. Takayama, A. Iwase and A. Kudo, *ChemSusChem*, 2017, **10**, 112-118.
52. A. Anzai, N. Fukuo, A. Yamamoto and H. Yoshida, *Catal. Commun.*, 2017, **100**, 134-138.
53. X. Zhu, A. Anzai, A. Yamamoto and H. Yoshida, *Appl. Catal. B*, 2019, **243**, 47-56.

54. Z. Wang, K. Teramura, S. Hosokawa and T. Tanaka, *Appl. Catal. B*, 2015, **163**, 241-247.

55. Z. Wang, K. Teramura, S. Hosokawa and T. Tanaka, *J. Mater. Chem. A*, 2015, **3**, 11313-11319.

56. Z. Wang, K. Teramura, Z. Huang, S. Hosokawa, Y. Sakata and T. Tanaka, *Catal. Sci. Technol.*, 2016, **6**, 1025-1032.

57. T. Takayama, A. Iwase and A. Kudo, *Bull. Chem. Soc. Jpn.*, 2015, **88**, 538-543.

58. S. Iguchi, K. Teramura, S. Hosokawa and T. Tanaka, *Catal. Sci. Technol.*, 2016, **6**, 4978-4985.

59. Z. Huang, K. Teramura, S. Hosokawa and T. Tanaka, *Appl. Catal. B*, 2016, **199**, 272-281.

60. Z. Huang, K. Teramura, H. Asakura, S. Hosokawa and T. Tanaka, *Catal. Today*, 2018, **300**, 173-182.

61. Z. Huang, S. Yoshizawa, K. Teramura, H. Asakura, S. Hosokawa and T. Tanaka, *ACS Omega*, 2017, **2**, 8187-8197.

62. J. Yang, D. Wang, H. Han and C. Li, *Acc. Chem. Res.*, 2013, **46**, 1900-1909.

63. Y. Hori, H. Wakebe, T. Tsukamoto and O. Koga, *Electrochim. Acta*, 1994, **39**, 1833-1839.

64. K. Li, A. D. Handoko, M. Khraisheh and J. Tang, *Nanoscale*, 2014, **6**, 9767-9773.

65. B. AlOtaibi, S. Fan, D. Wang, J. Ye and Z. Mi, *ACS Catalysis*, 2015, **5**, 5342-5348.

66. K. Wang, Q. Li, B. Liu, B. Cheng, W. Ho and J. Yu, *Appl. Catal. B*, 2015, **176**, 44-52.

67. S. Sahu, L. Cao, M. J. Meziani, C. E. Bunker, K. S. Fernando, P. Wang and Y.-P. Sun, *Chem. Phys. Lett.*, 2015, **634**, 122-128.

68. H. Zhou, P. Li, J. Guo, R. Yan, T. Fan, D. Zhang and J. Ye, *Nanoscale*, 2015, **7**, 113-120.

69. H. Zhou, J. Guo, P. Li, T. Fan, D. Zhang and J. Ye, *Sci. Rep.*, 2013, **3**, 1667.

70. H. Yoshida, L. Zhang, M. Sato, T. Morikawa, T. Kajino, T. Sekito, S. Matsumoto and H. Hirata, *Catal. Today*, 2015, **251**, 132-139.

71. V. Vaiano, D. Sannino and P. Ciambelli, *Photochem. Photobiol. Sci.*, 2015, **14**, 550-555.

72. K. Sasan, F. Zuo, Y. Wang and P. Feng, *Nanoscale*, 2015, **7**, 13369-13372.

73. B. Fang, Y. Xing, A. Bonakdarpour, S. Zhang and D. P. Wilkinson, *ACS Sustainable Chem. Eng.*, 2015, **3**, 2381-2388.

74. E. Liu, L. Qi, J. Bian, Y. Chen, X. Hu, J. Fan, H. Liu, C. Zhu and Q. Wang, *Mater. Res. Bull.*, 2015, **68**, 203-209.

75. Q. Kang, T. Wang, P. Li, L. Liu, K. Chang, M. Li and J. Ye, *Angew. Chem. Int. Ed.*, 2015, **54**,

841-845.

76. Q. Zhai, S. Xie, W. Fan, Q. Zhang, Y. Wang, W. Deng and Y. Wang, *Angew. Chem. Int. Ed.*, 2013, **52**, 5776-5779.
77. Z. Zhang, Z. Wang, S.-W. Cao and C. Xue, *J. Phys. Chem. C*, 2013, **117**, 25939-25947.
78. G. Yin, M. Nishikawa, Y. Nosaka, N. Srinivasan, D. Atarashi, E. Sakai and M. Miyauchi, *ACS Nano*, 2015, **9**, 2111-2119.
79. A. D. Handoko and J. Tang, *Int. J. Hydrogen Energy*, 2013, **38**, 13017-13022.
80. P.-W. Pan and Y.-W. Chen, *Catal. Commun.*, 2007, **8**, 1546-1549.
81. D.-S. Lee, H.-J. Chen and Y.-W. Chen, *J. Phys. Chem. Solids*, 2012, **73**, 661-669.
82. S. Wang, Y. Hou and X. Wang, *ACS Appl. Mater. Interfaces*, 2015, **7**, 4327-4335.
83. K. Teramura, Z. Wang, S. Hosokawa, Y. Sakata and T. Tanaka, *Chem. – Eur. J.*, 2014, **20**, 9906-9909.
84. H. G. Yang, C. H. Sun, S. Z. Qiao, J. Zou, G. Liu, S. C. Smith, H. M. Cheng and G. Q. Lu, *Nature*, 2008, **453**, 638.
85. L. Mino, G. Spoto and A. M. Ferrari, *J. Phys. Chem. C*, 2014, **118**, 25016-25026.
86. L. Ye, J. Mao, T. Peng, L. Zan and Y. Zhang, *Phys. Chem. Chem. Phys.*, 2014, **16**, 15675-15680.
87. J. Yu, J. Low, W. Xiao, P. Zhou and M. Jaroniec, *J. Am. Chem. Soc.*, 2014, **136**, 8839-8842.
88. Q. Xu, J. Yu, J. Zhang, J. Zhang and G. Liu, *Chem. Commun.*, 2015, **51**, 7950-7953.
89. K. Li, T. Peng, Z. Ying, S. Song and J. Zhang, *Appl. Catal. B*, 2016, **180**, 130-138.
90. S. Yan, L. Wan, Z. Li and Z. Zou, *Chem. Commun.*, 2011, **47**, 5632-5634.
91. J. Mao, L. Ye, K. Li, X. Zhang, J. Liu, T. Peng and L. Zan, *Appl. Catal. B*, 2014, **144**, 855-862.
92. Y. Ma, X. Wang, Y. Jia, X. Chen, H. Han and C. Li, *Chem. Rev.*, 2014, **114**, 9987-10043.
93. G. Xi, S. Ouyang and J. Ye, *Chem. – Eur. J.*, 2011, **17**, 9057-9061.
94. J.-C. Wang, L. Zhang, W.-X. Fang, J. Ren, Y.-Y. Li, H.-C. Yao, J.-S. Wang and Z.-J. Li, *ACS Appl. Mater. Interfaces*, 2015, **7**, 8631-8639.
95. Y. Wei, J. Jiao, Z. Zhao, W. Zhong, J. Li, J. Liu, G. Jiang and A. Duan, *J. Mater. Chem. A*, 2015, **3**, 11074-11085.
96. J. Low, J. Yu and W. Ho, *J. Phys. Chem. Lett*, 2015, **6**, 4244-4251.
97. M. A. Asi, L. Zhu, C. He, V. K. Sharma, D. Shu, S. Li, J. Yang and Y. Xiong, *Catal. Today*,

2013, **216**, 268-275.

98. H. Li, X. Zhang and D. R. MacFarlane, *Adv. Energy Mater.*, 2015, **5**, 1401077.

99. Y. He, Y. Wang, L. Zhang, B. Teng and M. Fan, *Appl. Catal. B*, 2015, **168**, 1-8.

100. H. Shi, G. Chen, C. Zhang and Z. Zou, *ACS Catalysis*, 2014, **4**, 3637-3643.

101. J. Yu, K. Wang, W. Xiao and B. Cheng, *Phys. Chem. Chem. Phys.*, 2014, **16**, 11492-11501.

Chapter 1

Highly selective photocatalytic conversion of CO_2 by water over Ag-loaded $SrNb_2O_6$ nanorods

Abstract

Strontium niobates ($SrNb_2O_6$ and $Sr_2Nb_2O_7$) with regular nanostructures were synthesized by a facile flux method. Ag-loaded $SrNb_2O_6$ and $Sr_2Nb_2O_7$ exhibited different performances for the photocatalytic reduction of CO_2 in H_2O. Compared to $Sr_2Nb_2O_7$ nanoflakes and $SrNb_2O_6$ nanoparticles, $SrNb_2O_6$ nanorods exhibited higher photocatalytic activity and selectivity toward CO evolution. Stoichiometric amounts of CO (51.2 μmol h^{-1}) and H_2 (1.1 μmol h^{-1}) as the reduction products, in addition to O_2 (24.8 μmol h^{-1}) as the oxidation product, were obtained, indicating that H_2O serves as an electron donor in the photocatalytic conversion of CO_2. In addition, the effect of the Ag co-catalyst on the photocatalytic conversion of CO_2 was investigated.

Introduction

Carbon dioxide (CO_2), which is one of the major contributors to the greenhouse gas effect, has become a worldwide environmental burden because of fossil fuel consumption.[1-4] As a result, supplementing the natural carbon cycle and addressing climate change are imperative. The conversion of CO_2 to other valuable chemical compounds, e.g. CO, HCOOH, HCHO, CH_3OH, and CH_4, under ambient temperature and pressure conditions has attracted considerable attention as a sustainable strategy to solve environmental and energy issues,[5-9] especially conversion of CO_2 into CO, which is widely studied in recent years as an alternative route to produce syngas components.[10, 11] Since the discovery of the photoreduction of CO_2 into organic compounds using various semiconductors by Inoue et al.,[5, 12] several studies on the semiconductor-based photocatalytic conversion of CO_2 using H_2O as an electron donor have been reported.[13-18] Nevertheless, the selective activation of CO_2 by electrons and suppression of H_2 evolution in an aqueous solution are difficult because the redox potential of H^+/H_2 (−0.41 V vs. NHE, at pH 7) is more positive than that of CO/CO_2 (−0.51 V vs. NHE, at pH 7).[19, 20] Previously, our group has reported high activity for Ag-loaded $ZnGa_2O_4$-modified Ga_2O_3,[21, 22] $La_2Ti_2O_7$,[23] SrO-modified Ta_2O_5,[24] $ZnGa_2O_4$,[25] $Sr_2KTa_5O_{15}$,[26] and $ZnTa_2O_6$[27] for the photocatalytic conversion of CO_2 by H_2O under UV irradiation. Ag co-catalysts are well known to be effective for the conversion of CO_2 to CO in aqueous solutions.[14, 28, 29] However, still only a few photocatalysts have been reported, which exhibit high activity and selectivity for the photocatalytic conversion of CO_2 by H_2O, even with the modification of a Ag co-catalyst. Hence, it is imperative to develop highly efficient photocatalysts for CO_2 reduction using water as the electron donor.

Niobium-containing materials, e.g., $SrNb_2O_6$ and $Sr_2Nb_2O_7$, have been reported as promising candidates for water splitting because of their attractive layered crystal structures, containing the $[NbO_6]$ octahedra that can be distorted, and the high energy of the Nb 4d orbitals.[30-34] These structural advantages of niobium-based materials also make them promising for the photocatalytic reduction of CO_2. Nevertheless, only a few studies have reported the photocatalytic performance of niobium-based photocatalysts for CO_2 reduction, and the reported activity and selectivity were not satisfactory.[35-37] An inerratic nanostructure for a photocatalyst has been reported to not only increase active sites for the photocatalytic reduction of CO_2 in the presence of H_2O but also promote the separation of oxidation

and reduction sites because of its anisotropic effect.[14, 26, 38, 39] In this study, two strontium niobates (e.g. $SrNb_2O_6$ and $Sr_2Nb_2O_7$) with regular nanostructures were synthesized by a flux method, and their performance in the photocatalytic conversion of CO_2 in H_2O was investigated. After modification with a Ag co-catalyst, $SrNb_2O_6$ with a nanorod structure exhibited higher photocatalytic activity and selectivity toward CO evolution compared to $Sr_2Nb_2O_7$ with a nanoflake structure and $SrNb_2O_6$ with a nanoparticle structure. In addition, the effects of the Ag co-catalyst on the photocatalytic conversion of CO_2 were discussed.

Experimental

Photocatalyst preparation

$SrNb_2O_6$ and $Sr_2Nb_2O_7$ were prepared by a flux method. To fabricate $SrNb_2O_6$, 2.0 g of Nb_2O_5 powder (99.9%, Wako) and 6.0 g of $SrCl_2 \cdot 6H_2O$ (99.9%, Wako) were ground in an alumina mortar for 5 min. $SrCl_2 \cdot 6H_2O$ was used as the precursor and flux reagent. The mixture was calcined in air using an alumina crucible at 1173 K for 2 h. After calcination, the obtained powder was thoroughly washed three times with hot water (353 K) to remove the residual salt and dried at 353 K in an oven. The process of synthesizing $Sr_2Nb_2O_7$ was almost the same as that of synthesizing $SrNb_2O_6$, except for the use of $SrCO_3$ (99.9%, Wako) as the precursor. Modification using a Ag co-catalyst was performed by chemical reduction (CR), impregnation (IMP), and photodeposition (PD) methods. For modification by CR method, the obtained $SrNb_2O_6$ or $Sr_2Nb_2O_7$ (1.5 g) was suspended into a 50 mL aqueous solution of $AgNO_3$ (0.1 M), followed by the dropwise addition of a $NaPH_2O_2$ (0.4 M) solution into the suspension. After stirring the mixture at 358 K for 1.5 h, it was filtered and dried at room temperature. For modification by IMP method, $SrNb_2O_6$ (1.5 g) was homogeneously dispersed in an aqueous $AgNO_3$ solution, followed by evaporation at 358 K to remove water and calcination at 723 K for 2 h in air. Modification by PD method was carried out in situ during the photocatalytic conversion of CO_2. The synthetic details have been reported in our previous studies.[24, 27] Generally, 1.5 g of $SrNb_2O_6$ powder was dispersed in 1.0 L of ultra-pure water containing a required amount of $AgNO_3$, and the dissolved air in the solution was completely degassed by a flow of Ar gas. The suspension was irradiated under a 400 W high-pressure Hg lamp with a quartz filter using an inner-irradiation-type

reaction vessel with Ar gas flowing for 1.5 h, followed by filtration and dried at room temperature.

Characterization

The crystal phase and structure of the samples were observed by powder X-ray diffractometry (Rigaku Multiflex) with Cu Kα radiation (λ = 0.154 nm) at a scan rate of 4° min^{-1}. Sample morphologies were observed by field-emission scanning electron microscopy (FE-SEM, SU-8220, Hitachi High Technologies) and transmission electron microscopy (TEM, JEM-2100F). The Brunauer–Emmett–Teller surface areas of the photocatalysts were measured by their N_2 adsorption isotherms at 77 K using a volumetric gas adsorption apparatus (BELSORP-mini II, BEL Japan, Inc.). Prior to the measurements, each sample was evacuated at 473 K for 1 h using a pretreatment system (BELPREP-vacII, BEL Japan, Inc.). UV–Vis diffuse-reflectance spectra were recorded on a UV–visible spectrometer (V-650, JASCO) equipped with an integrated sphere accessory.

Photocatalytic reaction

The photocatalytic conversion of CO_2 was carried out using a flow system with an inner-irradiation-type reaction vessel at ambient pressure. First, the synthesized photocatalyst (0.5 g) was dispersed in ultrapure water (1.0 L) containing 0.1 M $NaHCO_3$. Second, CO_2 was bubbled into the solution at a flow rate of 30 mL min^{-1}. Third, the suspension was illuminated using a 400 W high-pressure mercury lamp with a quartz filter connected to a water cooling system. The amounts of the evolved H_2 and O_2 were detected using a thermal conductivity detector–gas chromatography system (TCD-GC, Shimadzu Corp; MS-5A column, Ar carrier). The amount of evolved CO was analyzed by a flame ionization detector–GC with a methanizer (ShinCarbon ST column, N_2 carrier). The selectivity toward CO evolution compared to H_2 evolution and the balance between the consumed electrons (e^-) and holes (h^+) were expressed by eqns. (1) and (2), respectively:

$$\text{Selectivity toward CO evolution (\%)} = 100 \times 2\boldsymbol{R}_{\mathbf{CO}}/(2\boldsymbol{R}_{\mathbf{CO}} + 2\boldsymbol{R}_{\mathbf{H2}}) \quad (1)$$

$$\text{Consumed } e^-/h^+ = (2\boldsymbol{R}_{\mathbf{CO}} + 2\boldsymbol{R}_{\mathbf{H2}})/4\boldsymbol{R}_{\mathbf{O2}} \quad (2)$$

Here, $\boldsymbol{R}_{\mathbf{CO}}$ and $\boldsymbol{R}_{\mathbf{H2}}$ represent the formation rates of CO and H_2, respectively.

In the isotopic experiment, $^{12}CO_2$ was replaced by $^{13}CO_2$. The formation rates of H_2, O_2, ^{13}CO, and ^{12}CO under photoirradiation were detected using a quadrupole mass spectrometer (BELMASS, Microtrac BEL) combined with a TCD-GC detector.

Results and discussion

Figure 1 shows the XRD patterns of as-prepared $SrNb_2O_6$ and $Sr_2Nb_2O_7$ fabricated by a flux method. All the diffraction peaks in the upper and lower patterns were accurately indexed to the pure monoclinic phase of $SrNb_2O_6$ with a $P12_1/c$ space group (JCPDS 72-2088) and the orthorhombic phase of $Sr_2Nb_2O_7$ with a $Cmc2_1$ space group (JCPDS 70-0114), respectively.[32] No peaks corresponding to other impurity phases were observed, indicating that the pure phases of $SrNb_2O_6$ and $Sr_2Nb_2O_7$ are successfully prepared by calcination at 1173 K for 2 h by the flux method.

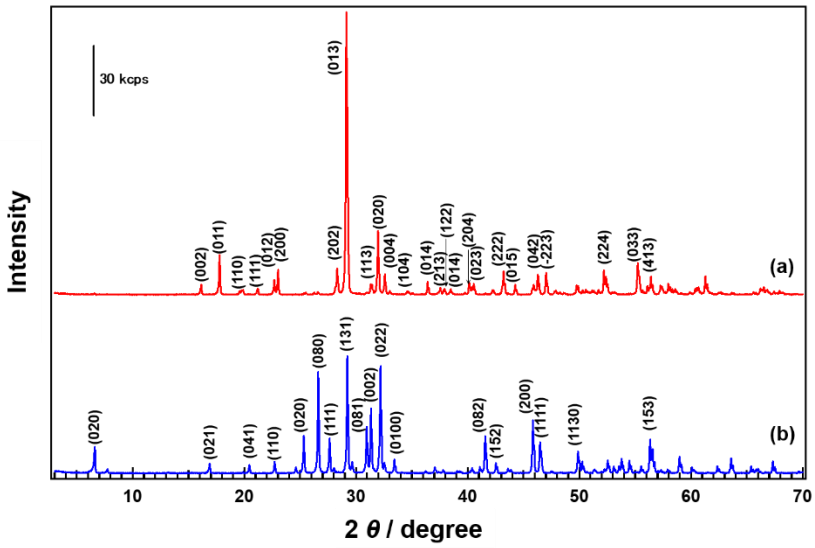

Figure 1 XRD patterns of (a) $SrNb_2O_6$ and (b) $Sr_2Nb_2O_7$ fabricated by a flux method.

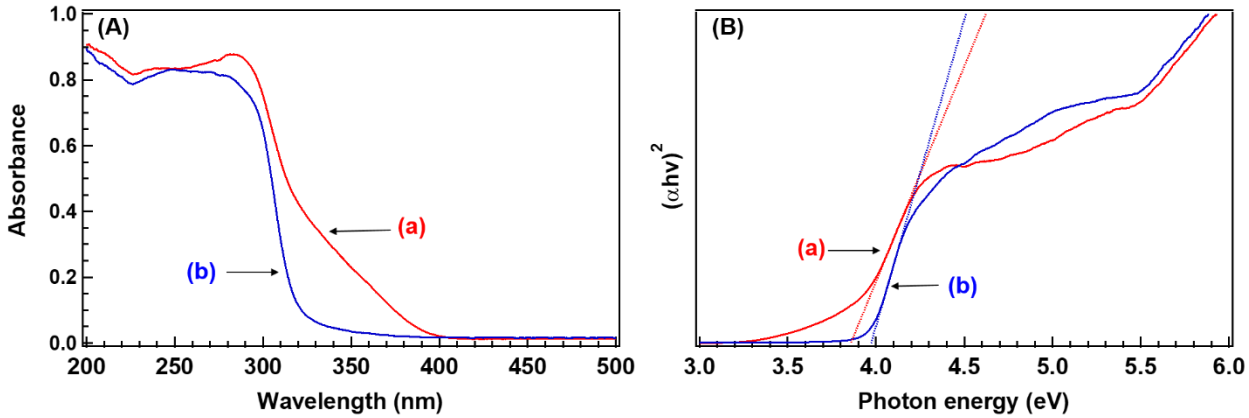

Figure 2 (A) UV-visible spectra, (B) Davis-Mott plot presenting $(\alpha hv)^2$ versus photon energy (hv) for the determination of band gap of as-synthesized (a) $SrNb_2O_6$ and (b)$Sr_2Nb_2O_7$ by a flux method.

Figure 2A shows the UV–vis diffuse reflectance spectra of as-synthesized $SrNb_2O_6$ and $Sr_2Nb_2O_7$; diffuse reflectance spectra were converted to absorption spectra using the Kubelka–Munk equation. The band gaps of $Sr_2Nb_2O_7$ and $SrNb_2O_6$ were estimated as 3.97 eV and 3.86 eV, respectively (Figure 2B), based on the Davis–Mott equation[40] using the Kubelka–Munk function $F(R_\infty)$ obtained from the diffuse-reflectance spectrum; these values are similar to the reported values.[31, 32]

$$[F(R_\infty)\, hv] = A\,(hv - E_g)^n \quad (3)$$

Here, h, v, A, and n = 1/2 represent the Planck's constant, vibrational frequency, proportionality constant, and direct allowed transition, respectively.

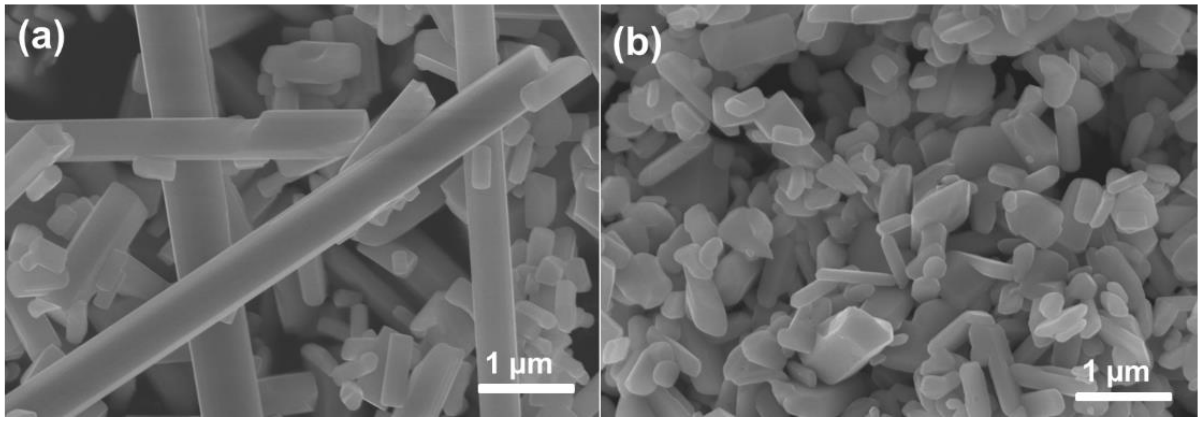

Figure 3 SEM images of as-prepared (a) $SrNb_2O_6$ and (b) $Sr_2Nb_2O_7$ prepared by the flux method.

Figure 3 shows the SEM images of as-prepared $SrNb_2O_6$ and $SrNb_2O_7$. $SrNb_2O_6$ predominantly consisted of 1D rod-like particles (Figure 3a). The diameters of the nanorods ranged from 100 nm to 1 μm, and their lengths ranged from 500 nm to several tens of microns. On the other hand, $Sr_2Nb_2O_7$ prepared by the same flux method predominantly exhibited a nanoflake structure with a thickness of 50–250 nm (Figure 3b). The surface areas of $SrNb_2O_6$ nanorod and $SrNb_2O_7$ nanoflake were 1.78 $m^2\ g^{-1}$ and 3.85 $m^2\ g^{-1}$, respectively.

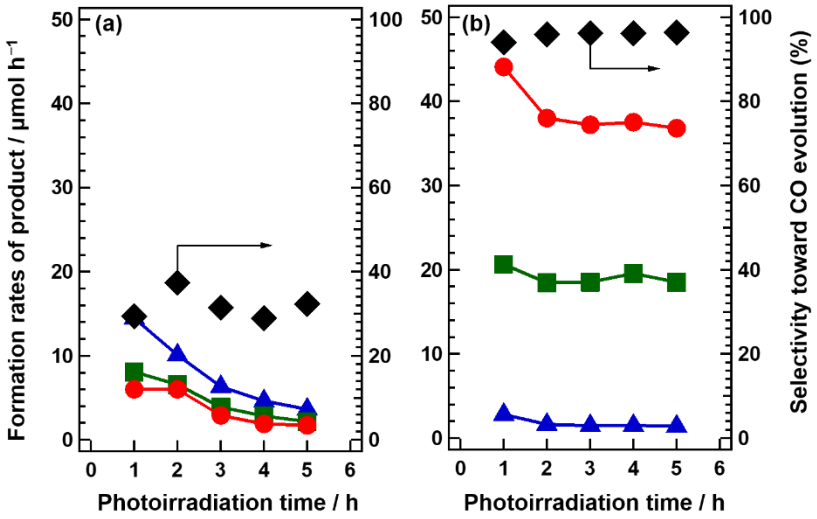

Figure 4 Formation rates of H_2 (blue triangles), O_2 (green squares), CO (red circles), and the selectivity toward CO evolution (black diamonds) for the photocatalytic conversion of CO_2 in an aqueous $NaHCO_3$ solution using (a) $Ag/Sr_2Nb_2O_7$ and (b) $Ag/SrNb_2O_6$ as the photocatalysts. Photocatalyst powder: 0.5 g, reaction solution volume: 1.0 L, additive: 0.1 M $NaHCO_3$, Ag loading amount: 1.0 wt.%, modification method: chemical reduction, CO_2 flow rate: 30 mL min^{-1}, light source: 400 W high-pressure Hg lamp.

Figure 4 shows the formation rates of H_2, O_2, and CO for the photocatalytic conversion of CO_2 by H_2O over $Ag/SrNb_2O_6$ and $Ag/Sr_2Nb_2O_7$ under UV light irradiation. Ag (1.0 wt.%) was loaded as the co-catalyst on the sample surface by chemical reduction method. The surface areas of $Ag/SrNb_2O_6$ and $Ag/SrNb_2O_7$ were 2.25 m^2 g^{-1} and 4.26 m^2 g^{-1}, respectively; these values are slightly greater than that of the bare catalyst. High selectivity (greater than 95%) toward the photocatalytic evolution of CO over $Ag/SrNb_2O_6$ was observed. CO was obtained as the main product (44.1 μmol h^{-1}), with marginal amounts of H_2 (2.7 μmol h^{-1}). A stoichiometric formation amount of O_2 (22.4 μmol h^{-1}), in addition to H_2 and CO, was observed, indicating that H_2O serves as the electron donor for the photocatalytic reduction of CO_2. On the other hand, compared to $Ag/SrNb_2O_6$, $Ag/Sr_2Nb_2O_7$ exhibited lower formation rates of H_2, CO, and O_2; H_2 was the main product; and the photocatalytic activity also rapidly decreased after photoirradiation for 5 h. This result clearly indicated that $Ag/SrNb_2O_6$ with a nanorod structure exhibits better photocatalytic activity and higher selectivity toward CO evolution compared

to Ag/$Sr_2Nb_2O_7$ with a nanoflake structure.

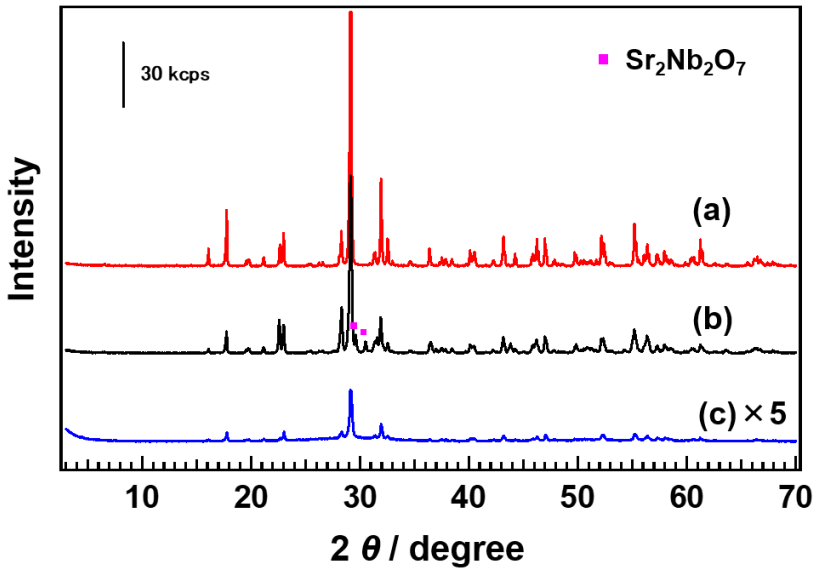

Figure 5 XRD patterns of $SrNb_2O_6$ prepared using different methods: (a) Flux (red). (b) SSR (black), and (c) solvothermal methods (blue).

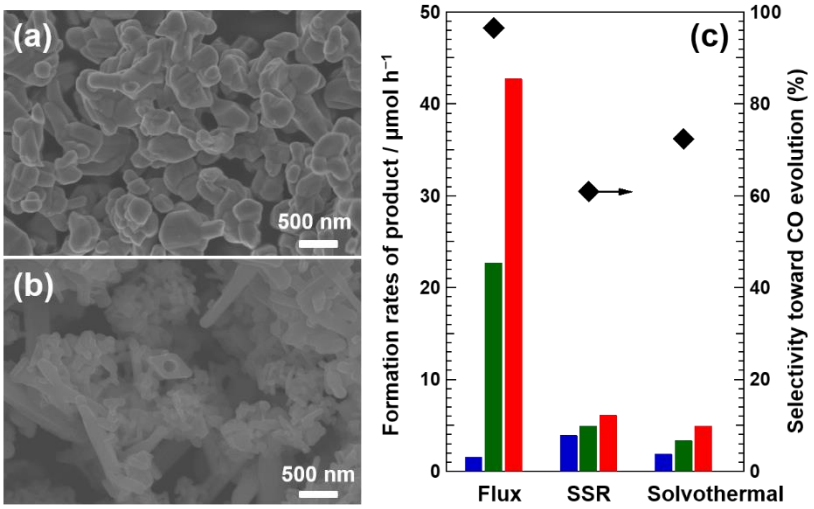

Figure 6 SEM images of the $SrNb_2O_6$ products prepared using different methods: (a) SSR method, (b) Solvothermal method; (c) Formation rates of H_2 (blue), O_2 (green), and CO (red) and the selectivity toward CO evolution (black diamond) for the photocatalytic conversion of CO_2 in an aqueous. Photocatalyst powder: 0.5 g, reaction solution volume: 1.0 L, additive: 0.1 M $NaHCO_3$, Ag loading amount: 1.0 wt.%, modification method: chemical reduction, CO_2 flow rate: 30 mL min^{-1}, light source: 400 W high-pressure Hg lamp.

As $SrNb_2O_6$ and $Sr_2Nb_2O_7$ exhibited different structures, $SrNb_2O_6$ with a nanorod structure was compared with catalysts with other nanostructures synthesized by the solid-state reaction (SSR) and solvothermal methods. As shown in the XRD patterns (Figure 5), a pure $SrNb_2O_6$ phase was successfully prepared, except using the SSR method, which contained few impurity phases of $Sr_2Nb_2O_7$. From the SEM images shown in Figure 6, aggregated nanoparticles (Figure 6a) and a mixture of nanoparticles and nanorods (Figure 6b) were observed for $SrNb_2O_6$ fabricated by SSR and the solvothermal method, respectively. All of the Ag-loaded $SrNb_2O_6$ products were favorable for CO evolution; however, $SrNb_2O_6$ nanorods prepared by the flux method exhibited higher photocatalytic activity and selectivity toward CO evolution compared to the aggregated nanoparticles prepared by SSR and the solvothermal method (Figure 6c). On the other hand, the nanorod-containing $SrNb_2O_6$ products prepared by the solvothermal method also exhibited higher photocatalytic selectivity toward CO evolution although its photocatalytic activity was less than that of the $SrNb_2O_6$ nanoparticles synthesized by the SSR method. This result revealed that $Ag/SrNb_2O_6$ is promising for the photocatalytic conversion of CO_2, and the nanorod structure is favorable for CO evolution, the reasons for the high selectivity toward CO evolution of $SrNb_2O_6$ nanorod will be discussed later.

Figure 7 shows the blank tests using the $SrNb_2O_6$ nanorods. No product was detected in the dark (Figure 7a) and without a photocatalyst (Figure 7b). Marginal amounts of H_2 and O_2 were observed, while the formation rates of CO were rather low without a $NaHCO_3$ additive and a Ag co-catalyst (Figures 7c and 7d), indicating that the $NaHCO_3$ additive and Ag co-catalyst are indispensable for the photocatalytic conversion of CO_2 in an aqueous solution. The use of inert Ar instead of CO_2 led to the decreased formation rate of evolved CO (Figure 7e). The best performance for the photocatalytic conversion of CO_2 was using Ag-loaded $SrNb_2O_6$ nanorods in an aqueous $NaHCO_3$ solution with bubbling CO_2 under photoirradiation (Figure 7f). From the photocatalytic result mentioned above, the $SrNb_2O_6$ nanorods clearly exhibited good activity for the photocatalytic conversion of CO_2 by H_2O under UV irradiation. The stoichiometric formation amount of H_2, CO, and O_2 indicated that H_2O serves as electron donor for the photocatalytic reduction of CO_2.

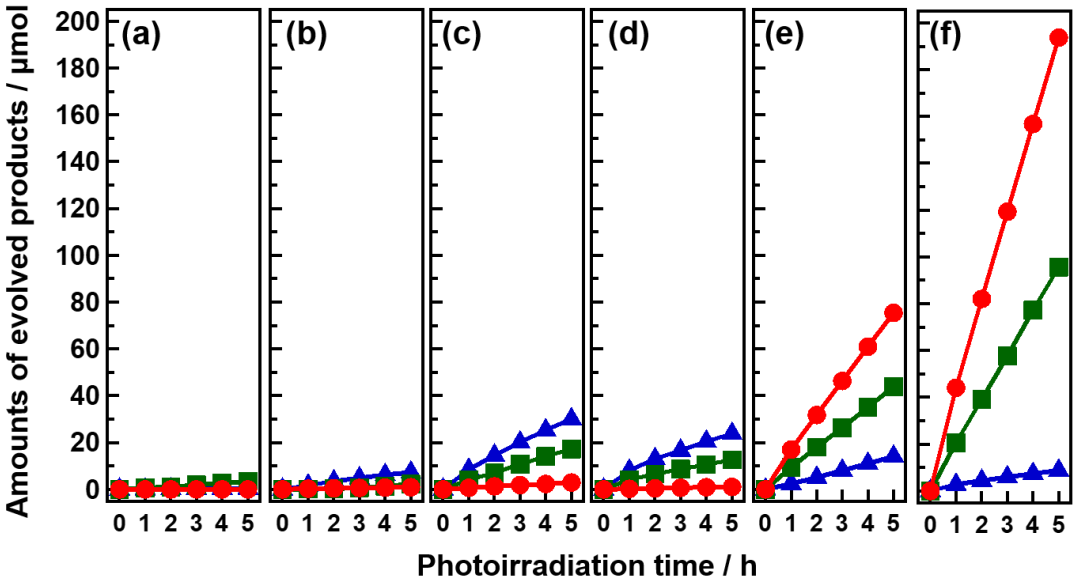

Figure 7 Amounts of H_2 (blue triangles), O_2 (green squares), and CO (red circles) from control experiments for the photocatalytic conversion of CO_2 in water using the $Ag/SrNb_2O_6$ photocatalyst. (a) dark condition; (b) no photocatalyst; (c) no additive; (d) no Ag co-catalyst; (e) with Ar gas flow; (f) typical condition. Photocatalyst powder: 0.5 g, reaction solution volume: 1.0 L, additive: 0.1 M $NaHCO_3$, Ag loading amount: 1.0 wt.%, modification method: chemical reduction, CO_2 flow rate: 30 mL min^{-1}, light source: 400 W high-pressure Hg lamp.

It is known that gaseous CO_2 can dissolve in an aqueous solution, whereas, it is negligible in pure water.[41] Adding additives in the aqueous solution could greatly affect the solubility of gaseous CO_2 and pH value into a reactant solution for CO_2 reduction.[42] The effects of bases on the photocatalytic conversion of CO_2 over $Ag/SrNb_2O_6$ are shown in Table 1. When $NaHCO_3$ (0.1 mol L^{-1}), Na_2CO_3 (0.05 mol L^{-1}), and NaOH (0.1 mol L^{-1}) were added into the reactant solution, it showed similar formation rates of products and pH values for the photocatalytic conversion of CO_2. Because CO_2 gas was continuously bubbled in solution, all the concentrations of CO_2 (aq), HCO_3^-, and CO_3^{2-} achieve equilibrium in case that Na_2CO_3 and NaOH are added as well as $NaHCO_3$.[42] In our previous work, the concentration of CO_2 (aq), HCO_3^-, and CO_3^{2-} in 0.1 mol L^{-1} $NaHCO_3$ aqueous solution were calculated under different pH values, which showed higher dissolved amount of CO_2 (aq) for the photocatalytic conversion of CO_2 (at pH = 6.8) as compared to that in the pure water.[43] Whereas, in the solutions of 0.05 mol L^{-1} H_2SO_4 and 0.1 mol L^{-1} NaCl, the SO_4^{2-} and Cl^- ions are hard to keep the high solubility

of gaseous CO_2 in solution, the concentrations of CO_2 related species are similar to that in H_2O during the bubbling of CO_2.[42] On the other hand, the high concentration of H^+ in H_2SO_4 and NaCl solutions is in favor of water splitting, so H_2 was the main products when H_2SO_4 and NaCl were used as additives.

Table 1 Effects of reactant solutions on the photocatalytic reduction of CO_2 over $Ag/SrNb_2O_6$.[a]

Additive (mol L^{-1})	pH[b]	Formation rate of products / μmol h^{-1}			Selec. toward CO (%)
		H_2	O_2	CO	
None	4.1	8.1	4.2	0.3	3.6
$NaHCO_3$ (0.1)	6.8	2.8	20.1	44.1	94.0
Na_2CO_3 (0.05)	7.0	2.2	23.0	49.7	95.8
NaOH (0.1)	6.9	3.8	24.4	45.2	92.3
NaCl (0.1)	3.9	10.7	5.8	1.2	9.8
H_2SO_4 (0.05)	1.3	176.5	85.0	0.1	0.1

[a] Photocatalyst powder: 0.5 g, reaction solution volume: 1.0 L, additive: 0.1 M $NaHCO_3$, Ag loading amount: 1.0 wt.%, modification method: chemical reduction, CO_2 flow rate: 30 mL min^{-1}, light source: 400 W high-pressure Hg lamp. [b] pH value of reaction solution during the photocatalytic reduction of CO_2.

Figure 8 shows the gas chromatograms and mass spectra for the photocatalytic conversion of $^{13}CO_2$ by H_2O over $Ag/SrNb_2O_6$. Peaks corresponding to H_2, O_2, and CO were observed in the TCD-GC chromatogram. The peak at m/z = 29 corresponded to ^{13}CO; in contrast, no peak was detected at m/z = 28. Therefore, CO evolved over $Ag/SrNb_2O_6$ originates from the CO_2 introduced in the gas phase and not from the residual organic contaminants on the surface.

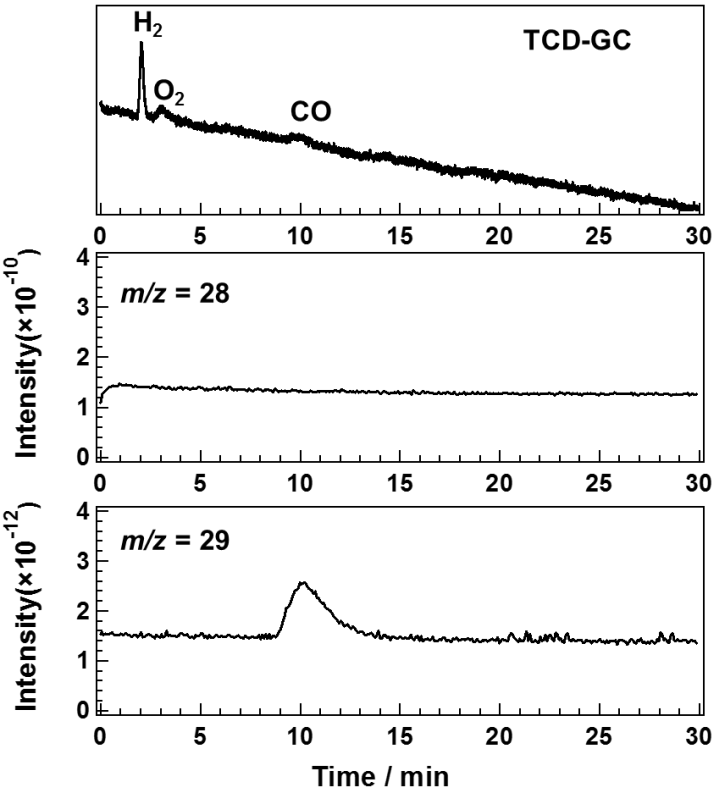

Figure 8 Gas chromatograms and mass spectra (*m/z* 28, 29) for the photocatalytic conversion of $^{13}CO_2$ by H_2O over $Ag/SrNb_2O_6$. Photocatalyst powder: 0.5 g, reaction solution volume: 1.0 L, Ag loading amount: 1.0 wt.%, modification method: chemical reduction, $^{13}CO_2$ gas flow rate: 30 mL min^{-1}, light source: 400 W high-pressure Hg lamp.

Loading with Ag has been reported to affect the activity and selectivity for the photocatalytic reduction of CO_2.[25] Figure 9 shows the formation rates of H_2, O_2, and CO for the photocatalytic conversion of CO_2 in an aqueous $NaHCO_3$ solution using $Ag/SrNb_2O_6$ modified by CR, IMP, and PD method. Ag-loaded $SrNb_2O_6$ prepared by all methods exhibited high photocatalytic selectivity toward CO evolution, and stoichiometric formation amount of H_2, CO, and O_2 were obtained. The amount of CO obtained as the reduction product of CO_2 over $Ag/SrNb_2O_6$ prepared by CR method was greater than those obtained by IMP and PD methods. The photocatalytic activity clearly decreased after photoirradiation for 1 h and gradually became stable with the increase in the photoirradiation time using CR methods. However, the evolution rate of CO only slightly decreased during photoirradiation for 5 h by the loading of Ag using PD method.

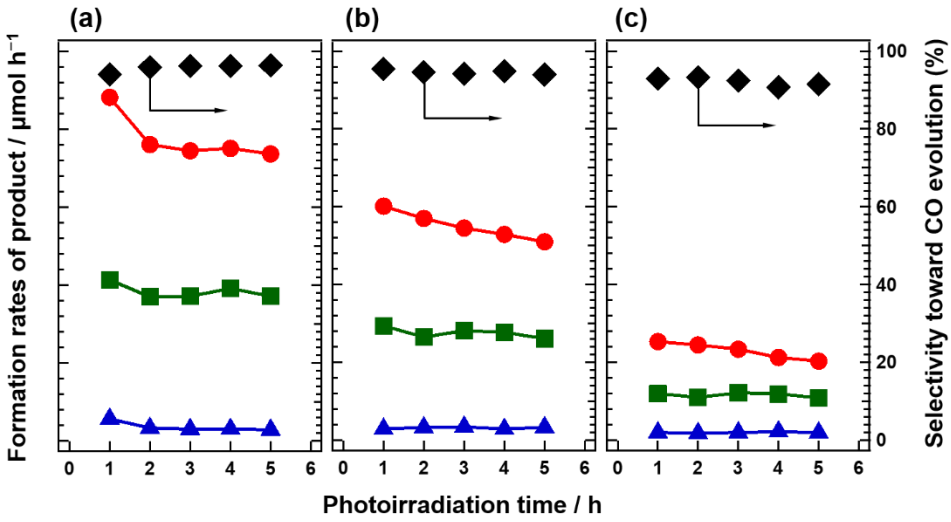

Figure 9 Formation rates of H_2 (blue triangle), O_2 (green square), CO (red circle), and the selectivity toward CO evolution (black diamond) for the photocatalytic conversion of CO_2 in an aqueous $NaHCO_3$ solution using Ag-modified $SrNb_2O_6$ by (a) CR, (b) IMP, and (c) PD methods. Photocatalyst powder: 0.5 g, reaction solution volume: 1.0 L, additive: 0.1 M $NaHCO_3$, Ag loading amount: 1.0 wt.%, CO_2 flow rate: 30 mL min^{-1}, light source: 400 W high-pressure Hg lamp.

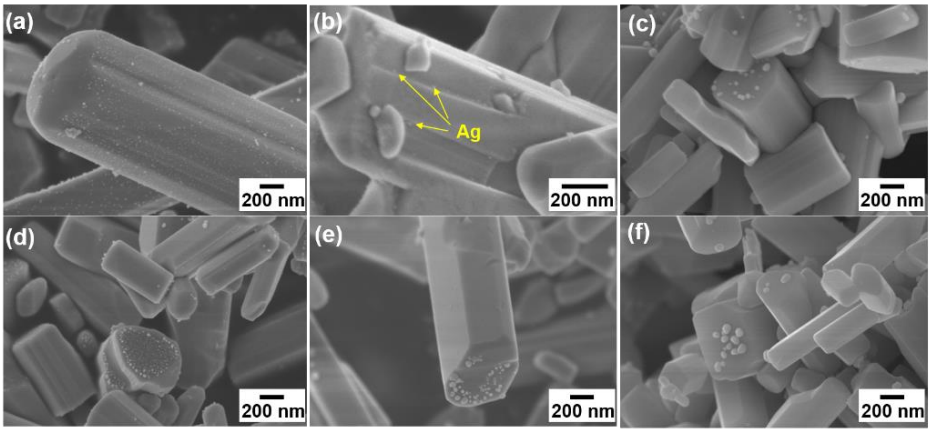

Figure 10 SEM images of $SrNb_2O_6$ modified with Ag by (a), (d) CR, (b), (e) IMP, and (c), (f) PD methods. (a–c) before and (d–f) after photoirradiation for 1 h. Ag loading amount: 1.0 wt.%.

Figure 10 shows the SEM images of $Ag/SrNb_2O_6$ prepared by the three methods. Ag particles modified by CR method were uniformly scattered on the $SrNb_2O_6$ nanorod surface with a size less than

10 nm (Figure 10a). Ag co-catalysts prepared by IMP method were dispersed on the surface of $SrNb_2O_6$ nanorod with an aggregate size of 10–50 nm (Figure 10b). The Ag co-catalysts prepared by PD method were predominantly deposited on the top of $SrNb_2O_6$ nanorods as nanoparticles with a size of 30–70 nm (Figure 10c). This selective deposition of Ag co-catalysts was also observed for Ag/$SrNb_2O_6$ prepared by CR and IMP methods at a photoirradiation time of 1 h (Figures 10d and 10e). The sizes of the Ag particles, which were prepared by CR and IMP methods, redeposited on the top of nanorods were 10–30 nm and 20–70 nm, respectively. The particle size of Ag on the top of nanorods was almost similar to the initial size of Ag/$SrNb_2O_6$ prepared by PD method after photoirradiation for 5 h (Figure 10f). Ag particles loaded on the top plane with a smaller size prepared by CR method exhibited higher photocatalytic activity for the reduction of CO_2 than those prepared by IMP and PD method. This result is consistent with those reported previously.[14]

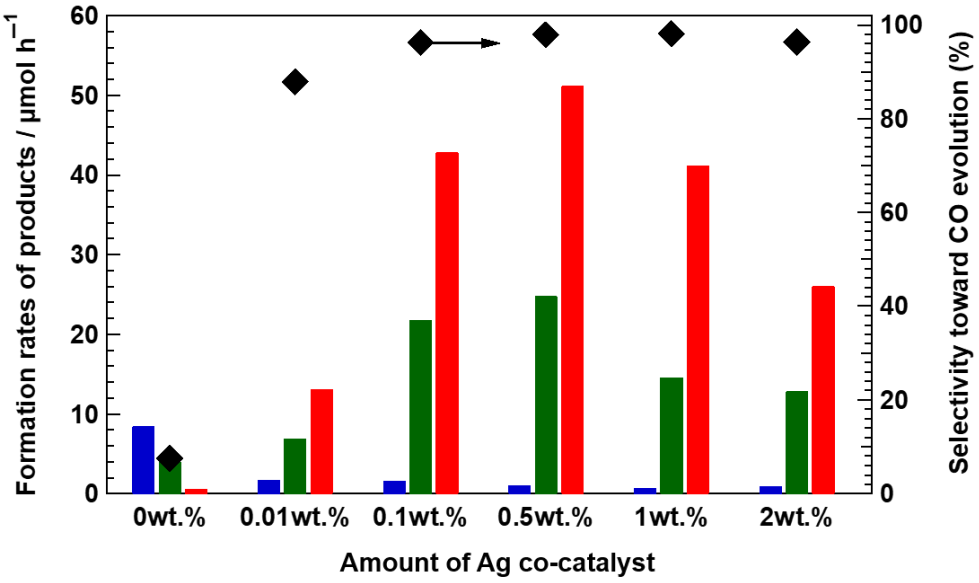

Figure 11 Formation rates of H_2 (blue), O_2 (green), and CO (red) and selectivity toward CO (black diamond) evolution for the photocatalytic conversion of CO_2 in an aqueous $NaHCO_3$ solution using the $SrNb_2O_6$ photocatalyst modified with different contents of Ag. Photocatalyst powder: 0.5 g, reaction solution volume: 1.0 L, additive: 0.1 M $NaHCO_3$, modification method: chemical reduction, CO_2 flow rate: 30 mL min^{-1}, light source: 400 W high-pressure Hg lamp.

Figure 11 shows the effect of the Ag co-catalyst loading amount on the photocatalytic activity for CO_2 conversion. Modification of the catalyst with marginal amounts of Ag dramatically improved the

formation rate of CO and suppressed the formation rate of H_2, indicating that the modification of the Ag co-catalyst leads to increased reaction sites on the $SrNb_2O_6$ nanorod surface for the reduction of CO_2 because of its good selectivity toward CO evolution.[28] As the active sites for reduction increased with increasing amounts of added Ag co-catalyst, the formation rate of CO increased with the addition of a large amount of Ag from 0 to 0.5 wt.%. However, further increase in the amount of Ag led to the aggregation of Ag particles; hence, the photocatalytic activity decreases with the further modification by Ag with a loading from 0.5 to 2 wt.%. The particle size of the Ag co-catalysts increased with the increase in the Ag loading amount, followed by gradual aggregation, which was clearly observed from the SEM and TEM images in Figure 12. The highest formation rate of the evolved CO (51.2 μmol h^{-1}) was observed using 0.5 wt.% Ag-loaded $SrNb_2O_6$ nanorods, as well as high selectivity (98%), although the conversion efficiency was very low (0.06%).

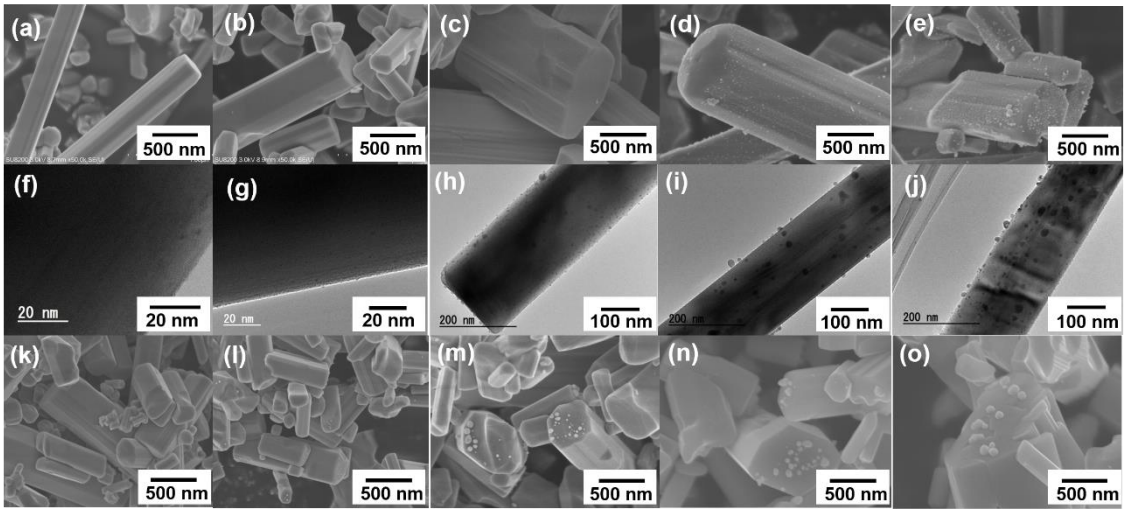

Figure 12 SEM images of $SrNb_2O_6$ nanorod modified with different contents of Ag (CR method) before photoirradiation: (a) 0.01, (b) 0.1, (c) 0.5; (d) 1.0, (e) 2.0 wt.%, TEM images of $SrNb_2O_6$ nanorod modified with different contents of Ag (CR method) before photoirradiation: (f) 0.01, (g) 0.1, (h) 0.5; (i) 1.0, (j) 2.0 wt.%; SEM images of $SrNb_2O_6$ nanorod modified with different contents of Ag (CR method) after photoirradiation for 5 h: (k) 0.01, (l) 0.1, (m) 0.5; (n) 1.0, (o) 2.0 wt.%.

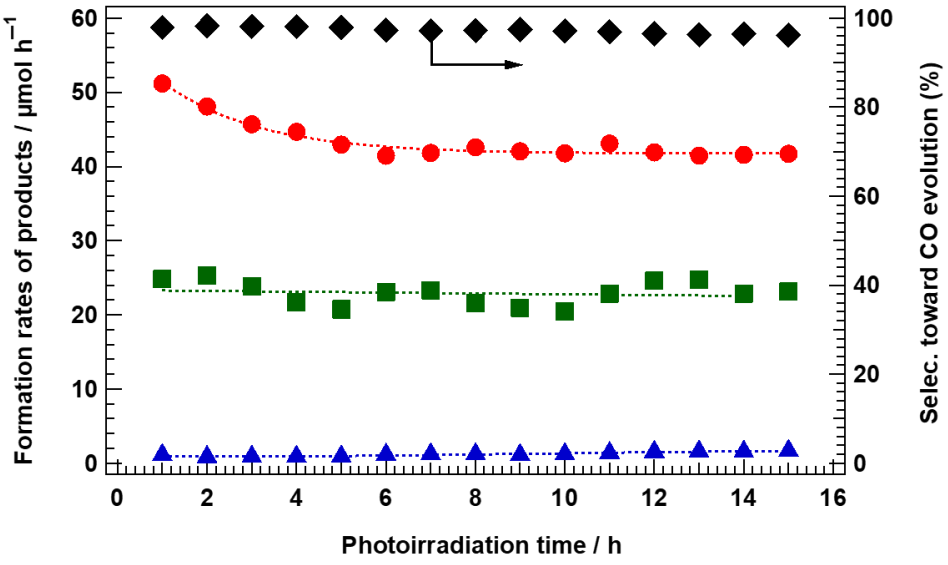

Figure 13 Time course for the evolution of CO (red circle), O_2 (green square), and H_2 (blue triangle) evolution and the selectivity toward CO evolution (black diamond) for the photocatalytic conversion of CO_2 in an aqueous $NaHCO_3$ solution using $Ag/SrNb_2O_6$. Photocatalyst powder: 0.5 g, reaction solution volume: 1.0 L, additive: 0.1 M $NaHCO_3$, Ag loading amount: 0.5 wt.%, modification method: chemical reduction, CO_2 flow rate: 30 mL min^{-1}, light source: 400 W high-pressure Hg lamp.

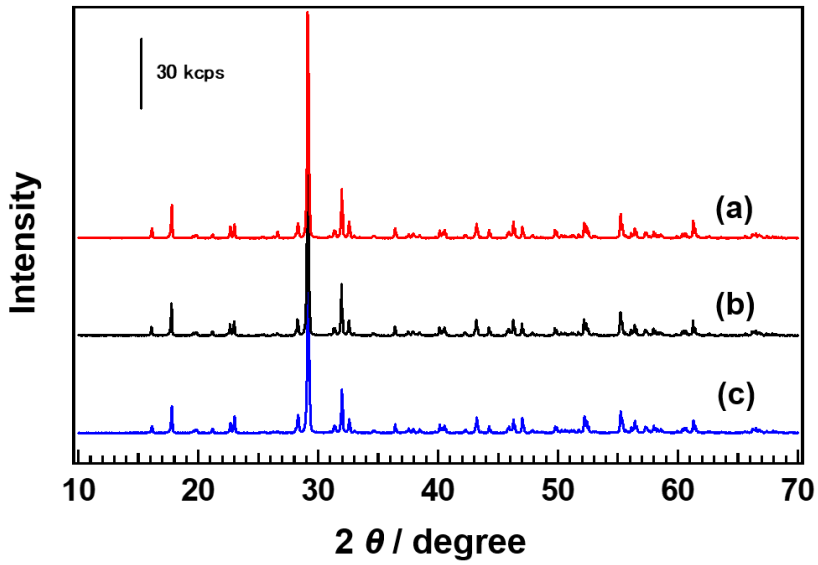

Figure 14 XRD patterns of $Ag/SrNb_2O_6$ with different photoirradiation time: (a) 0 h (red), (b) 6 h (black), and (c)15 h (blue). Ag loading amount: 1.0 wt.%, modification method: chemical reduction.

Figure 13 shows the time course for the evolution of CO, H_2, and O_2 during the photocatalytic conversion of CO_2 by H_2O over 0.5 wt.% Ag-loaded $SrNb_2O_6$. Stable selectivity toward CO was observed during photoirradiation (approximately 97%). CO was evolved as the main reduction product, and marginal amounts of H_2 were generated. Stoichiometric amounts of O_2 as the oxidation product of H_2O were obtained, in addition to CO and H_2 as the reduction products, suggesting that H_2O serves as the electron donor for the photocatalytic conversion of CO_2. Notably, the formation rate of CO gradually decreased with the increase in the photoirradiation time for the first 6 h and then was maintained constant. As shown in the XRD pattern (Figure 14), the crystalline structures of $SrNb_2O_6$ were very stable under UV light irradiation, while the diffraction peak corresponding to metallic Ag was not observed because of the low amount of Ag.

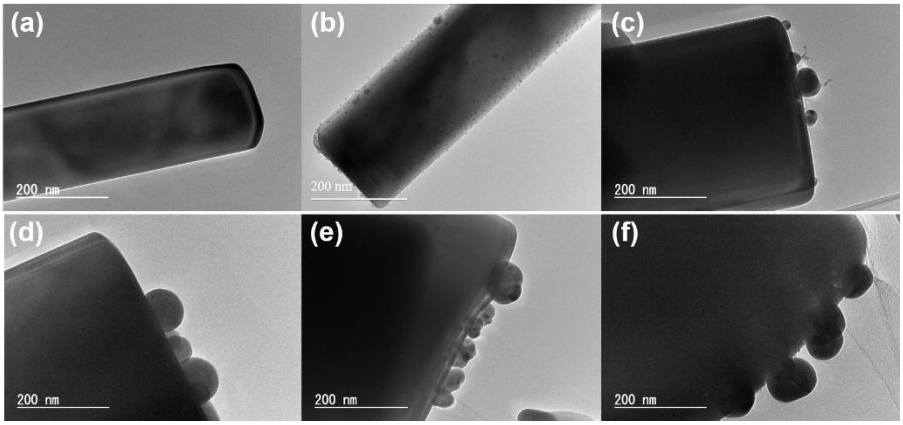

Figure 15 TEM images of (a) $SrNb_2O_6$ and Ag-loaded $SrNb_2O_6$ nanorods at different photoirradiation times: (b) 0 h, (c) 3 h, (d) 6 h, (e) 10 h, (f) 15 h. Ag loading amount: 0.5 wt.%, modification method: chemical reduction.

Figure 15 shows the TEM images, which clearly show the variation of Ag particles on the $SrNb_2O_6$ nanorod surface. Before the loading of Ag, a smooth $SrNb_2O_6$ nanorod surface was observed (Figure 15a). After the loading of the Ag co-catalyst by CR method, Ag nanoparticles with a size less than 10 nm were highly dispersed on the $SrNb_2O_6$ nanorod surface (Figure 15b), which were selectively redeposited on the top of the $SrNb_2O_6$ nanorod with photoirradiation (Figure 15c). The particle size of Ag increased with the increase in the photoirradiation time from 0 h to 6 h (Figure 15d) and gradually maintained constant with the further increase in the photoirradiation time to 15 h (Figure

15e and 15f). The variation of Ag particles could also be confirmed by EDS analysis (Figure 16).

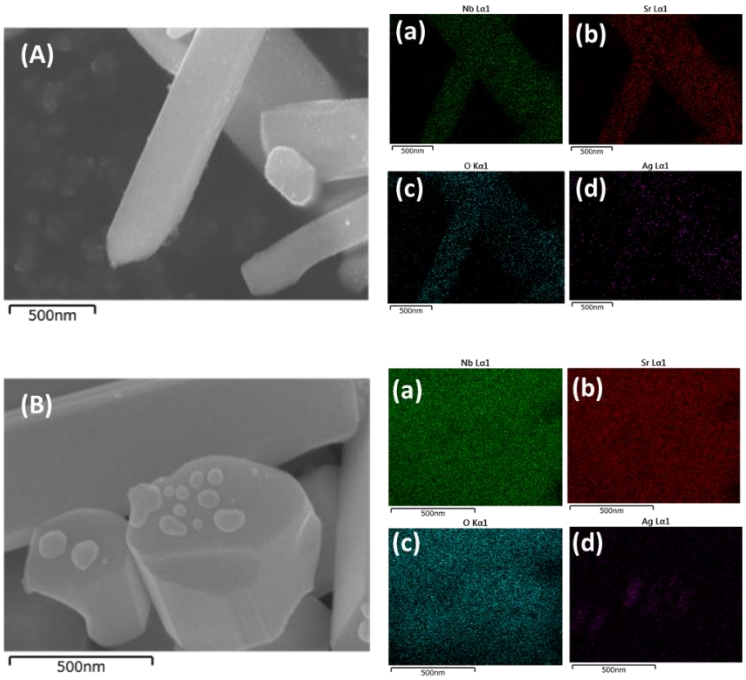

Figure 16 EDS analysis of Ag-loaded $SrNb_2O_6$ nanorod with different photoirradiation time. Selected SEM images (A) 0 h, (B) 5 h; (a) Nb, (b) Sr, (c) O, (d) Ag mapping images. Ag loading amount: 1.0 wt.%, modification method: chemical reduction.

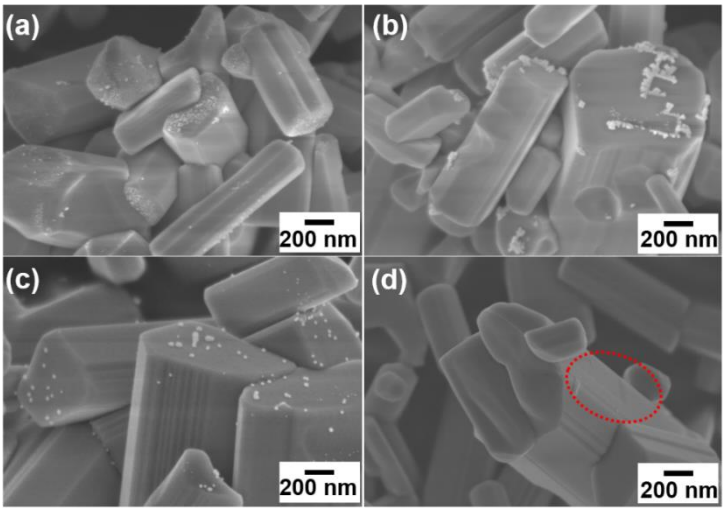

Figure 17 SEM images of various metals and PbO_2 loaded on $SrNb_2O_6$ nanorod by a photodeposition method; (a) Pt, (b) Pd, (c)Au, and (d) Pb_2O. Loading amount: 1.0 wt.%, modification method: photodeposition.

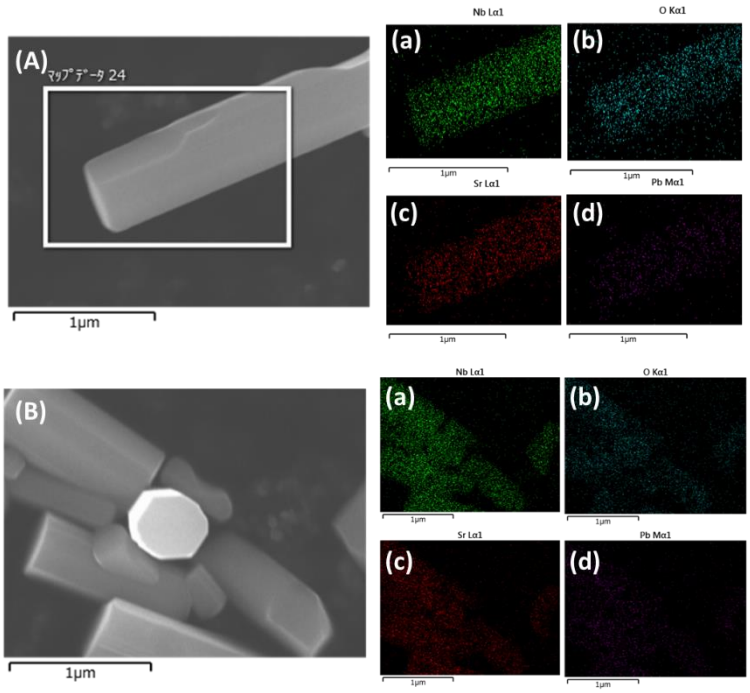

Figure 18 EDS analysis of PbO_2-loaded $SrNb_2O_6$ nanorod with different exposed plane. Selected SEM images (A) side plane, (B) top plane; (a) Nb, (b) Sr, (c) O, (d) Pb mapping images. PbO_2 loading amount: 1.0 wt.%, modification method: photodeposition.

Pt and PbO_2 have been reported to be reductively and oxidatively photodeposited, respectively, on surfaces because of their anisotropic properties.[38, 44] Hence, a series of metals and PbO_2 is examined to investigate the anisotropy property of the $SrNb_2O_6$ nanorod (Figure 17). Metallic Au, Pt, and Pd were reductively photodeposited from $[AuCl_4]^-$, $[PtCl_6]^{2-}$, and Pd^{2+} on the top plane of the nanorod, respectively. In contrast, PbO_2 was selectivity deposited from Pb^{2+} on the side plane of the nanorod, which was also confirmed by EDS (Figure 18). This selective photodeposition of different materials demonstrated that reduction and oxidation by the photogenerated e^- and h^+ primary occur on the top and side planes of the nanorods, respectively, indicating that Ag loaded on the $SrNb_2O_6$ surface in this study is firstly dissolved by the photogenerated holes to Ag^+ and then redeposited on the top plane under photoirradiation because of the anisotropy of the $SrNb_2O_6$ nanorod.

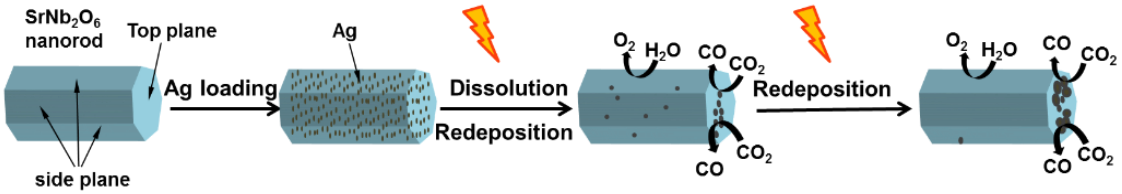

Scheme 1 Possible mechanism for the redeposition of the Ag co-catalyst on the Ag/$SrNb_2O_6$ nanorod surface

Scheme 1 shows the possible mechanism for the redeposition of the Ag co-catalyst on the Ag/$SrNb_2O_6$ nanorod surface. The photocatalytic reduction of CO_2 predominantly led to the formation of CO on the top of the Ag-loaded $SrNb_2O_6$ nanorods, while O_2 was formed on the sides of the nanorods. The variation of the Ag particles on the $SrNb_2O_6$ nanorod surface, which were dissolved and redeposited on the top of $SrNb_2O_6$ nanorod possibly led to the decreased Ag active sites; hence, the photocatalytic activity decreases during photoirradiation, especially in the first 1 h. The separation of the reduction sites from the oxidation sites contributed to the decrease in the recombination of the photogenerated carriers; hence, Ag-loaded $SrNb_2O_6$ nanorods prepared by the flux method exhibit good activity and selectivity for the photocatalytic conversion of CO_2.

Conclusion

$SrNb_2O_6$ nanorods and $Sr_2Nb_2O_7$ nanoflakes were successfully synthesized by a flux method. $SrNb_2O_6$ with a nanorod structure exhibited higher photocatalytic activity and selectivity toward CO evolution for the photocatalytic conversion of CO_2 compared to $Sr_2Nb_2O_7$ nanoflakes and $SrNb_2O_6$ particles. Ag particles loaded on the $SrNb_2O_6$ nanorod surface with a smaller size exhibited higher photocatalytic activity for CO_2 conversion. The Ag co-catalysts loaded by CR method were uniformly loaded on the $SrNb_2O_6$ nanorod surface, followed by the selective re-deposition on the top of $SrNb_2O_6$ nanorod during photoirradiation. The separation of the reduction and oxidation sites was considered to be crucial for the high photocatalytic activity and selectivity toward CO evolution for CO_2 conversion.

References

1. J. Hansen, L. Nazarenko, R. Ruedy, M. Sato, J. Willis, A. Del Genio, D. Koch, A. Lacis, K. Lo and S. Menon, *Science*, 2005, **308**, 1431-1435.
2. W. Wang, S. Wang, X. Ma and J. Gong, *Chem. Soc. Rev.*, 2011, **40**, 3703-3727.
3. M. Mikkelsen, M. Jørgensen and F. C. Krebs, *Energy Environ. Sci.*, 2010, **3**, 43-81.
4. A. J. Morris, G. J. Meyer and E. Fujita, *Acc. Chem. Res.*, 2009, **42**, 1983-1994.
5. T. Inoue, A. Fujishima, S. Konishi and K. Honda, *Nature*, 1979, **277**, 637-638.
6. B. Kumar, M. Llorente, J. Froehlich, T. Dang, A. Sathrum and C. P. Kubiak, *Annu. Rev. Phys. Chem.*, 2012, **63**, 541-569.
7. R. K. Yadav, G. H. Oh, N.-J. Park, A. Kumar, K.-j. Kong and J.-O. Baeg, *J. Am. Chem. Soc.*, 2014, **136**, 16728-16731.
8. G. Qin, Y. Zhang, X. Ke, X. Tong, Z. Sun, M. Liang and S. Xue, *Appl. Catal. B*, 2013, **129**, 599-605.
9. E. V. Kondratenko, G. Mul, J. Baltrusaitis, G. O. Larrazábal and J. Pérez-Ramírez, *Energy Environ. Sci.*, 2013, **6**, 3112-3135.
10. M. Asadi, B. Kumar, A. Behranginia, B. A. Rosen, A. Baskin, N. Repnin, D. Pisasale, P. Phillips, W. Zhu and R. Haasch, *Nat. Commun.*, 2014, **5**, 4470.
11. Q. Lu, J. Rosen, Y. Zhou, G. S. Hutchings, Y. C. Kimmel, J. G. Chen and F. Jiao, *Nat. Commun.*, 2014, **5**, 3242.
12. H. Inoue, T. Matsuyama, B. J. Liu, T. Sakata, H. Mori and H. Yoneyama, *Chem. Lett*, 1994, 653-656.
13. N. M. Dimitrijevic, B. K. Vijayan, O. G. Poluektov, T. Rajh, K. A. Gray, H. He and P. Zapol, *J. Am. Chem. Soc.*, 2011, **133**, 3964-3971.
14. K. Iizuka, T. Wato, Y. Miseki, K. Saito and A. Kudo, *J. Am. Chem. Soc.*, 2011, **133**, 20863-20868.
15. C. Wang, R. L. Thompson, J. Baltrus and C. Matranga, *J. Phys. Chem. Lett.*, 2009, **1**, 48-53.
16. Q. Kang, T. Wang, P. Li, L. Liu, K. Chang, M. Li and J. Ye, *Angew. Chem. Int. Ed.*, 2015, **54**, 841-845.
17. L. Zhang, W. Wang, D. Jiang, E. Gao and S. Sun, *Nano Res.*, 2015, **8**, 821-831.

18. J.-C. Wang, H.-C. Yao, Z.-Y. Fan, L. Zhang, J.-S. Wang, S.-Q. Zang and Z.-J. Li, *ACS Appl. Mater. Interfaces*, 2016, **8**, 3765-3775.
19. J. L. White, M. F. Baruch, J. E. Pander III, Y. Hu, I. C. Fortmeyer, J. E. Park, T. Zhang, K. Liao, J. Gu and Y. Yan, *Chem. Rev.*, 2015, **115**, 12888-12935.
20. J. Mao, K. Li and T. Peng, *Catal. Sci. Technol.*, 2013, **3**, 2481-2498.
21. K. Teramura, Z. Wang, S. Hosokawa, Y. Sakata and T. Tanaka, *Chem. – Eur. J.*, 2014, **20**, 9906-9909.
22. Z. Wang, K. Teramura, Z. Huang, S. Hosokawa, Y. Sakata and T. Tanaka, *Catal. Sci. Technol.*, 2016, **6**, 1025-1032.
23. Z. Wang, K. Teramura, S. Hosokawa and T. Tanaka, *Appl. Catal. B*, 2015, **163**, 241-247.
24. K. Teramura, H. Tatsumi, Z. Wang, S. Hosokawa and T. Tanaka, *Bull. Chem. Soc. Jpn.*, 2015, **88**, 431-437.
25. Z. Wang, K. Teramura, S. Hosokawa and T. Tanaka, *J. Mater. Chem. A*, 2015, **3**, 11313-11319.
26. Z. Huang, K. Teramura, S. Hosokawa and T. Tanaka, *Appl. Catal. B*, 2016, **199**, 272-281.
27. S. Iguchi, K. Teramura, S. Hosokawa and T. Tanaka, *Catal. Sci. Technol.*, 2016, **6**, 4978-4985.
28. Y. Hori, H. Wakebe, T. Tsukamoto and O. Koga, *Electrochim. Acta*, 1994, **39**, 1833-1839.
29. M. Yamamoto, T. Yoshida, N. Yamamoto, T. Nomoto, Y. Yamamoto, S. Yagi and H. Yoshida, *J. Mater. Chem. A*, 2015, **3**, 16810-16816.
30. K. Domen, J. N. Kondo, M. Hara and T. Takata, *Bull. Chem. Soc. Jpn.*, 2000, **73**, 1307-1331.
31. I.-S. Cho, S. Lee, J. H. Noh, D. W. Kim, D. K. Lee, H. S. Jung, D.-W. Kim and K. S. Hong, *J. Mater. Chem.*, 2010, **20**, 3979-3983.
32. D. Chen and J. Ye, *Chem. Mater.*, 2009, **21**, 2327-2333.
33. O. C. Compton, C. H. Mullet, S. Chiang and F. E. Osterloh, *J. Phys. Chem. C*, 2008, **112**, 6202-6208.
34. Q.-P. Ding, Y.-P. Yuan, X. Xiong, R.-P. Li, H.-B. Huang, Z.-S. Li, T. Yu, Z.-G. Zou and S.-G. Yang, *J. Phys. Chem. C*, 2008, **112**, 18846-18848.
35. H. Shi and Z. Zou, *J. Phys. Chem. Solids*, 2012, **73**, 788-792.
36. P. Li, S. Ouyang, Y. Zhang, T. Kako and J. Ye, *J. Mater. Chem. A*, 2013, **1**, 1185-1191.
37. S. Xie, Y. Wang, Q. Zhang, W. Deng and Y. Wang, *Chem. Commun.*, 2015, **51**, 3430-3433.

38. Y. Miseki, H. Kato and A. Kudo, *Energy Environ. Sci.*, 2009, **2**, 306-314.
39. Q. Liu, Y. Zhou, J. Kou, X. Chen, Z. Tian, J. Gao, S. Yan and Z. Zou, *J. Am. Chem. Soc.*, 2010, **132**, 14385-14387.
40. E. Davis and N. Mott, *Philos. Mag.*, 1970, **22**, 0903-0922.
41. E. Wilhelm, R. Battino and R. J. Wilcock, *Chem. Rev.*, 1977, **77**, 219-262.
42. H. Zhong, K. Fujii, Y. Nakano and F. Jin, *J. Phys. Chem. C*, 2014, **119**, 55-61.
43. K. Teramura, K. Hori, Y. Terao, Z. Huang, S. Iguchi, Z. Wang, H. Asakura, S. Hosokawa and T. Tanaka, *J. Phys. Chem. C*, 2017, **121**, 8711-8721.
44. T. Ohno, K. Sarukawa and M. Matsumura, *New J. Chem.*, 2002, **26**, 1167-1170.

Chapter 2

Evaluation of intermediate species for the photocatalytic conversion of CO_2 with bicarbonate as a carbon source over $Ag/SrNb_2O_6$

Abstract

In this study, $Ag/SrNb_2O_6$ nanorods exhibited a high CO formation rate and high selectivity toward CO evolution in aqueous solutions containing bicarbonate ions even without CO_2 bubbling. Notably, the formation rate of CO reached as high as 287 μmol h^{-1} with a selectivity toward CO evolution of higher than 94.1% when NH_4HCO_3 was used as an additive under the bubbling of Ar gas. Both the formation rate of CO and selectivity toward CO evolution increased with the concentration of HCO_3^-. According to the experimental results and analytical chemistry calculations, it was concluded that the CO_2(aq) obtained by the dissociation of HCO_3^- was the actual reactant for the photocatalytic conversion of CO_2. In contrast, the HCO_3^- species in the aqueous solution was beneficial for improving the photocatalytic activity and selectivity toward CO evolution by increasing the adsorption of carbon-related species on the surface of the photocatalyst and/or suppressing the backward reaction for the photocatalytic conversion of CO_2.

Introduction

The Climate Change 2014: Synthesis Report by the Intergovernmental Panel on Climate Change predicted that anthropogenic greenhouse gas (GHG) emissions since the pre-industrial era have driven large increases in atmospheric concentrations of carbon dioxide (CO_2). Without additional efforts to reduce GHG emissions, we will exceed 450 ppm CO_2-eq by 2030 and reach CO_2-eq concentration levels between about 750 and more than 1300 ppm CO_2-eq by 2100, which will have a disastrous impact on the global climate, environment, and economy.[1] Inspired by plant photosynthesis, one of the best strategies to mitigate CO_2 emissions is the photocatalytic conversion of CO_2 into other feedstocks such as CO, HCOOH, HCHO, CH_4, and CH_3CH_2OH by heterogeneous catalysts using H_2O as an electron donor.[2-7] Especially, the conversion of CO_2 into CO can be further used for syngas preparation based on the Fischer–Tropsch process.[8-10] Nevertheless, it is difficult to activate CO_2 selectively and suppress the H_2 evolution from protons (H^+) in aqueous solutions, because the redox potential of CO_2/CO (−0.521 V vs. NHE, pH = 7) is more negative than that of H^+/H_2 (−0.414 V vs. NHE, pH = 7).[3] To our knowledge, Kudo et al. reported for the first time that the formation of CO from CO_2 exceeds that of H_2 from H^+, and a stoichiometric amount of O_2 evolves as an oxidation product for the photocatalytic conversion of CO_2 in an aqueous solution over $Ag/BaLa_4Ti_4O_{15}$.[11] Subsequently, various Ag-loaded photocatalysts have been reported for the highly selective photocatalytic conversion of CO_2 into CO with H_2O as an electron donor.[12-15] Our group also found many photocatalysts that exhibit a high selectivity toward CO evolution for the photocatalytic conversion of CO by H_2O, such as Ag-modified $ZnGa_2O_4/Ga_2O_3$,[16, 17] $ZnGa_2O_4$,[18] $Sr_2KTa_5O_{15}$,[19] Mg-Al LDH/Ga_2O_3,[20] $K_2RETa_5O_{15}$,[21] and Ag-Cr-modified Ga_2O_3.[22]

According to previous isotopic experiments and in situ FT-IR spectroscopy measurements, it has been revealed that CO_2 dissolved in an aqueous solution (CO_2(aq)) will react with the hydroxyl group anchored on the surface and form bidentate bicarbonate, which acts as the intermediate species for the photocatalytic conversion of CO_2, where H_2O acts as the electron donor.[23] I found that CO_2(aq) functions as the reactant for the photocatalytic conversion of CO_2 toward CO evolution, and its concentration ([CO_2(aq)]) greatly influences the formation rate of CO and selectivity toward CO evolution. Based on our previous work,[16-19, 21, 23-25] the main reduction product was found to change

from CO to H_2 derived from water splitting when [CO_2(aq)] was too low. In fact, the solubility of CO_2 in pure H_2O was only about 0.033 mol L^{-1} (at 298 K under 1 atm).[26, 27] Moreover, the capture, storage, and transportation of CO_2 are very expensive. Thus, it is crucial to develop a photocatalyst that can achieve the highly selective and highly active photocatalytic conversion of CO_2 into CO at low CO_2 concentrations. Very recently, I found an interesting phenomenon where the formation rate of CO_2 was much higher than that of H_2 in an aqueous solution of $NaHCO_3$ even without the bubbling of CO_2 over Ag-modified $SrNb_2O_6$ (Ag/$SrNb_2O_6$).[28] This result indicates the potential of HCO_3^- as a carbon source for the photocatalytic conversion of CO_2. In this work, I investigated the photocatalytic performance for the conversion of CO_2 over Ag/$SrNb_2O_6$ with various bicarbonate salts as carbon sources, and further evaluated the intermediate species for the photocatalytic conversion of CO_2 through experiments and analytical chemistry calculations.

Experimental

Preparation of photocatalyst

$SrNb_2O_6$ was prepared by the flux method reported in our previous work.[28] Briefly, 2.0 g of Nb_2O_5 powder (99.9%, Wako) and 6.0 g of $SrCl_2 \cdot 6H_2O$ (99.9%, Wako) were ground in an alumina mortar for 5 min. The mixture was calcined in air using an alumina crucible at 1173 K for 2 h. After calcination, the obtained powder was thoroughly washed three times with hot water (353 K) to remove the residual salt and dried at 353 K in an oven. The impregnation method was used the modify 1.0 wt.% of Ag on the surface of the $SrNb_2O_6$ photocatalyst. Specifically, 1.5 g of the prepared $SrNb_2O_6$ was homogeneously dispersed in an aqueous $AgNO_3$ solution (20 mL), followed by evaporation at 358 K to remove water and calcination at 723 K for 2 h in air.

Characterization

The crystal phase of $SrNb_2O_6$ was observed by powder X-ray diffractometry (XRD; Rigaku Multiflex) with Cu Kα radiation (λ = 0.154 nm). Sample morphologies were observed by field-emission scanning electron microscopy (FE-SEM, SU8220, Hitachi High-Technologies) and transmission electron microscopy (TEM, JEM-2100F, JEOL).

Photocatalytic reaction

The photocatalytic conversion of CO_2 was carried out using a flow system with an inner-irradiation-type reaction vessel at ambient pressure. In ultrapure water (1.0 L) containing a certain concentration of additives, 0.5 g of the synthesized photocatalyst was dispersed. CO_2 and/or Ar gas were bubbled into the solution at a flow rate of 30 mL min^{-1}. The suspension was illuminated using a 400 W high-pressure mercury lamp with a quartz filter connected to a cooling water system. The amounts of the evolved H_2, O_2, and N_2 were detected using a thermal conductivity detector-gas chromatography (GC) system (Shimadzu Corp; MS-5A column, Ar carrier), and the amount of evolved CO was analyzed by a flame ionization detector-GC with a methanizer (ShinCarbon ST column, N_2 carrier). The selectivity toward CO evolution compared to the H_2 evolution and the balance between the consumed electrons (e^-) and holes (h^+) can be expressed by Eqn. (1) and (2), respectively:[2]

$$\text{Selectivity toward CO evolution (\%)} = 100 \times 2\boldsymbol{R}_{CO}/(2\boldsymbol{R}_{CO} + 2\boldsymbol{R}_{H2}) \quad (1)$$

$$\text{Consumed } e^-/h^+ = (2\boldsymbol{R}_{CO} + 2\boldsymbol{R}_{H2})/4\boldsymbol{R}_{O2} \quad (2)$$

Here, $\boldsymbol{R}_{CO}$ and $\boldsymbol{R}_{H2}$ represent the formation rates of CO and H_2, respectively.

Results and discussion

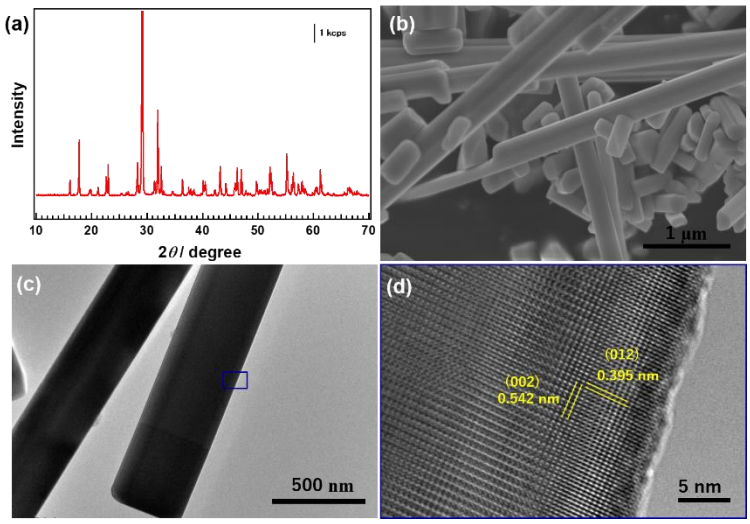

Figure 1 (a) XRD pattern, (b) SEM image, (c) TEM image, and (d) high-resolution TEM (HRTEM) image of $SrNb_2O_6$. (d) shows an enlarged HRTEM image of the blue rectangle in (c).

The crystal structures of $SrNb_2O_6$ were confirmed by powder XRD measurement, as illustrated in Figure 1a. All diffraction peaks in the XRD pattern can be exactly indexed to pure monoclinic $SrNb_2O_6$ with the space group $P12_1/c1$ (JCPDS 01-072-2088).[29] SEM and TEM images of $SrNb_2O_6$ are shown in Figure 1b and 1c, respectively, which indicate that the produced $SrNb_2O_6$ mainly consists of a nanorod structure. The corresponding high-resolution TEM image in Figure 1d shows fringe spacings of 0.395 and 0.542 nm, which correspond to the (012) and (002) lattice planes of monoclinic $SrNb_2O_6$, respectively. These results indicate that the $SrNb_2O_6$ nanorods are of good crystallinity with a growth direction parallel to the lattice (012) plane.

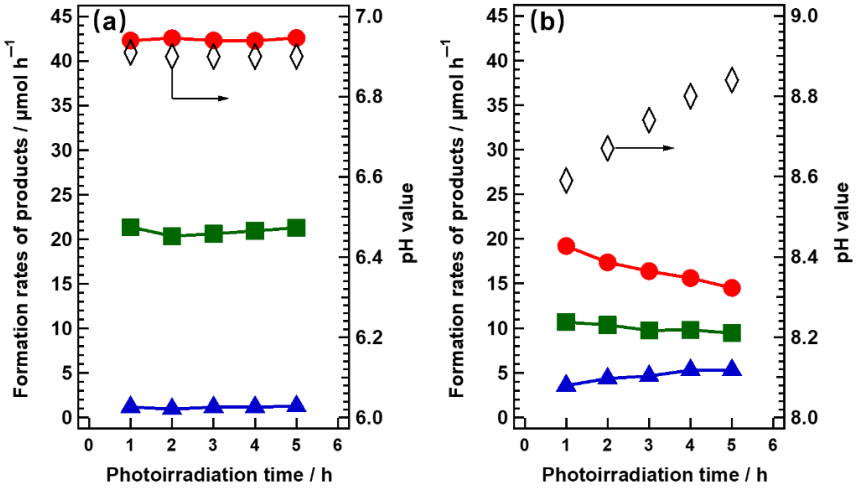

Figure 2 Formation rates of H_2 (blue triangles), O_2 (green squares), and CO (red circles), and pH values of the solution (open diamond) for the photocatalytic conversion of CO_2 in an $NaHCO_3$ aqueous solution over $Ag/SrNb_2O_6$ with the bubbling of (a) CO_2 and (b) Ar gas. Photocatalyst: 1.0 wt.% $Ag/SrNb_2O_6$ (0.5 g), reaction solution volume: H_2O (1.0 L), gas flow rate: 30 mL min^{-1}, light source: 400 W high-pressure Hg lamp.

Figure 2a shows the formation rates of H_2, O_2, and CO during the photocatalytic conversion of CO_2 for 5 h with the bubbling of CO_2 in the $NaHCO_3$ solution. The formation rate of CO is about 42.3 μmol h^{-1} and is very stable during the photoirradiation for 5 h. A very small amount of H_2 is formed, and the selectivity toward CO evolution is higher than 97.3%. The pH value of the reaction solution is stable at 6.86 during the photocatalytic conversion of CO_2 for 5 h while continuously bubbling CO_2. However, when flowing Ar gas instead of CO_2 gas, as shown in Figure 2b, the formation rate of CO

decreases by approximately half to 19.2 μmol h^{-1}, and the formation rate of H_2 increases slightly after 1 h of photoirradiation. With the increase in photoirradiation time, the pH value of the solution increases from 8.58 to 8.89, and the formation rate of CO decreases while H_2 increases after photoirradiation for 5 h under the flowing of Ar.

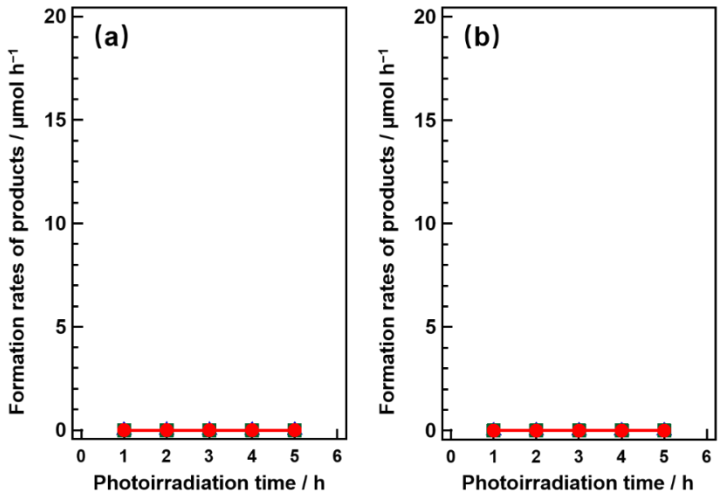

Figure 3 Formation rates of H_2 (blue triangles), O_2 (green squares), and CO (red circles) for the photocatalytic conversion of CO_2 in an $NaHCO_3$ aqueous solution over $Ag/SrNb_2O_6$ with the bubbling of Ar gas. (a) dark condition; (b) no photocatalyst. Photocatalyst: 1.0 wt.% $Ag/SrNb_2O_6$ (0.5 g), reaction solution volume: H_2O (1.0 L), Ar gas flow rate: 30 mL min^{-1}, light source: 400 W high-pressure Hg lamp.

Various control experiments were investigated to confirm the CO_2 source under the flowing of Ar. No products were detected in the dark (Figure 3a) and without a photocatalyst (Figure 3b). Table 1 lists the formation rates of products for the photocatalytic conversion of CO_2 over $Ag/SrNb_2O_6$ with different additives under the bubbling of Ar. H_2 and O_2 are observed as the main products, while the formation rate of CO is negligible without any additives (Entry 1). This result indicates that additives are indispensable for the photocatalytic conversion of CO_2 over $Ag/SrNb_2O_6$ in an aqueous solution. A high selectivity toward CO evolution is obtained in the case of $NaHCO_3$, $KHCO_3$, and NH_4HCO_3 as additives (Entry 2–4). Notably, a very high formation rate of CO and selectivity toward CO evolution are achieved with NH_4HCO_3 as an additive under the bubbling of Ar gas instead of CO_2 gas (287 μmol h^{-1} and 94.2%, respectively). A stoichiometric amount of N_2 is obtained as the oxidation product,

indicating that ammonia and/or ammonium ions function as electron donors in the photocatalytic conversion of CO_2 into CO, which have been reported in our previous work.[30, 31] A very small amount of CO is evolved when using other additives, such as Na_2CO_3, NaOH, and a mixed solution of Na_2HPO_4/NaH_2PO_4, which show similar pH values as in the $NaHCO_3$ solution (Entry 5–7). If CO_2 is bubbled into 0.05 M of Na_2CO_3 until the pH of the reaction solution at 8.51 is close to that of the $NaHCO_3$ solution at 8.59 and then changes to Ar gas, comparable amounts of CO, H_2, and O_2 will be obtained as compared to those in the case of $NaHCO_3$ for the photocatalytic conversion of CO_2 under the bubbling of Ar. According to the carbon equilibrium, after bubbling CO_2 into 0.05 M of Na_2CO_3 until the pH value reaches 8.51, the final solution will be similar to 0.1 M of $NaHCO_3$; therefore, the major species of dissolved CO_2 is HCO_3^-.[32] This result indicates that HCO_3^- acts as the carbon source for the photocatalytic conversion of CO_2 into CO in the aqueous solution containing bicarbonate ions under the bubbling of Ar.

Table 1 Photocatalytic conversion of CO_2 over $Ag/SrNb_2O_6$ with different additives under the bubbling of Ar gas.

Entry	Additives	pH	Formation rates of gases / μmol h^{-1}			Selec. toward CO (%)
			H_2	O_2	CO	
1	None	6.90	2.9	1.2	0.1	3.3
2	[a]$NaHCO_3$	8.59	3.6	10.7	19.2	87.8
3	[a]$KHCO_3$	8.56	2.2	11.2	20.6	90.3
4	[a]NH_4HCO_3	8.28	17.9	94.2 (N_2)	287	94.1
5	[b]Na_2CO_3	11.21	14.9	7.7	0.1	0.7
6	[a]NaOH	12.89	17.7	8.2	0.3	1.5
7	Na_2HPO_4/NaH_2PO_4	8.30	18.3	9.1	0.1	0.5
8	[c]$Na_2CO_3 + CO_2$	8.51	2.0	13.1	26.3	93.0

Photocatalyst: 1.0 wt.% $Ag/SrNb_2O_6$ (0.5 g), reaction solution volume: H_2O (1.0 L), Ar flow rate: 30 mL min^{-1}, light source: 400 W high-pressure Hg lamp; concentrations of additives: [a] 0.1 M; [b] 0.05 M, [c] CO_2 was bubbled into 0.05 M of Na_2CO_3 aqueous solution until the pH of the reaction solution reached 8.51, and then the CO_2 gas was changed to Ar gas.

HCO_3^- is converted into H_2CO_3(aq) because there are no CO_2-related species in the aqueous solution. H_2CO_3(aq) will further produce CO_2(aq) easily because of the low hydration equilibrium constant of carbonic acid in pure water.[23] Based on the carbon equilibrium in the solution, there are primarily four equilibria in the solution:

$$HCO_3^- (aq) \rightleftharpoons H_2CO_3 (aq) + OH^- (aq) \quad (3)$$

$$H_2CO_3 (aq) \rightleftharpoons CO_2 (aq) + H_2O (l) \quad (4)$$

$$CO_2 (aq) \rightleftharpoons CO_2 (g) \quad (5)$$

$$HCO_3^- (aq) + OH^- (aq) \rightleftharpoons CO_3^{2-} (aq) \quad (6)$$

Based on Eqn. (3) and (6), the first and second dissociation constants of carbonic acid can be denoted by the following equations, respectively:

$$K_1 = \frac{[OH^-][H_2CO_3]}{[HCO_3^-]} = \frac{K_w[H_2CO_3]}{[H^+][HCO_3^-]} \quad (7)$$

$$K_2 = \frac{[CO_3^{2-}]}{[HCO_3^-][OH^-]} = \frac{[H^+][CO_3^{2-}]}{K_w[HCO_3^-]} \quad (8)$$

where $K_w = 1.0\times10^{-14}$ is the self-ionization constant of water:

$$K_w = [H^+][OH^-] \quad (9)$$

As mentioned in our previous paper, because the CO_2 hydration equilibrium constant is very small, the $[H_2CO_3]$ mentioned in Eqn. (3) and (4) is almost equal to $[CO_2(aq)]$,[23] and $K_1' = K_w / K_1$, $K_2' = K_2 \times K_w$. Thus, Eqn. (7) and (8) can be changed to

$$K_1' = \frac{[H^+][HCO_3^-]}{[CO_2(aq)]} \quad (10)$$

$$K_2' = \frac{[H^+][CO_3^{2-}]}{[HCO_3^-]} \quad (11)$$

In the $NaHCO_3$ aqueous solution, there are primarily three kinds of CO_2-related species: CO_2(aq), HCO_3^-, and CO_3^{2-}. Herein, I define D as the total concentration of all CO_2-related species:

$$D = [CO_2(aq)] + [HCO_3^-] + [CO_3^{2-}] \quad (12)$$

Substituting Eqn. (10) and (11) into (12) results in

$$[\mathrm{HCO_3^-}] = \frac{K_1'[\mathrm{H^+}]}{[\mathrm{H^+}]^2+K_1'[\mathrm{H^+}]+K_1'K_2'} \cdot D \tag{13}$$

$$[\mathrm{CO_3^{2-}}] = \frac{K_1'K_2'}{[\mathrm{H^+}]^2+K_1'[\mathrm{H^+}]+K_1'K_2'} \cdot D \tag{14}$$

$$[\mathrm{CO_2(aq)}] = \frac{[\mathrm{H^+}]^2}{[\mathrm{H^+}]^2+K_1'[\mathrm{H^+}]+K_1'K_2'} \cdot D \tag{15}$$

In contrast, according to the ionization balance of ions in the $NaHCO_3$ solution, which exhibits electrical neutrality,

$$[\mathrm{Na^+}] + [\mathrm{H^+}] = [\mathrm{HCO_3^-}] + 2[\mathrm{CO_3^{2-}}] + [\mathrm{OH^-}] \tag{16}$$

When Eqn. (13), (14), and (15) are introduced into (16), the value of *D* can be obtained as

$$D = \left([\mathrm{Na^+}] + [\mathrm{H^+}] - \frac{K_w}{[\mathrm{H^+}]}\right)\left(\frac{[\mathrm{H^+}]^2+K_1'[\mathrm{H^+}]+K_1'K_2'}{K_1'[\mathrm{H^+}]+2K_1'K_2'}\right) \tag{17}$$

Plummer and Busenberg[33] reported that the dissociation constants of carbonic acid, K_1' and K_2', can be calculated from the temperature of the solution; the empirical expression is as follows:

$$log\, K_1' = -356.3094 - 0.06091964T + \frac{21834.37}{T} + 126.8339\, log\, T - \frac{1684915}{T^2} \tag{18}$$

$$log\, K_2' = -107.8871 - 0.03252849T + \frac{5151.79}{T} + 38.92561\, log\, T - \frac{563713.9}{T^2} \tag{19}$$

where *T* is the temperature of the solution.

Therefore, the concentrations of all the CO_2-related species (CO_2(aq), HCO_3^-, and CO_3^{2-}) in a carbonic acid buffer aqueous solution can be estimated by the temperature and pH of the solution. In this work, the measured pH values ranged from 4.0 to 12.0 during the photocatalytic conversion of CO_2. Figure 4 presents the calculated concentrations of CO_2(aq), HCO_3^-, and CO_3^{2-} in a 0.10 M aqueous solution of $NaHCO_3$ at 303 K under 101.325 kPa of CO_2. During the photocatalytic conversion of CO_2 in a $NaHCO_3$ aqueous solution with the bubbling of Ar gas, the pH values of the solutions are about 8.0–9.0. In this pH range, $[HCO_3^-]$ is almost stable at 0.10 M; $[CO_2(aq)]$ is quite low, ranging from 2.11×10^{-3} to 1.93×10^{-4} M; and $[CO_3^{2-}]$ ranges from 5.09×10^{-4} to 4.66×10^{-3} M.

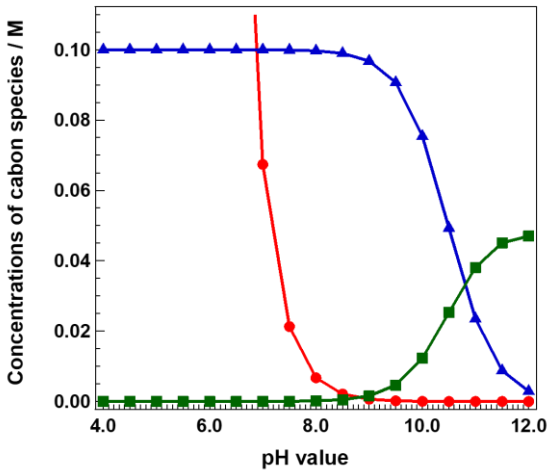

Figure 4 Calculated concentrations of CO_2 (aq) (circles), HCO_3^- (triangles), and CO_3^{2-} (squares) in 0.10 M aqueous solution of $NaHCO_3$ at 303 K under 101.325 kPa of CO_2.

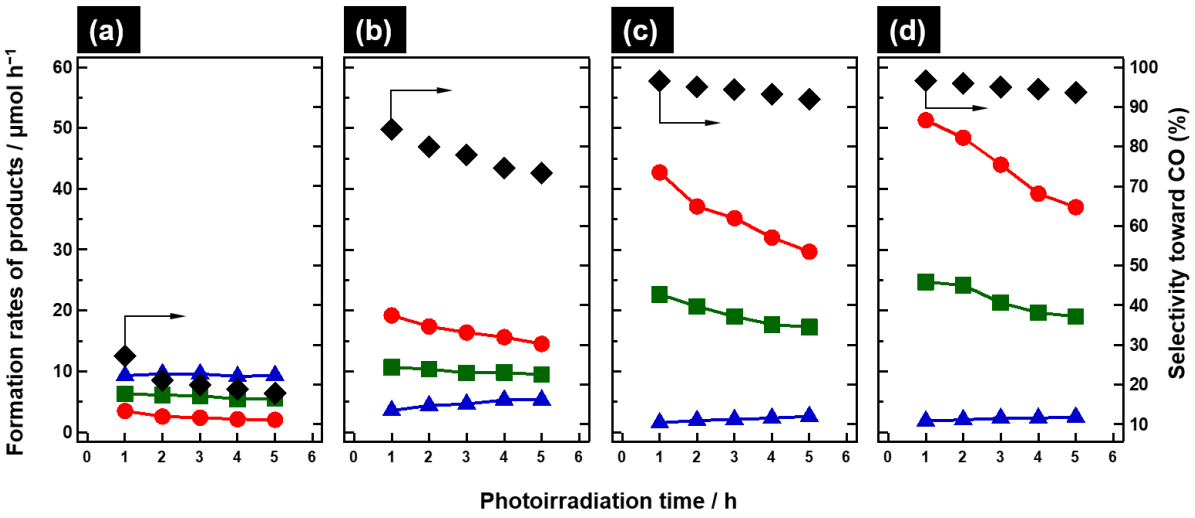

Figure 5 Formation rates of H_2 (blue triangles), O_2 (green squares), and CO (red circles), and selectivity toward CO evolution (black diamond) at different concentrations of $NaHCO_3$: (a) 0.01, (b) 0.10, (c) 0.30, and (d) 0.50 M for the photocatalytic conversion of CO_2 after photoirradiation for 5 h. Photocatalyst: 1.0 wt.% $Ag/SrNb_2O_6$ (0.5 g), reaction solution volume: H_2O (1.0 L), Ar flow rate: 30 mL min^{-1}, light source: 400 W high-pressure Hg lamp.

In the previous work, CO_2(aq) was proved to be the direct reactant for the photocatalytic conversion of CO_2 with H_2O as an electron donor over $Ag/ZnGa_2O_4/Ga_2O_3$ with the continuous

bubbling of CO_2.[23] If Ar was bubbled instead of CO_2, H_2 would become the main product and the CO evolved would be negligible because of the low [CO_2(aq)]. On the contrary, the selectivity toward CO evolution was still very high in this work even though [CO_2(aq)] was very low. In order to confirm which species was the actual reactant during the photocatalytic conversion of CO_2 under the flowing of Ar in the aqueous solution of bicarbonate salt, I investigated the effect of the $NaHCO_3$ concentration ([$NaHCO_3$]) and the dependences of the formation rate of CO on [CO_2(aq)], [HCO_3^-], and [CO_3^{2-}].

Figure 5 shows the formation rates of H_2, O_2, and CO at different [$NaHCO_3$] for the photocatalytic conversion of CO_2 after photoirradiation for 5 h. When [$NaHCO_3$] is 0.01 M, the formation rate of CO is lower than that of H_2. The formation rate of CO and selectivity toward CO evolution steadily increases with [$NaHCO_3$] from 0.01 to 0.50 M. The formation rate of CO reaches 51.2 μmol h^{-1} with a selectivity toward CO evolution of higher than 96.5% after photoirradiation for 1 h in 0.50 M of $NaHCO_3$ solution. It should be noted that the formation rate of H_2 decreases with [$NaHCO_3$], as shown in Figure 6 This result indicates that increasing the concentration of HCO_3^- is beneficial for improving the formation rate of CO and suppressing the formation of H_2. As shown in Figure 7, the pH values of the reaction solutions increase with the photoirradiation time because the production of CO promotes the decomposition of HCO_3^- into H_2CO_3 and OH^- according to Eqn. (3) and (4).

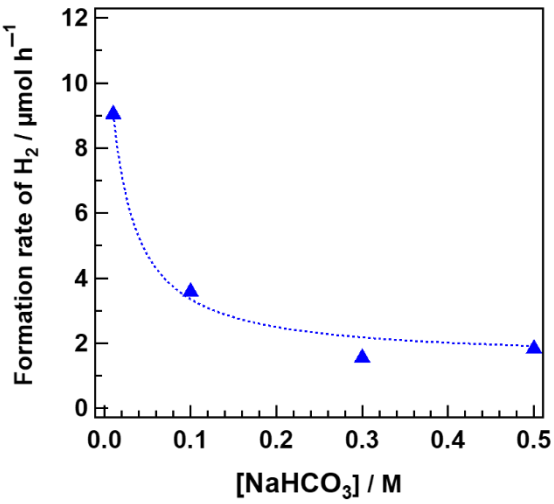

Figure 6 Formation rates of H_2 at different concentrations of $NaHCO_3$ for the photocatalytic conversion of CO_2 after photoirradiation for 1 h. Photocatalyst: 1.0 wt.% $Ag/SrNb_2O_6$ (0.5 g), reaction solution volume: H_2O (1.0 L), Ar flow rate: 30 mL min^{-1}, light source: 400 W high-pressure Hg lamp.

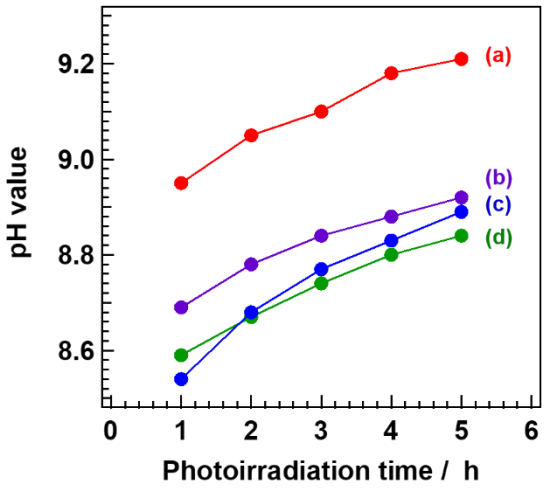

Figure 7 The pH of the reaction solutions during the photocatalytic conversion of CO_2 for 5 h in different [$NaHCO_3$] solutions: (a) 0.01 M, (b) 0.10 M, (c) 0.30 M, and (d) 0.50 M.

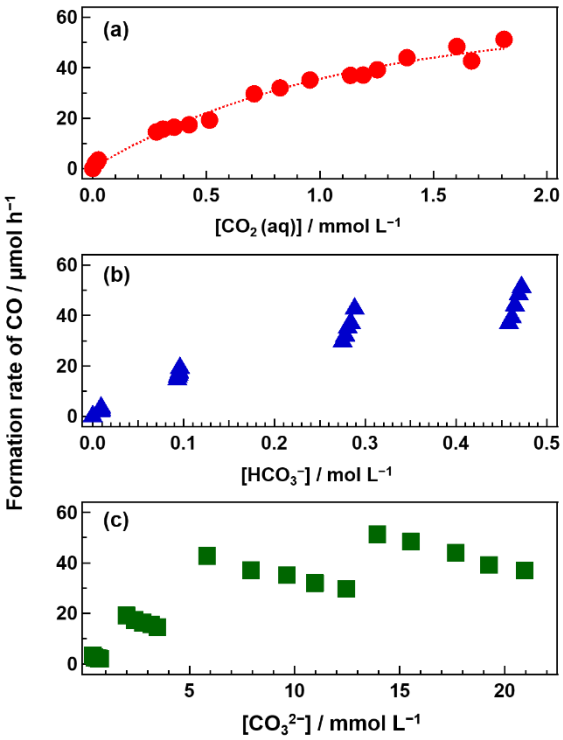

Figure 8 Dependences of the formation rate of CO on [CO_2(aq)] (circles), [HCO_3^-] (triangles), and [CO_3^{2-}] (squares) at different [$NaHCO_3$] ([$NaHCO_3$] = 0.01, 0.10, 0.30, and 0.50 M).

Based on the pH values and reaction temperatures of different [$NaHCO_3$] solutions, I calculated the corresponding concentrations of carbon species (CO_2(aq), HCO_3^-, and CO_3^{2-}) derived from Eqn.

(13), (14), and (15) according to Eqn. (17), (18), and (19). Figure 8 displays the dependences of the formation rate of CO on [CO_2(aq)], [HCO_3^-], and [CO_3^{2-}]. In a fixed concentration of $NaHCO_3$ solution, the formation rate of CO increases with [CO_2(aq)] and [HCO_3^-], while it decreases with [CO_3^{2-}]. As [$NaHCO_3$] increases from 0.01 to 0.50 M, [CO_2(aq)], [HCO_3^-] and [CO_3^{2-}] increase steadily. However, in the whole [$NaHCO_3$] range, the formation rate of CO only shows a good correspondence with [CO_2(aq)]. This result clearly indicates that the CO_2(aq) obtained by the dissociation of HCO_3^- is the actual reactant for the photocatalytic conversion of CO_2, although [CO_2(aq)] is very low at solution pH values ranging from 8.0 to 9.0. Consequently, the yield of CO is defined as

$$Y = \frac{R_{CO}}{[CO_2(aq)]} \tag{20}$$

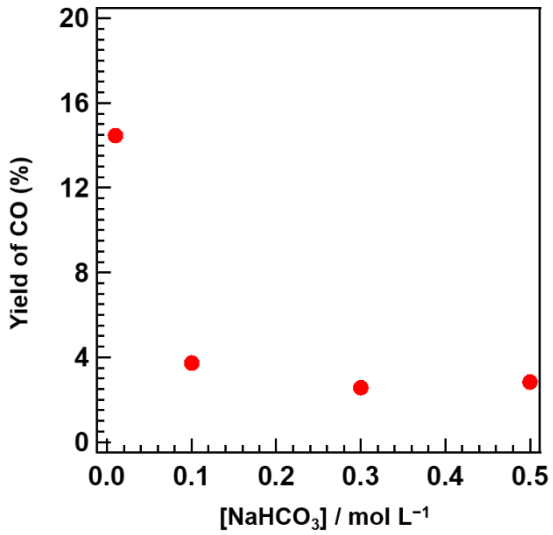

Figure 9 Yield of CO for the photocatalytic conversion of CO_2 with Ar gas bubbling at different [$NaHCO_3$].

Figure 2a has showed that the formation rate of CO is about 42.3 μmol h^{-1} with the pH value of the reaction solution stable at 6.86 when CO_2 gas is continuously bubbled into 0.10 M of $NaHCO_3$ solution. The yield of CO is only about 0.15% in this case. Figure 9 shows the yield of CO for the photocatalytic conversion of CO_2 with Ar gas bubbling at different [$NaHCO_3$]. The yield of CO is about 3.0% when [$NaHCO_3$] ranges from 0.10 to 0.50 M, and reaches about 14.6% when [$NaHCO_3$] is 0.01 M, although H_2 is the main product in this case. This work suggests that using bicarbonate as a

carbon source can greatly increase the conversion rate of CO_2, and Ag/SNb_2O_6 is a promising photocatalyst for the highly effective conversion of CO_2 into CO at low CO_2 concentrations.

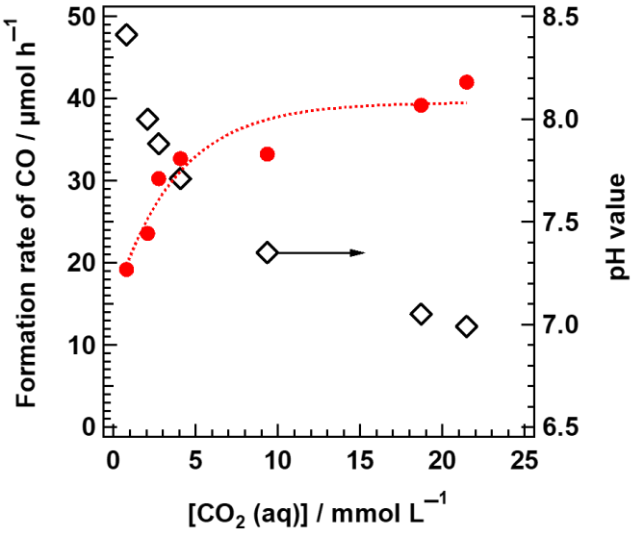

Figure 10 Dependence of formation rate of CO (red circles) and pH values (open diamonds) on $[CO_2(aq)]$ at different partial pressures of CO_2. The partial pressure of CO_2 was adjusted by varying the flow rate of CO_2 and Ar in the gas phase of the fluid (flow rate ratio of CO_2:Ar = 0:30, 2:28, 3:27, 5:25, 10:20, 20:10, and 30:0), the total flow rate of CO_2 and Ar gas was 30 mL min, $[NaHCO_3]$ = 0.1 M, and T = 304.5 K.

I further investigated the dependence of the formation rate of CO on $[CO_2(aq)]$ by varying the partial pressure of CO_2 in the gas phase. A change in the partial pressure of CO_2 will result in a change in the pH of the solution. According to Eqn. (15), (17), (18), and (19), $[CO_2(aq)]$ can be calculated with different partial pressures of CO_2. Figure 10 illustrates the dependence of the formation rate of CO on $[CO_2(aq)]$ at different partial pressures of CO_2. With the increase in the partial pressure of CO_2, the pH of the solution gradually decreases, and the formation rate of CO increases exponentially with $[CO_2(aq)]$ in the reaction solution, which is consistent with the result in Figure 5. This result further confirms that $CO_2(aq)$ is the direct reactant for the photocatalytic conversion of CO_2 in the aqueous solution containing bicarbonate ions. Note that the formation rate of CO at low $[CO_2(aq)]$ is almost half that at high $[CO_2(aq)]$, indicating that $Ag/SrNb_2O_6$ acts as an active photocatalyst for the reduction of CO_2 even at low concentrations of CO_2 molecules dissolved in an aqueous solution as a real intermediate species. It already reported that the formation rate of CO dramatically decreases over

$Ag/ZnGa_2O_4/Ga_2O_3$ at low [CO_2(aq)].[16, 17] It is expected that $Ag/SrNb_2O_6$ can make CO_2(aq) easily adsorb on the surface and condense near the active sites.

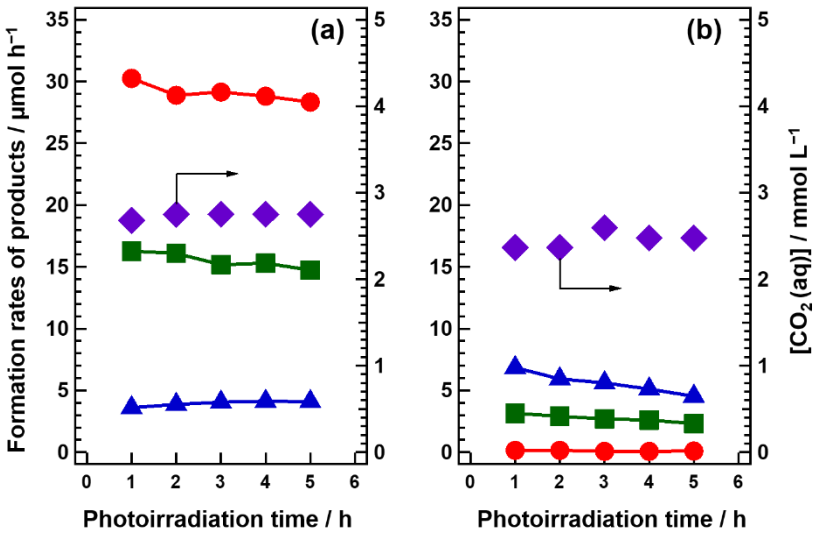

Figure 11 Formation rates of CO (red circles), H_2 (blue triangles), O_2 (green squares), and [CO_2(aq)] (purple diamonds) for the photocatalytic conversion of CO_2 in (a) an aqueous solution of $NaHCO_3$ and (b) pure H_2O solution. Photocatalyst: 1.0 wt.% $Ag/SrNb_2O_6$ (0.5 g), reaction solution volume: H_2O (1.0 L), gas flow rate: 30 mL min^{-1}, light source: 400 W high-pressure Hg lamp.

Figures 11a and 11b shows the formation rates of H_2, O_2, and CO for the photocatalytic conversion of CO_2 in an aqueous solution of $NaHCO_3$ and in a pure H_2O solution, respectively. Because CO_2(aq) is considered to be the reactant for the photocatalytic conversion of CO_2 into CO, the partial pressure of CO_2 was adjusted to keep [CO_2(aq)] similar in two solutions. Almost no CO is evolved in the H_2O solution, while the formation rate of CO is as high as 30.2 μmol h^{-1} with a selectivity higher than 89% in the $NaHCO_3$ solution. This result indicates that HCO_3^- has a great influence on the photocatalytic activity and selectivity for the conversion of CO_2, although it is not the direct reactant for the photocatalytic conversion of CO_2.

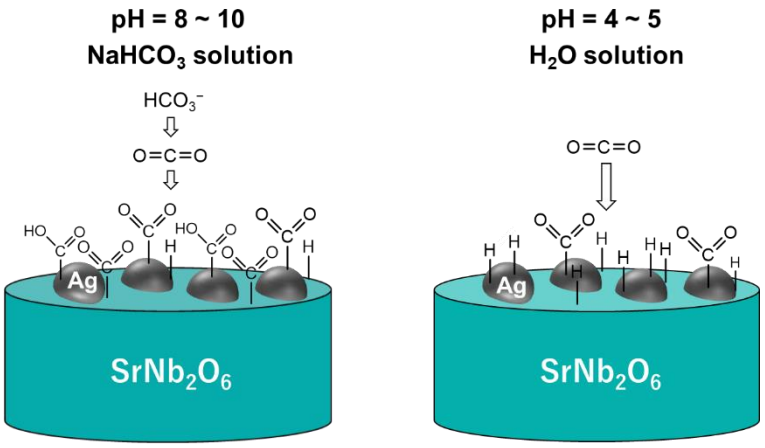

Scheme 1 Adsorbed species on the surface of photocatalyst during the photocatalytic conversion of CO_2 in $NaHCO_3$ solution with the bubbling of Ar and in pure H_2O solution with the bubbling of CO_2.

Regarding the role of HCO_3^-, I think there are two possibilities: (1) As shown in Scheme 1, the primary adsorbed species on the photocatalyst is carbonate or a bicarbonate species derived from HCO_3^-, with the pH ranging from 8.0 to 9.0 in an aqueous solution of $NaHCO_3$ with the flowing of Ar gas. However, hydrogen species are mainly adsorbed on the photocatalyst surface in the pure H_2O solution with the bubbling of CO_2 because of the low pH value. The high concentration of carbon-related species on the surface of the photocatalyst will help suppress the formation of H_2 and promote the formation of CO during the photocatalytic conversion of CO_2. This indicates that HCO_3^- functions as a buffer for supplying CO_2 on the surface of $Ag/SrNb_2O_6$, and adjusts the pH of the reaction solution to suppress the photocatalytic conversion of H^+ into H_2 and promote the photocatalytic conversion of CO_2 into CO; (2) from Figure 7b and Entry 1 in Table 1, it can observe that the formation rate of H_2 is quite low in the pure H_2O solution. However, the formation rate of H_2 significantly improves by adding some additives such as NaOH, Na_2CO_3, or Na_2HPO_4/NaH_2PO_4 mixture (Entry 5–7 in Table 1). Some papers have reported that alkaline hydroxides or carbonates can inhibit the backward reaction for the photocatalytic splitting of water.[34-38] Arakawa et al.[39, 40] reported that HCO_3^- can be activated by the photogenerated holes in the water splitting reaction and form peroxycarbonate, which easily decomposes into O_2 and CO_2 via holes under the photoirradiation. They thought that the presence of HCO_3^- easily desorbed the generated O_2 from the photocatalyst surface, suppressing the backward reaction for water splitting ($H_2 + O_2 \rightarrow H_2O$). Herein, I consider that the HCO_3^- species has a similar

effect on the photocatalytic conversion of CO_2: the rapid desorption of O_2 from the photocatalyst surface is beneficial for inhibiting the backward reaction for the photocatalytic conversion of CO_2 ($CO + O_2 \rightarrow CO_2$). Although, in the present study, I unfortunately did not find an effective measure to prove the existence of peroxycarbonate in this system. Based on the above two possibilities, I suggest that the presence of HCO_3^- can greatly improve the photocatalytic activity and selectivity toward CO evolution for the conversion of CO_2 in the aqueous solutions containing bicarbonate ions.

Conclusions

In this work, I proposed a strategy by using bicarbonate as the carbon source for the photocatalytic conversion of CO_2 over $Ag/SrNb_2O_6$. The selectivity toward CO evolution was higher than 87% for the photocatalytic conversion of CO_2 with various bicarbonate salts as additives. Notably, the formation rate of CO was as high as 287 μmol h^{-1} with a selectivity toward CO evolution of higher than 94.1% when NH_4HCO_3 was used as an additive under the bubbling of Ar instead of CO_2. The formation rate of CO showed a good correspondence with [CO_2(aq)], indicating that the CO_2(aq) obtained by the dissociation of HCO_3^- was the actual reactant for the photocatalytic conversion of CO_2. The following possible roles of HCO_3^- were also proposed: (1) It functions as a buffer for supplying CO_2 on the surface of $Ag/SrNb_2O_6$, which increases the concentrations of carbon-related species on the photocatalyst surface; (2) it inhibits the backward reaction for the photocatalytic conversion of CO_2 by accelerating the desorption of O_2 from the $Ag/SrNb_2O_6$ surface. In conclusion, the presence of HCO_3^- can greatly enhance the photocatalytic activity and selectivity toward CO evolution for the conversion of CO_2 in aqueous solutions. By using bicarbonate as a carbon source for the photocatalytic conversion of CO_2 over $Ag/SrNb_2O_6$, the photocatalytic efficiency and utilization of CO_2 significantly improve. I believe this study will provide meaningful insight into the practical application of the photocatalytic conversion of CO_2 to other feedstocks.

References

1. R. K. Pachauri, M. R. Allen, V. R. Barros, J. Broome, W. Cramer, R. Christ, J. A. Church, L.

Clarke, Q. Dahe and P. Dasgupta, *Climate change 2014: synthesis report. Contribution of Working Groups I, II and III to the fifth assessment report of the Intergovernmental Panel on Climate Change*, IPCC, 2014.

2. K. Teramura and T. Tanaka, *Phys. Chem. Chem. Phys.*, 2018, **20**, 8423-8431.
3. J. L. White, M. F. Baruch, J. E. Pander Iii, Y. Hu, I. C. Fortmeyer, J. E. Park, T. Zhang, K. Liao, J. Gu, Y. Yan, T. W. Shaw, E. Abelev and A. B. Bocarsly, *Chem. Rev.*, 2015, **115**, 12888-12935.
4. C. Chen, W. Ma and J. Zhao, *Chem. Soc. Rev.*, 2010, **39**, 4206-4219.
5. M. Cokoja, C. Bruckmeier, B. Rieger, W. A. Herrmann and F. E. Kuehn, *Angew. Chem. Int. Ed.*, 2011, **50**, 8510-8537.
6. M. Halmann, *Nature*, 1978, **275**, 115-116.
7. T. Inoue, A. Fujishima, S. Konishi and K. Honda, *Nature*, 1979, **277**, 637-638.
8. R. B. Anderson, H. Kölbel and M. Ralek, *The fischer-tropsch synthesis*, Academic Press New York, 1984.
9. G. Henrici-Olivé and S. Olive, *Angew. Chem. Int. Ed.*, 1976, **15**, 136-141.
10. G. Centi, E. A. Quadrelli and S. Perathoner, *Energy Environ. Sci.*, 2013, **6**, 1711-1731.
11. K. Iizuka, T. Wato, Y. Miseki, K. Saito and A. Kudo, *J. Am. Chem. Soc.*, 2011, **133**, 20863-20868.
12. T. Takayama, A. Iwase and A. Kudo, *Bull. Chem. Soc. Jpn.*, 2015, **88**, 538-543.
13. H. Nakanishi, K. Iizuka, T. Takayama, A. Iwase and A. Kudo, *ChemSusChem*, 2017, **10**, 112-118.
14. H. Yoshida, L. Zhang, M. Sato, T. Morikawa, T. Kajino, T. Sekito, S. Matsumoto and H. Hirata, *Catal. Today*, 2015, **251**, 132-139.
15. A. Anzai, N. Fukuo, A. Yamamoto and H. Yoshida, *Catal. Commun.*, 2017, **100**, 134-138.
16. Z. Wang, K. Teramura, Z. Huang, S. Hosokawa, Y. Sakata and T. Tanaka, *Catal. Sci. Technol.*, 2016, **6**, 1025-1032.
17. K. Teramura, Z. Wang, S. Hosokawa, Y. Sakata and T. Tanaka, *Chem. – Eur. J.*, 2014, **20**, 9906-9909.
18. Z. Wang, K. Teramura, S. Hosokawa and T. Tanaka, *J. Mater. Chem. A*, 2015, **3**, 11313-11319.
19. Z. Huang, K. Teramura, S. Hosokawa and T. Tanaka, *Appl. Catal. B*, 2016, **199**, 272-281.
20. H. Tatsumi, K. Teramura, Z. Huang, Z. Wang, H. Asakura, S. Hosokawa and T. Tanaka, *Langmuir*,

2017, **33**, 13929-13935.

21. Z. Huang, K. Teramura, H. Asakura, S. Hosokawa and T. Tanaka, *Catal. Today*, 2018, **300**, 173-182.
22. R. Pang, K. Teramura, H. Tatsumi, H. Asakura, S. Hosokawa and T. Tanaka, *Chem. Commun.*, 2018, **54**, 1053-1056.
23. K. Teramura, K. Hori, Y. Terao, Z. Huang, S. Iguchi, Z. Wang, H. Asakura, S. Hosokawa and T. Tanaka, *J. Phys. Chem. C*, 2017, **121**, 8711-8721.
24. K. Teramura, H. Tatsumi, Z. Wang, S. Hosokawa and T. Tanaka, *Bull. Chem. Soc. Jpn.*, 2015, **88**, 431-437.
25. Z. Wang, K. Teramura, S. Hosokawa and T. Tanaka, *Appl. Catal. B*, 2015, **163**, 241-247.
26. D. A. Palmer and R. Van Eldik, *Chem. Rev.*, 1983, **83**, 651-731.
27. K. Hara, A. Kudo, T. Sakata and M. Watanabe, *J. Electrochem. Soc.*, 1995, **142**, L57-L59.
28. R. Pang, K. Teramura, H. Asakura, S. Hosokawa and T. Tanaka, *Appl. Catal. B*, 2017, **218**, 770-778.
29. D. Chen and J. Ye, *Chem. Mater.*, 2009, **21**, 2327-2333.
30. Z. Huang, K. Teramura, H. Asakura, S. Hosokawa and T. Tanaka, *Chem. Sci.*, 2017, **8**, 5797-5801.
31. Z. Huang, S. Yoshizawa, K. Teramura, H. Asakura, S. Hosokawa and T. Tanaka, *ACS Sustainable Chem. Eng.*, 2018.
32. H. Zhong, K. Fujii, Y. Nakano and F. Jin, *J. Phys. Chem. C*, 2014, **119**, 55-61.
33. L. N. Plummer and E. Busenberg, *Geochim. Cosmochim. Acta*, 1982, **46**, 1011-1040.
34. A. Kudo, K. Domen, K.-i. Maruya and T. Onishi, *Chem. Phys. Lett.*, 1987, **133**, 517-519.
35. J. Kim, D. W. Hwang, H. G. Kim, S. W. Bae, J. S. Lee, W. Li and S. H. Oh, *Top. Catal.*, 2005, **35**, 295-303.
36. K. Sayama and H. Arakawa, *Chem. Lett.*, 1992, **21**, 253-256.
37. K. Sayama, R. Abe, H. Arakawa and H. Sugihara, *Catal. Commun.*, 2006, **7**, 96-99.
38. K. Sayama and H. Arakawa, *J. Chem. Soc., Faraday Trans.*, 1997, **93**, 1647-1654.
39. K. Sayama and H. Arakawa, *J. Photochem. Photobiol., A*, 1996, **94**, 67-76.
40. H. Arakawa and K. Sayama, *Catal. Surv. Jpn.*, 2000, **4**, 75-80.

Chapter 3

Modification of Ga_2O_3 by Ag-Cr core-shell co-catalyst enhances photocatalytic CO evolution for the conversion of CO_2 by H_2O

Abstract

A core-shell structure of Ag-Cr dual co-catalyst loaded-Ga_2O_3 was found to significantly enhance the formation rate of CO (480 μmol h^{-1}) and selectivity toward CO evolution (83.8%) for the photocatalytic conversion of CO_2, as compared to that of bare Ga_2O_3, Ag/Ga_2O_3, Cr/Ga_2O_3 and other Ag-metals/Ga_2O_3. An isotopic labeling experiment using $^{13}CO_2$ confirmed that the CO evolution originated from the CO_2 introduced in the gas phase rather than residual carbon contaminants. During the reaction, stoichiometric amounts of CO, H_2, and O_2 were obtained, which indicates that H_2O functions as an electron donor for the photocatalytic conversion of CO_2. The modification of Ga_2O_3 by Cr species provided a thin layer of Cr_2O_3 on the surface of the Ag co-catalyst, which drastically suppressed the formation of CO_2 from the produced CO and O_2. This is referred to as the backward reaction for the photocatalytic conversion of CO_2.

Introduction

The conversion of CO_2 as a fuel feedstock into other valuable chemical compounds, e.g., CO, HCOOH, HCHO, CH_3OH, and CH_4, under ambient temperature and pressure conditions has attracted significant attention as a renewable strategy for both environmental and energy issues.[1-5] The conversion of CO_2 into CO in particular has been widely studied as an alternative approach to generate syngas components.[6, 7] Nevertheless, the activation of CO_2 is extremely challenging owing to its high stability ($\Delta G_f^0 = -394.4$ kJ mol^{-1}).[8] It is especially difficult to selectively activate only CO_2 molecules in an aqueous solution in cases where H_2O is used as an electron donor, because the redox potential of H^+/H_2 (−0.41 V vs. NHE, at pH 7) is more positive than that of CO/CO_2 (−0.51 V vs. NHE, at pH 7).[9, 10] Thus, the reduction of protons (H^+) is preferred to that of CO_2.

Since the pioneering work by Halmann[11] and Inoue et al.,[12] significant efforts have been devoted to the semiconductor−based photocatalytic conversion of CO_2.[10, 13-17] However, most bare semiconductors without co-catalyst modifications exhibit very low photocatalytic activity for CO_2 conversion due to the facile recombination of electron-hole pairs before they migrate to the surface of the semiconductor.[18] Proper co-catalysts loaded onto light harvesting semiconductors can serve as both electron sinks and proton reduction sites, and can hence dramatically promote photocatalytic activity for the conversion of CO_2.[19, 20] Hori et al. reported that metal electrodes (Au, Ag, Cu, Zn) showed high selectivity toward CO evolution for the electrochemical conversion of CO_2.[21] Kudo and coworkers were the first to report the photocatalytic conversion of CO_2 into CO by H_2O prior to the conversion of H^+ into H_2 over Ag co-catalyst-loaded $BaLa_4Ti_4O_{15}$, whereas in the absence of an Ag co-catalyst, water splitting was predominant.[22] Since then, various co-catalysts have been investigated for the photocatalytic conversion of CO_2 in an aqueous solution. At present, Ag is considered to be the most effective co-catalyst toward CO evolution for the photocatalytic conversion of CO_2 using H_2O as an electron donor.[23-30]

Recently, some dual co-catalysts, such as Au-Cu and Ni-NiO, with proper structures have been designed to facilitate high CO_2 conversion activity by taking advantage of the synergistic effect between the two co-catalysts.[31-33] However, the formation rates of products for the photocatalytic conversion of CO_2 are still very low, and only a very few papers in the literature have confirmed that

carbon-containing products are derived from the CO_2 introduced in the gas phase rather than from residual organic contaminants where H_2O is an electron donor. Herein, I present a facile strategy for designing and preparing a core-shell structure of an Ag-Cr dual co-catalyst that significantly improves the photocatalytic efficiency for conversion of CO_2 into CO with H_2O as an electron donor.

Experimental

Preparation of Ag-Cr/Ga_2O_3

Ag-Cr/Ga_2O_3 was prepared by a facile simultaneously photodeposition method.[34, 35] Generally, 1.0 g of Ga_2O_3 (Kojundo, 99.99%) powder was dispersed in 1.0 L of ultra-pure water containing a required amount of $AgNO_3$ and $Cr(NO_3)_3$, and the dissolved air in the solution was completely degassed by a flow of Ar gas. The suspension was irradiated under a 400 W high-pressure Hg lamp with Ar gas flowing for 1.0 h, followed by filtration and drying at room temperature. The amount of Ag and Cr was the molar ratio of Ag/Ga and Cr/Ga.

Characterization

The as-prepared Ag-Cr/Ga_2O_3 was studied by X-ray diffractometry (XRD, Rigaku Multiflex) with Cu Kα radiation (λ = 0.154 nm), field-emission scanning electron microscopy (FE-SEM, SU−8220, Hitachi High Technologies), transmission electron microscopy (TEM, JEM−2100F), X-ray photoelectron spectroscopy (XPS, Shimadzu, ESCA 3400, Mg Kα), and X-ray absorption fine structure (XAFS) at the Ag K-edge and Cr K-edge (beam line BL01B1 of Spring-8).

Photocatalytic reaction

The photocatalytic reduction of CO_2 was carried out using a flow system with an inner-irradiation-type reaction vessel at ambient pressure. First, the synthesized photocatalyst (0.5 g) was dispersed in ultrapure water (1.0 L) containing 0.1 M $NaHCO_3$. Second, CO_2 was bubbled into the solution at a flow rate of 30 mL min^{-1}. Third, the suspension was illuminated using a 400 W high-pressure mercury lamp with a quartz filter connected to a water cooling system. The amounts of evolved H_2 and O_2 were detected using a thermal conductivity detector-gas chromatography system (TCD-GC, Shimadzu Corp; MS−5A column, Ar carrier). The amount of evolved CO was analyzed by a flame ionization detector-GC with a methanizer (FID-GC, ShinCarbon ST column, N_2 carrier).

In the backward reaction, the processes were almost the same as those of the photocatalytic reduction of CO_2, except that the CO, O_2 and diluent gas Ar were bubbled into the ultrapure water solution with a total flow rate of 30 mL min^{-1}, and the amount of evolved CO_2 was analyzed by FID-GC.

Results and discussion

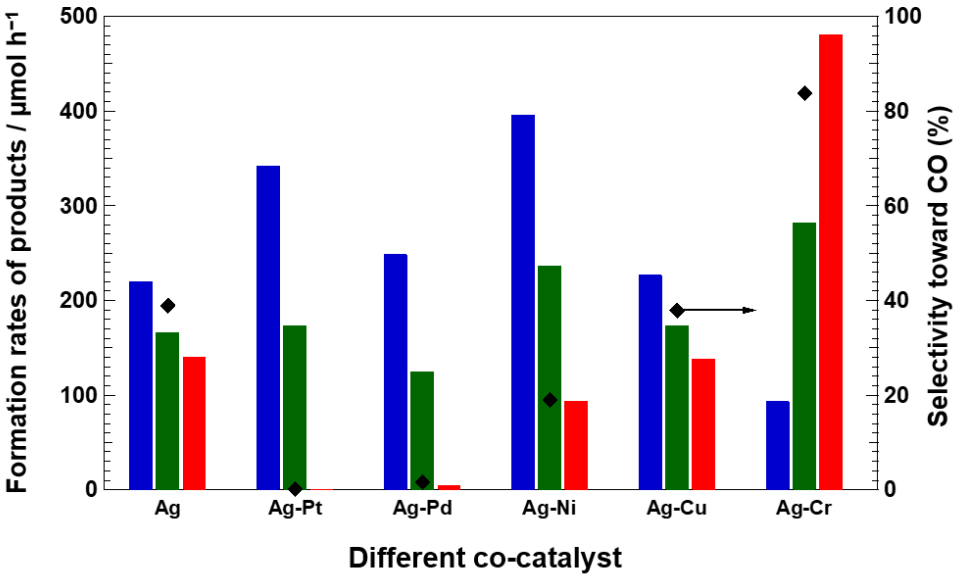

Figure 1 Formation rates of H_2 (blue), O_2 (green), CO (red), and selectivity toward CO (black diamonds) evolution for the photocatalytic conversion of CO_2 in water over Ag/Ga_2O_3 and Ag-metals/Ga_2O_3 photocatalysts. Photocatalyst powder: 0.5 g, reaction solution volume: 1.0 L, additive: 0.1 M $NaHCO_3$, Ag loading amount: 1.0 mol% (Ag/Ga), metals loading amount: 1.0 mol% (metals/Ga), modification method: simultaneously photodeposition (SPD) method, CO_2 flow rate: 30 mL min^{-1}, light source: 400 W high-pressure Hg lamp.

I preliminarily investigated the catalytic performances of different Ag-metal dual co-catalyst-loaded Ga_2O_3 for the photocatalytic conversion of CO_2 (Figure 1). Among these, Ag-Cr co-catalyst loaded-Ga_2O_3 (Ag-Cr/Ga_2O_3) exhibited the highest activity for the formation of CO and the highest selectivity toward CO evolution. Thus, the present work focuses on Ag-Cr/Ga_2O_3 and investigates the reasons for its excellent photocatalytic performance for the conversion of CO_2.

Table 1 shows the formation rates of H_2, O_2, and CO as products and their selectivity toward CO evolution for the photocatalytic conversion of CO_2 vs. bare Ga_2O_3, Ag/Ga_2O_3, Cr/Ga_2O_3, and $Ag\text{-}Cr/Ga_2O_3$. Compared with bare Ga_2O_3, the formation rate of CO increased after loading with the Ag co-catalyst, as Ag is well known to be effective for the conversion of CO_2 to CO in an aqueous solution; however, the selectivity toward CO evolution was still low. If only the Cr co-catalyst was loaded, the formation rates of all the products decreased, because Cr species on the Ga_2O_3 surface do not induce the migration of photogenerated electrons from the bulk to the surface of the catalyst.[36] Surprisingly, when Ag and Cr were simultaneously loaded, the result was a very high formation rate of CO (480 μmol h^{-1}) and high selectivity toward CO evolution (83.8%). The formation rate of CO and selectivity toward CO were 2.4 times and 2.0 times higher, respectively, than those of Ag/Ga_2O_3. It is worth mentioning that the formation rate of CO in this work showed great improvement when compared with the other representative photocatalysts reported in the literatures for the photocatalytic conversion of CO_2 by H_2O.[22-29] The conversion efficiency over $Ag\text{-}Cr/Ga_2O_3$ is as high as 0.60% for the photocatalytic conversion of CO_2.

Table 1 Photocatalytic conversion of CO_2 by H_2O vs. different photocatalysts.[a]

Catalyst	Formation rate of products / μmol h^{-1}			Selec. toward CO
	H_2	O_2	CO	(%)
Bare Ga_2O_3	163	90.6	11.5	6.6
Ag/Ga_2O_3	219	166	140	38.9
Cr/Ga_2O_3	100	48.2	9.36	8.5
$Ag\text{-}Cr/Ga_2O_3$	92.9	281	480	83. 8

[a] Photocatalyst powder: 0.5 g, reaction solution volume: 1.0 L, additive: 0.1 M $NaHCO_3$, Ag loading amount: 1.0 mol%, Cr loading amount: 1.0 mol%, CO_2 flow rate: 30 mL min^{-1}, light source: 400 W high-pressure Hg lamp.

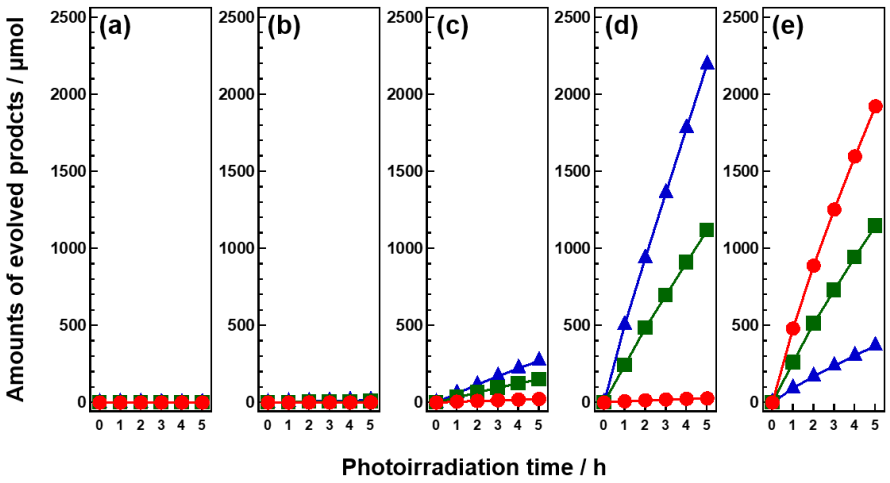

Figure 2 Amounts of H_2 (blue triangle), O_2 (green square), and CO (red circle) from controlled experiments for the photocatalytic conversion of CO_2 in water using the Ag-Cr/Ga_2O_3 photocatalyst. (a) dark condition; (b) no photocatalyst; (c) no additive; (d) with Ar gas flow; (e) typical condition. Photocatalyst powder: 0.5 g, reaction solution volume: 1.0 L, additive: 0.1 M $NaHCO_3$, Ag loading amount: 1.0 mol%, Cr loading amount: 1.0 mol%, CO_2 flow rate: 30 mL min^{-1}, light source: 400 W high-pressure Hg lamp.

Almost no product was detected under dark conditions (Figure 2a) or without a photocatalyst (Figure 2b). Using inert Ar instead of CO_2 or not using an $NaHCO_3$ additive led to the primary formation of H_2 (Figures 2c and 2d). The best performance for the photocatalytic conversion of CO_2 was using Ag-Cr/Ga_2O_3 in an aqueous $NaHCO_3$ solution with bubbling CO_2 under photoirradiation (Figure 2e). Stoichiometric amounts of CO and H_2 as the conversion products and O_2 as the oxidation product were obtained, indicating that H_2O serves as an electron donor for the photocatalytic conversion of CO_2.

In the isotopic experiments using $^{13}CO_2$ over Ag-Cr/Ga_2O_3 (Figure 3), peaks corresponding to H_2, O_2, and CO were observed in the thermal conductivity detector-gas chromatogram (TCD-GC). The peak at m/z = 29 corresponds to the evolved ^{13}CO because the peak position is consistent with that detected by TCD-GC, and the detected ^{12}CO at m/z = 28 was negligible. Moreover, the amount of ^{13}CO detected by mass spectrometry was approximately equal to the total amount of CO determined using a flame ionization detector (FID-GC) (Figure 4). These results indicate that the evolved CO originated from the CO_2 introduced in the gas phase and not from the carbon contaminants.

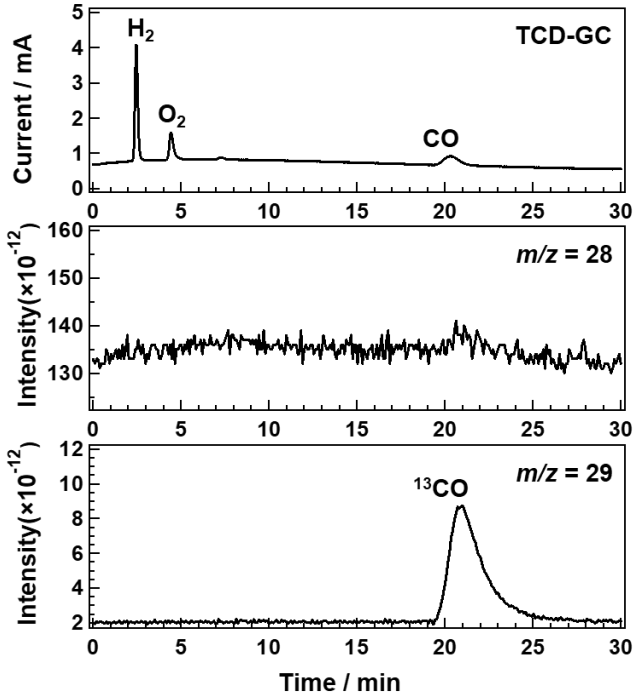

Figure 3 Gas chromatograms and mass spectra (*m/z* 28, 29) for the photocatalytic conversion of $^{13}CO_2$ by H_2O over Ag-Cr/Ga_2O_3. Photocatalyst powder: 0.5 g, reaction solution volume: 1.0 L, additive: 0.1 M $NaHCO_3$, Ag loading amount: 1.0 mol%, Cr loading amount: 1.0 mol%, CO_2 flow rate: 30 mL min^{-1}, light source: 400 W high-pressure Hg lamp.

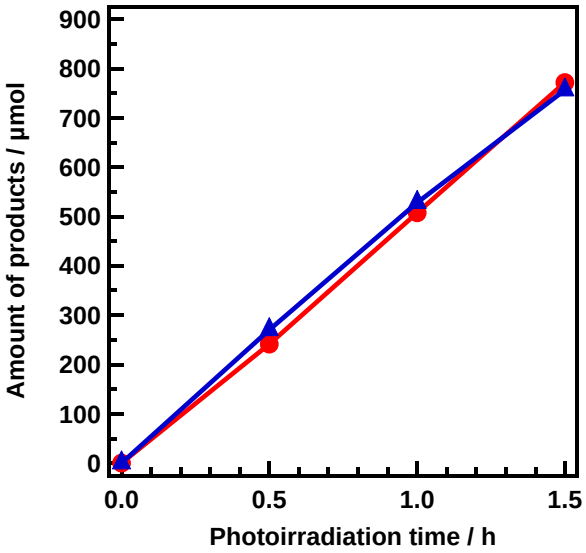

Figure 4 Time course of CO (blue triangles) and ^{13}CO (red circles) determined by FID-GC and mass, respectively, for the photocatalytic conversion of CO_2 over Ag-Cr/Ga_2O_3. Photocatalyst powder: 0.5 g,

reaction solution volume: 1.0 L, additive: 0.1 M $NaHCO_3$, Ag loading amount: 1.0 mol%, Cr loading amount: 1.0 mol%, CO_2 flow rate: 30 mL min^{-1}, light source: 400 W high-pressure Hg lamp.

Herein, an Ag-Cr dual co-catalyst was simultaneously photodeposited on Ga_2O_3 using $AgNO_3$ and $Cr(NO_3)_3$ as precursors, which is known as a simultaneous photodeposition (SPD) method.[34, 35] One focus of this work was determining the chemical states and distributions of the two co-catalysts in Ag-Cr/Ga_2O_3 to understand the significant enhancement of activity and selectivity for the photocatalytic conversion of CO_2.

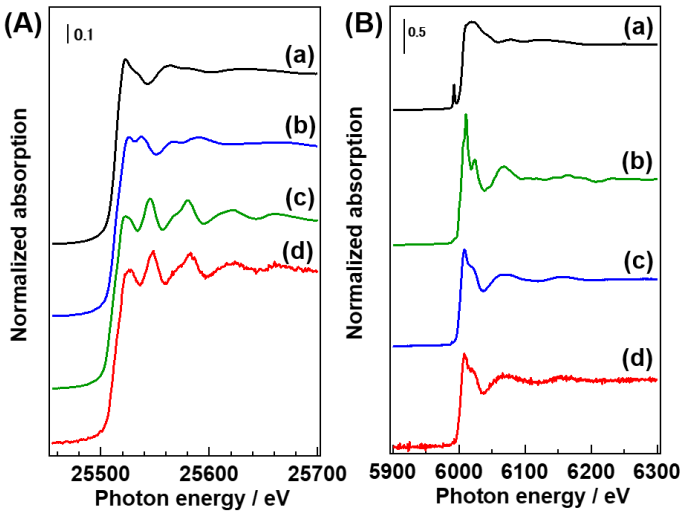

Figure 5 (A) Ag K-edge XANES of (a) Ag_2CO_3, (b) Ag_2O, (c) Ag foil, and (d) Ag-Cr/Ga_2O_3; (B) Cr K-edge XANES of (a) CrO_3, (b) Cr_2O_3, (c) $Cr(OH)_3{\cdot}xH_2O$, and (d) Ag-Cr/Ga_2O_3.

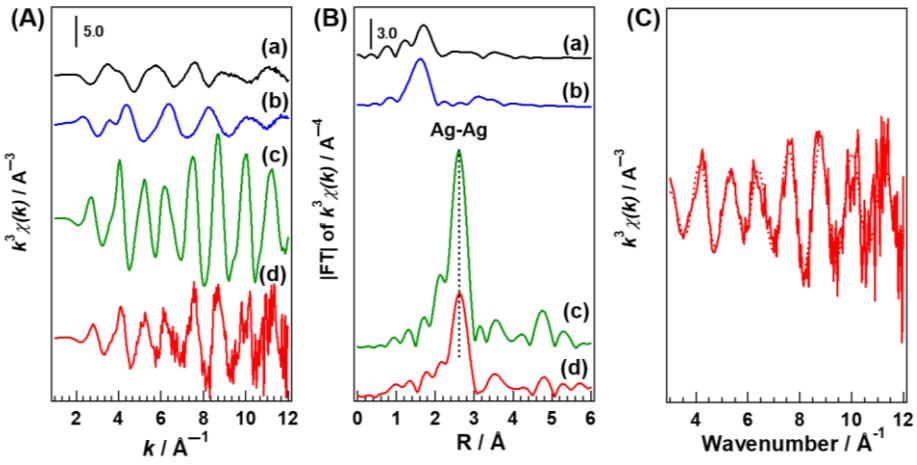

Figure 6 Ag K-edge (A) EXAFS and (B) Fourier transforms (FT) of the EXAFS spectra of (a) Ag_2CO_3,

(b) Ag_2O, (c) Ag foil, and (d) Ag-Cr/Ga_2O_3; and (C) Fourier-filtered EXAFS function (solid line) and resulting curve fit (dotted line) for the main peak appearing at 2.0–3.0 Å in FT of k^3-weighted EXAFS (Ag-Cr/Ga_2O_3 spectrum in Figure 6B).

Table 2 Curve-fitting analysis of Fourier-transformed EXAFS of Ag-Cr/Ga_2O_3.

Samples	Scatter atom	N[a]	R[b] (Å)	Δ(σ^2)[c] (Å^2)	Rf[d]
Ag-Cr/Ga_2O_3	Ag	4.80	2.87	1.08×10^{-2}	5.77×10^{-3}
Ag foil[e]	Ag	(12)	2.89	–	–

[a] Coordination number, [b] Bond distance, [c] Debye−Waller factor, [d] Residual factor, [e] Data from X-ray crystallography

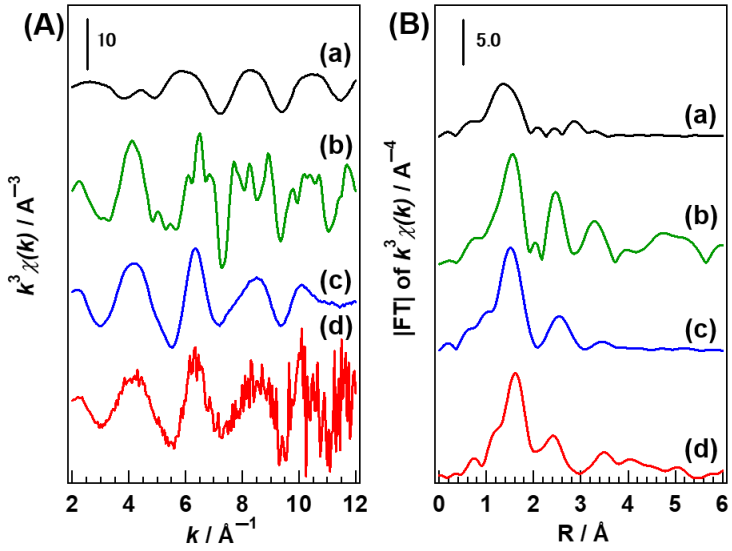

Figure 7 Cr K-edge (A) EXAFS and (B) Fourier transforms (FT) EXAFS spectra of (a) CrO_3, (b) Cr_2O_3, (c) $Cr(OH)_3{\cdot}xH_2O$, and (d) Ag-Cr/Ga_2O_3.

The chemical states of Ag and Cr in Ag-Cr/Ga_2O_3 were characterized using X-ray absorption fine structure (XAFS) measurements. Figures 5A and 5B show the Ag and Cr K-edge X-ray absorption near edge structure (XANES) spectra of Ag-Cr/Ga_2O_3, respectively. In these experiments, Ag_2CO_3, Ag_2O, Ag foil, CrO_3, Cr_2O_3, and $Cr(OH)_3{\cdot}xH_2O$ were used as references. The absorption edges in the Ag and Cr K-edge XANES spectra were similar to those of Ag foil and $Cr(OH)_3{\cdot}xH_2O$, which indicates that the Ag and Cr elements loaded on the surface of Ga_2O_3 were zero valent Ag species (Ag^0) and

trivalent Cr species (Cr^{3+}), respectively. As shown in Figure 6B, the peak at 2.6 Å is assigned to the Ag-Ag shell. Inverse Fourier transform of the Ag-Cr/Ga_2O_3 spectrum at 2.6 Å (R = 2.0–3.0 Å) in Figure 6B gives the EXAFS oscillation of Ag-Ag shell, as shown in Figure 6C. The dotted line in Figure 6C shows the result of a curve-fitting analysis using Ag-Ag shell parameters in the k region of 3.0–14.0 $Å^{-1}$. A simulated spectrum fitted well with the experimental one. As shown in Table 2, the curve-fitting analysis of the peak at 2.6 Å showed that this peak can be assigned to Ag-Ag shell with a coordination number of 4.8 and bond distance 2.87 Å, which is smaller with Ag foil.[37] The height of Ag-Ag shell peak of Ag-Cr/Ga_2O_3 was lower than that of Ag foil, which indicates that the particle size of Ag in Ag-Cr/Ga_2O_3 is smaller than Ag foil. As shown in Figure 7B, the peak with the largest FT moduli at 1.7 Å is assigned to oxygen atoms in the first coordination sphere of Cr (Cr-O). At further radial distance of about 2.6 Å and 3.2 Å with smaller FT moduli are assigned as contributions from distal Cr atoms (Cr-Cr).[38] The corresponding extended Ag and Cr K-edge XAFS (EXAFS) and the specific characteristic distances of Ag-Ag and Cr-(O)-Cr shell peaks in the Fourier transforms of EXAFS spectra (detail parameters are shown in Figures 6, 7, and Table 2) further confirm that the Ag and Cr species act as Ag metal and $Cr(OH)_3{\cdot}xH_2O$, respectively.[38]

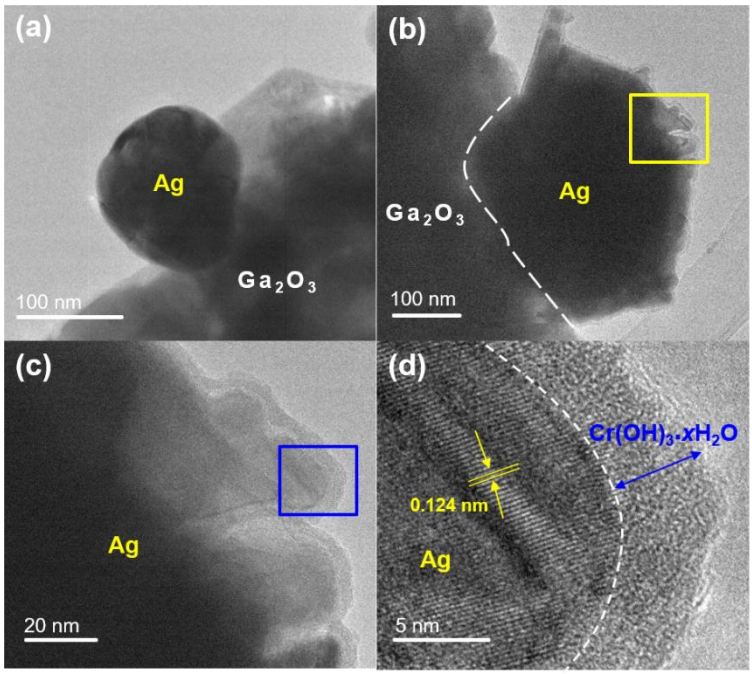

Figure 8 TEM images of (a) Ag/Ga_2O_3; (b), (c) Ag-$Cr(OH)_3{\cdot}xH_2O$/Ga_2O_3; (d) High-resolution TEM (HRTEM) image of Ag-Cr core-shell structure ((c) and (d) are the enlarged TEM images of the yellow

rectangular in Figure 8b and blue rectangular in 8c, respectively).

Figures 8a and 8b show transmission electron microscope (TEM) images of Ag/Ga_2O_3 and $Ag\text{-}Cr(OH)_3{\cdot}xH_2O/Ga_2O_3$, respectively. Ag with nanoparticle structures were loaded on the surface of Ga_2O_3 for Ag/Ga_2O_3, while in the case of $Ag\text{-}Cr(OH)_3{\cdot}xH_2O/Ga_2O_3$, some secondary particles with an antenna-like structures were aggregated onto the primary Ag particles, as confirmed by a scanning electron microscope (SEM) image (Figure 9a). Energy-dispersive X-ray spectroscopy (EDS) mapping for $Ag\text{-}Cr(OH)_3{\cdot}xH_2O/Ga_2O_3$ indicated that the antenna-like structure particles were also composed of Ag (Figures 9b and 9c). From the enlarged TEM image in Figure 8c, an obviously thin layer with shallow contrast was observed outside the Ag nanoparticles. The high-resolution TEM (HRTEM) image in Figure 8d shows lattice fringes with an interplanar spacing of 0.124 nm for the core, which is ascribed to the (311) facet of Ag, and a $Cr(OH)_3{\cdot}xH_2O$ shell with an amorphous structure of about 3–5 nm coated onto the surface of the Ag core, which together forms a core-shell nanostructure. Figure 10 shows TEM images of another Ag-Cr co-catalyst, which further demonstrates that the $Cr(OH)_3{\cdot}xH_2O$ shell uniformly covers the surface of the Ag core.

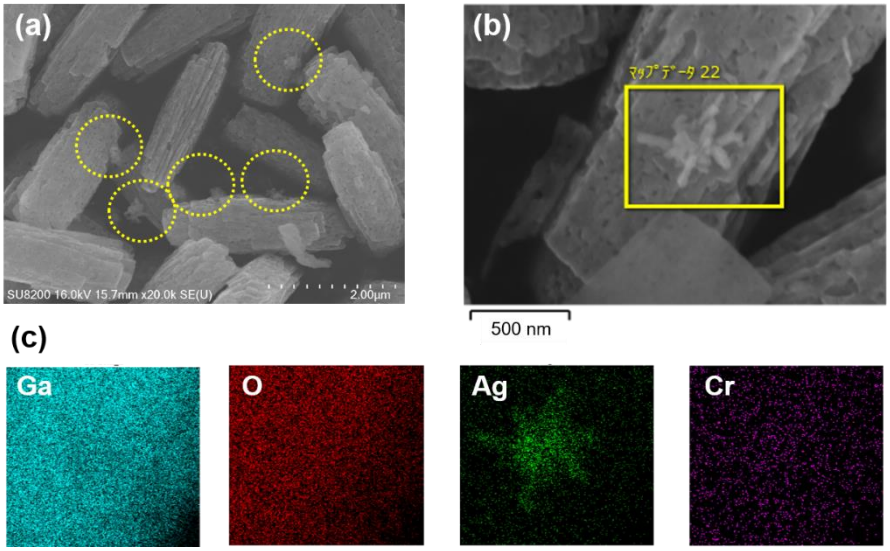

Figure 9 (a) SEM image of $Ag\text{-}Cr(OH)_3{\cdot}xH_2O/Ga_2O_3$; EDS analysis of $Ag\text{-}Cr(OH)_3{\cdot}xH_2O/Ga_2O_3$: (b) selected SEM images, (c) Ga, O, Ag, and Cr mapping images. Ag loading amount: 1.0 mol%, Cr loading amount: 1.0 mol%.

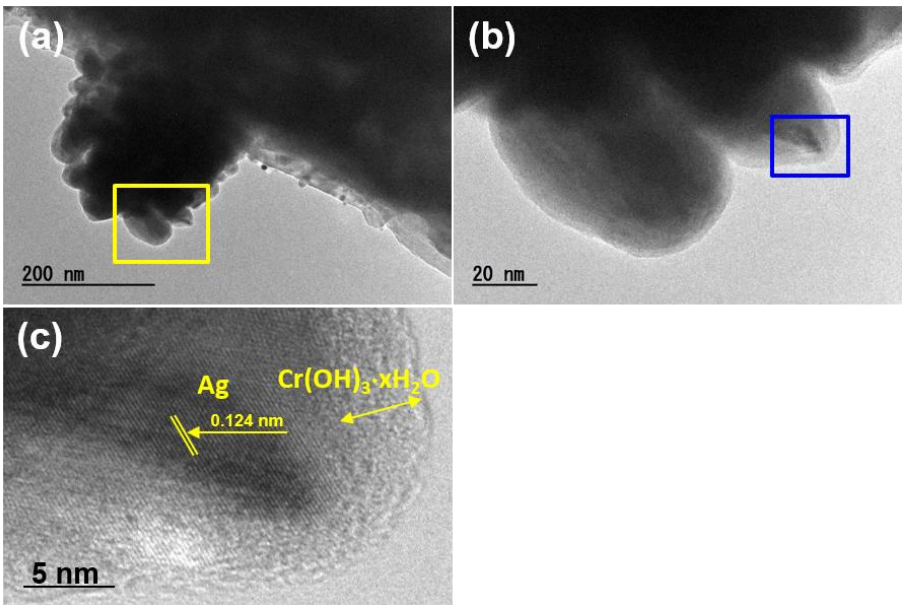

Figure 10 (a), (b) TEM images, and (c) high-resolution TEM (HRTEM) image of Ag-$Cr(OH)_3 \cdot xH_2O$ co-catalyst ((b) and (c) are the enlarged TEM images of the yellow rectangular in Figure 10a and blue rectangular in 10b, respectively).

It has been reported that a core-shell structure of Rh/Cr_2O_3 can suppress the backward reaction for overall water splitting, which is the formation of H_2O from H_2 and O_2.[39, 40] On the other hand, Ag has been used as an active co-catalyst for CO oxidation at low temperatures.[41-43] Therefore, during the photocatalytic conversion of CO_2, the backward reaction, which is oxidation of CO into CO_2, over an Ag co-catalyst would greatly decrease the photocatalytic efficiency for conversion of CO_2 into CO. This fact inspired us to confirm whether the backward reaction for the photocatalytic conversion of CO_2 can be suppressed by loading $Cr(OH)_3 \cdot xH_2O$ shell on the surface of Ag. The backward reaction was carried out in the same reactor as the photocatalytic conversion of CO_2, with CO and O_2 simultaneously bubbling into an ultrapure water solution. I then detected the formation rate of CO_2 gas under photoirradiation. As the backward reaction was carried out in an aqueous solution, water splitting could also happen during the photoirradiation, which produces H_2 and O_2. The possible reactions in the reactor are:

$$2CO + O_2 \rightarrow 2CO_2 \quad (1)$$

$$2H_2O \rightarrow 2H_2 + O_2 \quad (2)$$

According to Eqn. 1 and Eqn. 2, the consumed amounts of CO and O_2 can be calculated from the detected amounts of H_2, CO_2, CO, and O_2, the calcination details are shown as follows:

$$\text{Balance 1: Produced } CO_2/\text{Consumed CO} = \boldsymbol{R}_{CO2}/\boldsymbol{R}_{CO} \quad (3)$$

$$\text{Balance 2: } 0.5 \times \text{Produced } CO_2/\text{Consumed } O_2 = \boldsymbol{R}_{CO2}/2\boldsymbol{R}_{O2} \quad (4)$$

where R_x is the formation rate of species x

Table 3 Backward reactions for the photocatalytic reduction of CO_2 in H_2O over Ag/Ga_2O_3 and $Ag\text{-}Cr(OH)_3{\cdot}xH_2O/Ga_2O_3$.[b]

Catalyst	Flow rates of gases / μmol h^{-1}		Rates of detected gases / μmol h^{-1}				Balance 1 $\boldsymbol{R}_{CO2}/\boldsymbol{R}_{CO}$	Balance 2 $\boldsymbol{R}_{CO2}/2\boldsymbol{R}_{O2}$
	CO	**O_2**	**H_2**	**O_2**	**CO**	**CO_2**		
Ag/Ga_2O_3	487	301	20.8	260	382	103	0.98	1.01
	982	538	56.8	420	670	320	1.03	1.03
	2500	1590	7.45	1200	1750	820	1.09	1.02
$Ag\text{-}Cr/Ga_2O_3$	487	301	226	383	402	84.5	0.99	1.03
	982	538	282	590	782	202	1.01	1.02
	2500	1590	300	1560	2170	320	0.97	0.99

[b] Photocatalyst powder: 0.5 g, reaction solution: 1.0 L H_2O, Ag loading amount: 1.0 mol%, Cr loading amount: 1.0 mol%, light source: 400 W high-pressure Hg lamp.

Since about 480 μmol h^{-1} CO and 280 μmol h^{-1} O_2 were formed for the photocatalytic conversion of CO_2 over $Ag\text{-}Cr(OH)_3{\cdot}xH_2O/Ga_2O_3$, similar amounts of CO and O_2 were initially bubbled in the reactor (Table 3). The formation of a stoichiometric amount of CO_2 as the oxidation product with the

consumption amount of CO and O_2, indicated that a backward reaction for the photocatalytic conversion of CO_2 occurred on the surface of the Ag/Ga_2O_3 and Ag-$Cr(OH)_3$·xH_2O/Ga_2O_3 according to Eqn. 1. Compared to Ag/Ga_2O_3, the formation rate of CO_2 was much lower over Ag-$Cr(OH)_3$·xH_2O/Ga_2O_3 with same amount of CO and O_2 bubbling, especially when the flow rates of CO and O_2 were high, as shown in Figure 11, as more CO could be dissolved in the solution and absorbed on the photocatalyst. It is worth mentioning that there is still obvious CO_2 formed for the backward reaction over the Ag-$Cr(OH)_3$·xH_2O co-catalyst. As shown in TEM images of the as-prepared Ag-$Cr(OH)_3$·xH_2O/Ga_2O_3 in Figure 12, besides the uniform Ag-$Cr(OH)_3$·xH_2O core-shell structure, some Ag-$Cr(OH)_3$·xH_2O core-shell co-catalyst were covered by many small Ag particles. The exposure of Ag may lead to the formation of CO_2 over Ag-$Cr(OH)_3$·xH_2O/Ga_2O_3. These results demonstrate that the modification of the $Cr(OH)_3$·xH_2O thin layer on the surface of the Ag co-catalyst drastically suppressed the backward reaction for the photocatalytic conversion of CO_2. Consequently, the formation rate of CO and selectivity toward CO evolution were significantly enhanced over Ag-$Cr(OH)_3$·xH_2O/Ga_2O_3 as compared with Ag/Ga_2O_3.

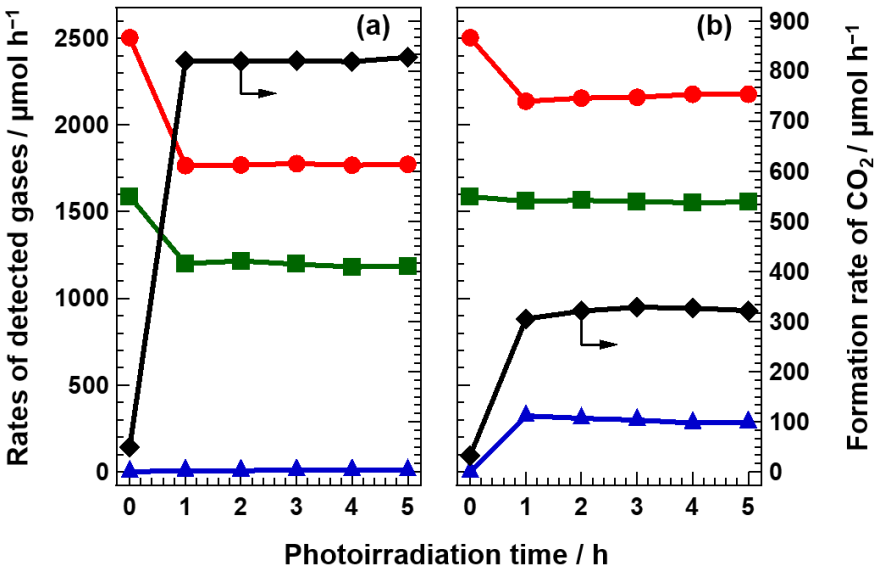

Figure 11 Rates of H_2 (blue triangle), O_2 (green square), CO (red circle) detected and the formation rate of CO_2 (black diamond) of the backward reaction for the photocatalytic conversion of CO_2 in H_2O over (a) Ag/Ga_2O_3 and (b) Ag-$Cr(OH)_3$·xH_2O/Ga_2O_3. Photocatalyst powder: 0.5 g, reaction solution: 1.0 L H_2O, flowing rates of gases: CO/Ar mixture gas (5.0%): 20 mL min^{-1}, O_2: 0.64 mL min^{-1}, Ar:

9.4 mL min^{-1}, solution: H_2O 1.0 L, Ag loading amount: 1.0 mol%, Cr loading amount: 1.0 mol%, light source: 400 W high-pressure Hg lamp.

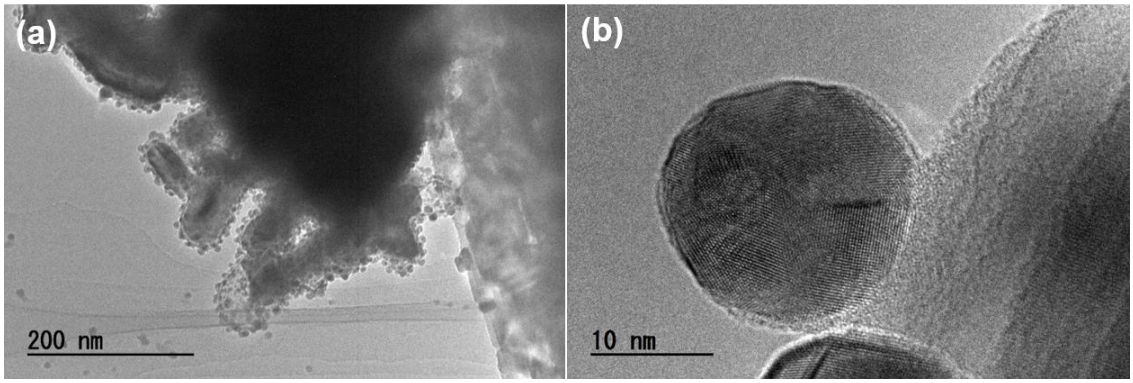

Figure 12 (a) TEM image and (b) HRTEM image of the as prepared Ag-$Cr(OH)_3{\cdot}xH_2O/Ga_2O_3$.

Lindbergh et al. have reported that the formation of $Cr(OH)_3{\cdot}xH_2O$ film on the surface of Pt cathode effectively hindered the reduction of O_2, while the hydrogen evolution could still proceed.[44] Yoshida et al. also confirmed this phenomenon using Cr_2O_3-coated metal electrodes.[39] The reason is considered to the selective permeation mechanism of $Cr(OH)_3{\cdot}xH_2O$ layer which is permeable to small hydroxide and/or hydrogen ions, and impermeable to the large O_2 species. Because the hydroxide are easily converted to carbonic compounds in the presence of a large amount of carbonates, it was expected that the $Cr(OH)_3{\cdot}xH_2O$ layer would change to $Cr_2(OH)_{2m}(CO_3)_{(3-m)}{\cdot}xH_2O$ under the flowing of CO_2 gas in an $NaHCO_3$ solution.[16] It has already reported that the same structure intermediates were formed in the case of rare-earth elements.[45] The formed $Cr_2(OH)_{2m}(CO_3)_{(3-m)}{\cdot}xH_2O$ layer continuously provides CO_2 molecules to the active sites in the Ag core for the photocatalytic conversion of CO_2, and prevents O_2 from penetrating deeply into the Ag co-catalyst. This selective permeation mechanism might suppress the backward reaction for the photocatalytic conversion of CO_2.

Conclusions

In conclusion, a facile core-shell structure Ag-$Cr(OH)_3{\cdot}xH_2O$ dual co-catalyst loaded Ga_2O_3 significantly improved the formation rate of CO (480 μmol h^{-1}) and selectivity toward CO evolution

(83.8%), compared with bare Ga_2O_3, Ag/Ga_2O_3, Cr/Ga_2O_3, and other Ag-metals/Ga_2O_3. The backward reaction tests, which produced CO_2 from CO and O_2 in H_2O, indicated that the modification of $Cr(OH)_3{\cdot}xH_2O$ on the surface of Ag co-catalyst drastically suppressed the backward reaction for the photocatalytic conversion of CO_2. This Ag-Cr dual co-catalyst modification strategy offers a facile approach for remarkably enhancing the photocatalytic efficiency for the conversion of CO_2 by H_2O.

References

1. J. Hansen, L. Nazarenko, R. Ruedy, M. Sato, J. Willis, A. Del Genio, D. Koch, A. Lacis, K. Lo and S. Menon, *Science*, 2005, **308**, 1431-1435.
2. W. Wang, S. Wang, X. Ma and J. Gong, *Chem. Soc. Rev.*, 2011, **40**, 3703-3727.
3. R. K. Yadav, G. H. Oh, N.-J. Park, A. Kumar, K.-j. Kong and J.-O. Baeg, *J. Am. Chem. Soc.*, 2014, **136**, 16728-16731.
4. J. L. White, M. F. Baruch, J. E. Pander III, Y. Hu, I. C. Fortmeyer, J. E. Park, T. Zhang, K. Liao, J. Gu and Y. Yan, *Chem. Rev.*, 2015, **115**, 12888-12935.
5. G. A. Olah, G. S. Prakash and A. Goeppert, *J. Am. Chem. Soc.*, 2011, **133**, 12881-12898.
6. M. Asadi, B. Kumar, A. Behranginia, B. A. Rosen, A. Baskin, N. Repnin, D. Pisasale, P. Phillips, W. Zhu and R. Haasch, *Nat. Commun.*, 2014, **55**:4470, DOI: 10.1038/ncomms5470.
7. Q. Lu, J. Rosen, Y. Zhou, G. S. Hutchings, Y. C. Kimmel, J. G. Chen and F. Jiao, *Nat. Commun.*, 2014, **55**:3242, DOI: 10.1038/ncomms4242.
8. W. M. Haynes, *CRC handbook of chemistry and physics*, CRC press, 2014.
9. P. S. Surdhar, S. P. Mezyk and D. A. Armstrong, *J. Phys. Chem.*, 1989, **93**, 3360-3363.
10. J. Qiao, Y. Liu, F. Hong and J. Zhang, *Chem. Soc. Rev.*, 2014, **43**, 631-675.
11. M. Halmann, *Nature*, 1978, **275**, 115-116.
12. T. Inoue, A. Fujishima, S. Konishi and K. Honda, *Nature*, 1979, **277**, 637-638.
13. N. M. Dimitrijevic, B. K. Vijayan, O. G. Poluektov, T. Rajh, K. A. Gray, H. He and P. Zapol, *J. Am. Chem. Soc.*, 2011, **133**, 3964-3971.
14. C. Wang, R. L. Thompson, J. Baltrus and C. Matranga, *J. Phys. Chem. Lett.*, 2009, **1**, 48-53.
15. Q. Liu, Y. Zhou, J. Kou, X. Chen, Z. Tian, J. Gao, S. Yan and Z. Zou, *J. Am. Chem. Soc.*, 2010,

132, 14385-14387.

16. W. Tu, Y. Zhou and Z. Zou, *Adv. Mater.*, 2014, **26**, 4607-4626.
17. V. P. Indrakanti, J. D. Kubicki and H. H. Schobert, *Energy Environ. Sci.*, 2009, **2**, 745-758.
18. J. Yang, D. Wang, H. Han and C. Li, *Acc. Chem. Res.*, 2013, **46**, 1900-1909.
19. S. C. Roy, O. K. Varghese, M. Paulose and C. A. Grimes, *ACS Nano*, 2010, **4**, 1259-1278.
20. T.-m. Su, Z.-z. Qin, H.-b. Ji, Y.-x. Jiang and G. Huang, *Environ. Chem. Lett.*, 2016, **14**, 99-112.
21. Y. Hori, H. Wakebe, T. Tsukamoto and O. Koga, *Electrochim. Acta*, 1994, **39**, 1833-1839.
22. K. Iizuka, T. Wato, Y. Miseki, K. Saito and A. Kudo, *J. Am. Chem. Soc.*, 2011, **133**, 20863-20868.
23. H. Nakanishi, K. Iizuka, T. Takayama, A. Iwase and A. Kudo, *ChemSusChem*, 2016.
24. S. Iguchi, K. Teramura, S. Hosokawa and T. Tanaka, *Catal. Sci. Technol.*, 2016, **6**, 4978-4985.
25. Z. Huang, K. Teramura, S. Hosokawa and T. Tanaka, *Appl. Catal. B*, 2016, **199**, 272-281.
26. K. Teramura, H. Tatsumi, Z. Wang, S. Hosokawa and T. Tanaka, *Bull. Chem. Soc. Jpn.*, 2015, **88**, 431-437.
27. K. Teramura, Z. Wang, S. Hosokawa, Y. Sakata and T. Tanaka, *Chem. – Eur. J.*, 2014, **20**, 9906-9909.
28. Z. Wang, K. Teramura, S. Hosokawa and T. Tanaka, *Appl. Catal. B*, 2015, **163**, 241-247.
29. Z. Wang, K. Teramura, S. Hosokawa and T. Tanaka, *J. Mater. Chem. A*, 2015, **3**, 11313-11319.
30. M. Yamamoto, T. Yoshida, N. Yamamoto, T. Nomoto, Y. Yamamoto, S. Yagi and H. Yoshida, *J. Mater. Chem. A*, 2015, **3**, 16810-16816.
31. Q. Kang, T. Wang, P. Li, L. Liu, K. Chang, M. Li and J. Ye, *Angew. Chem. Int. Ed.*, 2015, **54**, 841-845.
32. Q. Zhai, S. Xie, W. Fan, Q. Zhang, Y. Wang, W. Deng and Y. Wang, *Angew. Chem.*, 2013, **125**, 5888-5891.
33. C.-W. Tsai, H. M. Chen, R.-S. Liu, K. Asakura and T.-S. Chan, *J. Phys. Chem. C*, 2011, **115**, 10180-10186.
34. K. Maeda, D. Lu, K. Teramura and K. Domen, *J. Mater. Chem.*, 2008, **18**, 3539-3542.
35. K. Maeda, D. Lu, K. Teramura and K. Domen, *Energy Environ. Sci.*, 2010, **3**, 470-477.
36. K. Maeda, K. Teramura, N. Saito, Y. Inoue and K. Domen, *J. Catal.*, 2006, **243**, 303-308.
37. H. A. Gasteiger, S. S. Kocha, B. Sompalli and F. T. Wagner, *Appl. Catal. B*, 2005, **56**, 9-35.

38. D. Rai, D. A. Moore, N. J. Hess, K. M. Rosso, L. Rao and S. M. Heald, *J. Solution Chem.*, 2007, **36**, 1261-1285.
39. M. Yoshida, K. Takanabe, K. Maeda, A. Ishikawa, J. Kubota, Y. Sakata, Y. Ikezawa and K. Domen, *J. Phys. Chem. C*, 2009, **113**, 10151-10157.
40. K. Maeda, K. Teramura, D. Lu, N. Saito, Y. Inoue and K. Domen, *J. Phys. Chem. C*, 2007, **111**, 7554-7560.
41. Z. Qu, M. Cheng, W. Huang and X. Bao, *J. Catal.*, 2005, **229**, 446-458.
42. X. Zhang, Z. Qu, X. Li, Q. Zhao, Y. Wang and X. Quan, *Catal. Commun.*, 2011, **16**, 11-14.
43. S. F. Chen, J. P. Li, K. Qian, W. P. Xu, Y. Lu, W. X. Huang and S. H. Yu, *Nano Res.*, 2010, **3**, 244-255.
44. G. Lindbergh and D. Simonsson, *Electrochim. Acta*, 1991, **36**, 1985-1994.
45. Z. Huang, K. Teramura, H. Asakura, S. Hosokawa and T. Tanaka, *J. Mater. Chem. A*, 2017, **5**, 19351-19357.

Chapter 4

Chromium hydroxide layer on Ag co-catalyst surface for highly selective photocatalytic conversion of CO_2 by H_2O

Abstract

In this study, I developed a Ag-Cr core-shell-structured (Ag@Cr) co-catalyst that modified the surface of the Ga_2O_3 photocatalyst. Compared to results provided by modifications with Ag co-catalysts and M-Cr dual co-catalysts (M = Au, Cu, Pd, and Pt), this change significantly improved the formation rate of CO and selectivity toward CO evolution in the photocatalytic conversion of CO_2 by the electron donor H_2O. As a result of this modification, the $Cr(OH)_3{\cdot}xH_2O$ shell changed to $Cr(OH)_x(CO_3)_y$ during the photocatalytic conversion. Furthermore, the thickness of the $Cr(OH)_3{\cdot}xH_2O$ shell was found to influence the photocatalytic performance. More specifically, $Cr(OH)_3{\cdot}xH_2O$ shells that were too thick or too thin were not beneficial to the CO evolution and suppression of H_2 evolution. Notably, the highest photocatalytic activity (525.3 μmol h^{-1}), selectivity toward CO evolution (85.2 %), and turnover number of CO to Ag (167) was achieved over 0.25 mol% (Ag@Cr)/Ga_2O_3. In addition to Ga_2O_3, the Ag@Cr co-catalyst modification strategy can also be applied to other photocatalyst materials such as $NaTaO_3$, $ZnGa_2O_4$, and $ZnGa_2O_4/Ga_2O_3$ for the highly effective photocatalytic conversion of CO_2 to CO when using H_2O as an electron donor.

Introduction

The photocatalytic conversion of CO_2 into hydrocarbon fuels has been consistently drawing attention for over 40 years.[1-7] The process is also referred to as artificial photosynthesis, based on the natural photosynthesis undertaken by green plants, where carbohydrates and O_2 are produced from CO_2 and H_2O using solar light energy. It represents a promising way to environmentally friendly energy production. Since Halmann[8] and Inoue et al.[9] reported the photocatalytic conversion of CO_2 using heterogeneous photocatalysts in the late 1970s, substantial efforts have been devoted to the semiconductor-based photocatalytic conversion of CO_2.[10-15] Our group has also reported various semiconductor-based photocatalysts, such as $ZnGa_2O_4$-modified Ga_2O_3,[16, 17] $La_2Ti_2O_7$,[18] Ta_2O_5,[19] $ZnGa_2O_4$,[20] $Sr_2KTa_5O_{15}$,[21] $ZnTa_2O_6$,[22] and $SrNb_2O_6$[23], which have shown relatively high photocatalytic activity and selectivity toward CO evolution for the photocatalytic conversion of CO_2 into CO by H_2O, which acts as an electron donor. As a result, I found that it was difficult to selectively activate CO_2 and suppress H_2 evolution in the photocatalytic conversion of CO_2 in H_2O over the bare semiconductors. However, the photocatalytic performance for the conversion of CO_2 was significantly facilitated by the modification of the photocatalyst surface with a Ag co-catalyst, which can offer reaction sites and promote charge separation.[10]

Various co-catalysts have been investigated for the photocatalytic conversion of CO_2 in the past 40 years.[11, 13, 15, 24, 25] In particular, the conversion of CO_2 into CO has been widely known as an alternative approach to generating syngas components.[26, 27] Ag is thought to be the most effective co-catalyst in the photocatalytic conversion of CO_2 into CO when using H_2O as an electron donor. Unfortunately, Ag, being a noble metal, is not an economical co-catalyst for practical applications. Therefore, there is an urgent need to develop cheap and sustainable photocatalysts for the photocatalytic conversion of CO_2 into CO with high efficiency.

Recently, dual co-catalysts with particular structures have attracted significant attention because of their excellent catalytic performances.[28-31] The simultaneous presence of two metals, both acting as co-catalysts, could lead to new catalytic properties that differ from those of monometallic co-catalysts.[32] Base metals such as Cu, Ni, and Cr could be used as dual co-catalysts, which is cost-effective for practical applications. Previously, I have reported that a Ag-Cr core-shell-structured co-

catalyst loaded on Ga_2O_3 (Ag@Cr/Ga_2O_3) significantly enhances the formation rate of CO and selectivity toward CO evolution in the photocatalytic conversion of CO_2 when H_2O was used as an electron donor.[33] However, detailed studies on the effect of the Ag and Cr species on the core-shell structure and photocatalytic activity have not yet been carried out. In this work, I investigated in detail the functions of the Ag and Cr species in the photocatalytic conversion of CO_2 with the aim to develop a cost-effective and sustainable co-catalyst. As a result, I found that the Ag@Cr core-shell-structured co-catalyst modification method could provide a general strategy for significantly improving the photocatalytic activity and selectivity toward CO evolution in the photocatalytic conversion of CO_2 using H_2O as an electron donor.

Experimental

Preparation of metal-Cr/Ga_2O_3.

A simultaneous photodeposition (SPD) method was used to load Cr and a series of metals on the surface of Ga_2O_3.[34-36] In each case, 1.0 g of Ga_2O_3 (Kojundo, 99.99%) powder was dispersed in 1.0 L of ultra-pure water containing the required amount of $Cr(NO_3)_3$ (95%, Kanto Chemicals Co.) and one of the specific metal precursors: $AgNO_3$, $PdCl_2$, $Cu(NO_3)_2$, H_2PtCl_6, or $HAuCl_4$ (all purchased from Wako Pure Chemicals Co.). The solution was completely degassed by a flow of Ar gas. The suspension was irradiated under a 400 W high-pressure Hg lamp under Ar gas flow for 1 h, followed by filtration and drying at room temperature. The calculated metal/Ga and Cr/Ga molar ratios were both 1.0 mol%.

Preparation of $Cr(OH)_3{\cdot}xH_2O$

$Cr(OH)_3{\cdot}xH_2O$ was prepared by an ammonia precipitation method. The hydroxylation was carried out by dripping ammonium hydroxide solution into $Cr(NO_3)_3$ aqueous solution (0.1 M, 100 mL) until the pH value reached to 9.5. After continuously stirring for 3 h, the suspension was filtered and dried in vacuum at 313 K for 12 h.

Preparation of $Cr(OH)_x(CO_3)_y$

The synthesized $Cr(OH)_3{\cdot}xH_2O$ (2.0 g) was dispersed in an $NaHCO_3$ solution (0.1 M, 1.0 L). CO_2 was bubbled into the solution at a flow rate of 30 mL min^{-1}. The suspension was stirred at 283 K for 20 h, and then filtered and dried in vacuum at 313 K for 12 h.

Characterization.

The morphologies of the as-prepared metal-Cr/Ga_2O_3 samples were observed by transmission electron microscopy (TEM, JEM−2100F, JEOL). Inductively coupled plasma-optical emission spectrometry (ICP-OES, iCAP7400, Thermo Fisher Scientific, Inc) was used to determine the metal compositions (Ag, Au, Cu, Pt, and Pd) and Cr species in the metal-Cr/Ga_2O_3 samples. The X-ray absorption fine structure (XAFS) of the Ag K-edge and Cr K-edge was measured at the beamline BL01B1 of Spring-8 (Japan Synchrotron Radiation Research Institute, Hyogo, Japan). $Cr(OH)_3{\cdot}xH_2O$ and $Cr(OH)_x(CO_3)_y$ samples prepared in-house were used as references. The preparation methods are provided in the supporting information.[37] All reference samples for the transmission mode measurements were diluted by boron nitride (BN, Wako Pure Chemicals Co.) and pressed into pellets with a diameter of 10 mm to give the appropriate absorption edge jump. Due to the low concentration of Ag and Cr in Ag@Cr/Ga_2O_3, 19ch Ge solid state detectors (SSDs) was used to obtain the Ag K-edge and Cr K-edge XAFS spectra of the Ag@Cr/Ga_2O_3 samples.

Photocatalytic conversion of CO_2

The photocatalytic reduction of CO_2 was carried out using a quasi-flowing batch system with an inner-irradiation-type reaction vessel at an ambient pressure. The synthesized photocatalyst (0.5 g) was dispersed in ultrapure water (1.0 L) containing $NaHCO_3$ at a concentration of 0.1 M. CO_2 was bubbled into the solution at a flow rate of 30 mL min^{-1}. The suspension was illuminated using a 400 W high-pressure mercury lamp with a quartz filter connected to a cooling system. The amounts of H_2 and O_2 evolved were detected using a thermal conductivity detector–gas chromatography system (TCD-GC, Shimadzu Corp; MS−5A column, Ar carrier). The amount of CO evolved was analyzed by a flame ionization detector–GC system with a methanizer (FID-GC, ShinCarbon ST column, N_2 carrier). High-performance liquid chromatography (HPLC, LC−4000, JASCO) was used to detect any liquid product.

The selectivity toward CO evolution compared to H_2 evolution and the balance between the consumed electrons (e^-) and holes (h^+) generated by charge transfer can be expressed by Eqns. (1) and (2), respectively:[38]

$$\text{Selectivity toward CO evolution (\%)} = 100 \times 2\boldsymbol{R}_{\mathbf{CO}}/(2\boldsymbol{R}_{\mathbf{CO}} + 2\boldsymbol{R}_{\mathbf{H2}}) \quad (1)$$

$$\text{Consumed } e^-/h^+ = (2\boldsymbol{R}_{\mathbf{CO}} + 2\boldsymbol{R}_{\mathbf{H2}})/4\boldsymbol{R}_{\mathbf{O2}} \quad (2)$$

where R_{CO}, R_{H2}, and R_{O2} represent the formation rates of CO, H_2, and O_2, respectively. The turnover number (TON)[39] for the evolution of CO, expressed against the total amount of Ag atoms loaded as a co-catalyst on the surface of Ga_2O_3 was calculated for the photocatalytic conversion of CO_2 by H_2O for 5 h using Eqn. (3).

$$TON_{CO/Ag} = \text{amount of CO evolved/amount of Ag atoms loaded} \quad (3)$$

Results and discussion

Table 1 Photocatalytic conversion of CO_2 by H_2O vs. different metal-Cr/Ga_2O_3.[a]

Catalyst	Formation rates of products / μmol h^{-1}			Selec. toward	Consumed
	H_2	O_2	CO	CO (%)	e^-/h^+
Ag-Cr/Ga_2O_3	92.9	281.2	480.3	83.8	1.02
Au–Cr/Ga_2O_3	2819.1	1463.4	0.3	0	0.96
Cu–Cr/Ga_2O_3	423.5	203.9	14.3	3.2	1.07
Pd–Cr/Ga_2O_3	4485.2	2418.0	0.2	0	0.93
Pt–Cr/Ga_2O_3	7970.3	4456.1	0.2	0	0.90

[a] Photocatalyst powder: 0.5 g, reaction solution volume: 1.0 L, additive: 0.1 M $NaHCO_3$, CO_2 flow rate: 30 mL min^{-1}, light source: 400 W high-pressure Hg lamp.

Table 1 shows the formation rates of H_2, O_2, and CO as products, and their selectivity toward CO evolution for the photocatalytic conversion of CO_2 over various metal-Cr/ Ga_2O_3 samples. In those reactions, no liquid product, such as formic acid, methanol, and ethanol, was detected in the reaction solution, and only CO was identified as a reduction product in the gaseous phase. Ag@Cr/Ga_2O_3 led to a significant formation of CO (480 μmol h^{-1}) and high selectivity toward CO evolution (83.8%), although low selectivity toward CO evolution (38.9%) was obtained over Ag/Ga_2O_3. In order to confirm the active site for the photocatalytic conversion of CO_2, I carried out the photocatalytic conversion of CO_2 by H_2O over Ga_2O_3 using various dual metal-Cr co-catalysts including metals such as Au, Cu, Pd, and Pt, which have all been reported to show activity for overall water splitting. The

exact amounts of metals (Au, Cu, Pt, and Pd) and Cr species loaded on the Ga_2O_3 photocatalyst were determined using ICP-OES, and the results are shown in Table 1. Very small amount of CO was generated in all cases, although most of them showed a similar metal-Cr core-shell structure, as shown in Figure 1. This result indicates that the role of Cr was limited, and it did not work as an active site for the reduction of CO_2 but mainly suppressed backward reactions such as the formation of H_2O from H_2 and O_2[40-42] and the oxidation of CO by O_2 on the co-catalyst metals.[33] This suggests that Ag works as an active site in the photocatalytic conversion of CO_2 into CO more effectively than the other metals.

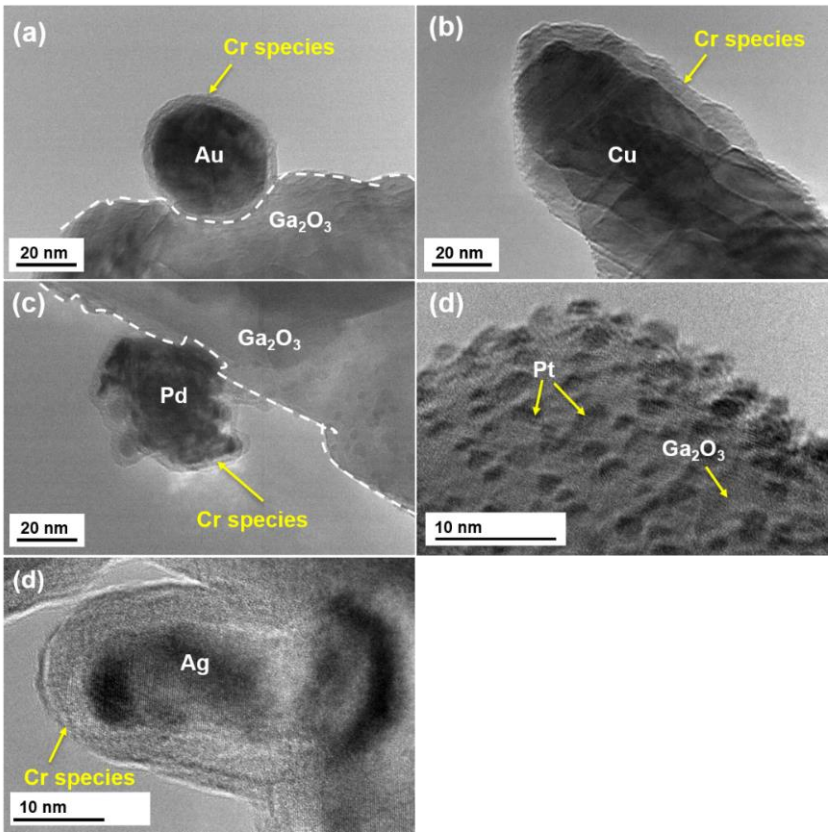

Figure 1 TEM images of various metal-Cr/Ga_2O_3. (a) Au-Cr/Ga_2O_3, (b) Cu-Cr/Ga_2O_3, (c) Pd-Cr/Ga_2O_3, (d) Pt-Cr/Ga_2O_3, and (e) Ag-Cr/Ga_2O_3.

Table 2 The actual molar ratio of M/Ga and Cr/Ga in different M-Cr/Ga_2O_3 samples estimated by ICP-OES.

M-Cr/Ga_2O_3	M/Ga (mol%)	Cr/Ga (mol%)
Ag-Cr/Ga_2O_3	0.89	0.82
Au-Cr/Ga_2O_3	0.48	0.83
Cu-Cr/Ga_2O_3	0.12	0.80
Pd-Cr/Ga_2O_3	0.94	0.81
Pt-Cr/Ga_2O_3	0.95	0.23

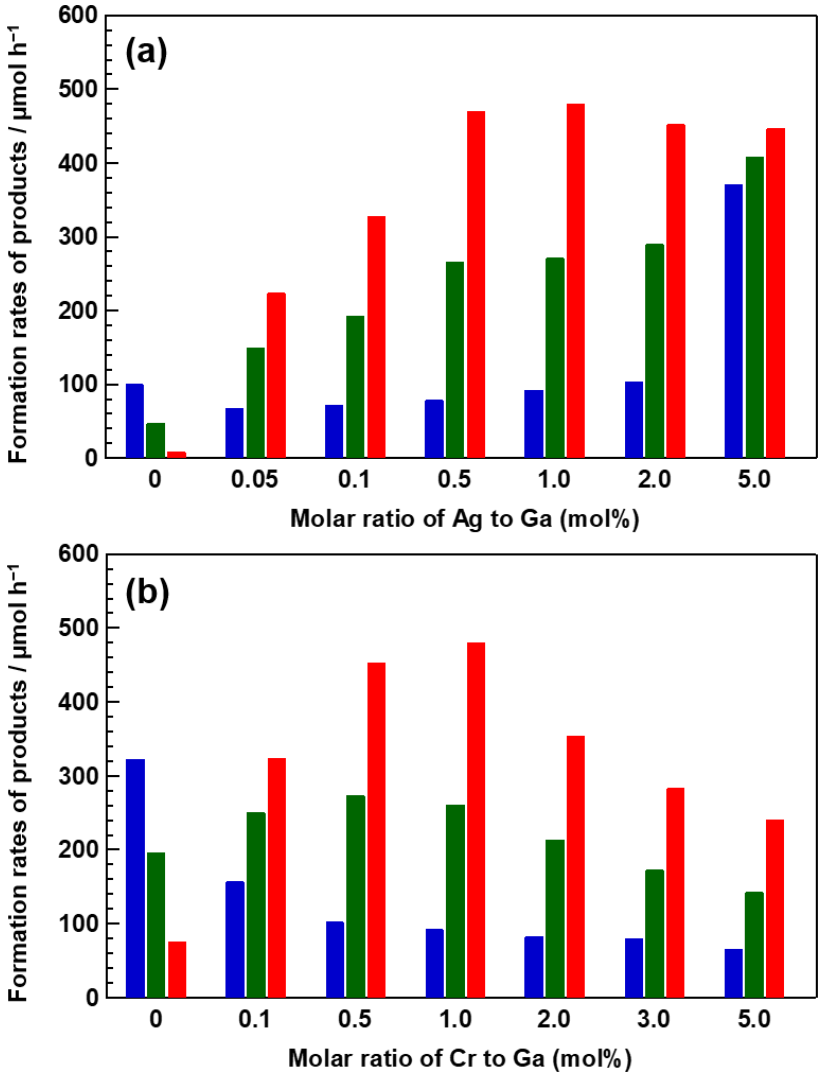

Figure 2 Formation rates of H_2 (blue), O_2 (green), and CO (red) for the photocatalytic conversion of CO_2 in H_2O over (a) different loading amounts of Ag, and (b) different loading amounts of Cr. The

actual amounts of Ag and Cr in the various Ag@Cr/Ga_2O_3 samples estimated by ICP-OES are shown in Table 3.

Table 3. The actual molar ratio of Ag/Ga and Cr/Ga in various Ag-Cr/Ga_2O_3 samples estimated by ICP-OES.

Sample	Ag/Ga (mol%)	Cr/Ga (mol%)	Ag/Cr
0.1 mol%Ag-1.0 mol%Cr/Ga_2O_3	0.10	0.80	0.13
0.25 mol%Ag-1.0 mol%Cr/Ga_2O_3	0.22	0.81	0.27
1.0 mol%Ag-1.0 mol%Cr/Ga_2O_3	0.89	0.82	1.09
5.0 mol%Ag-1.0 mol%Cr/Ga_2O_3	4.10	0.50	8.20
1.0 mol%Ag-0.1 mol%Cr/Ga_2O_3	0.73	0.09	8.11
1.0 mol%Ag-0.25 mol%Cr/Ga_2O_3	0.70	0.26	2.69
1.0 mol%Ag-1.0 mol%Cr/Ga_2O_3	0.89	0.82	1.09
1.0 mol%Ag-2.0 mol%Cr/Ga_2O_3	0.72	1.6	0.45
1.0 mol%Ag-3.0 mol%Cr/Ga_2O_3	0.33	2.2	0.14
1.0 mol%Ag-5.0 mol%Cr/Ga_2O_3	0.31	3.0	0.10
0.1 mol%(Ag-Cr)/Ga_2O_3	0.07	0.06	1.17
0.25 mol%(Ag-Cr)/Ga_2O_3	0.22	0.24	0.91
0.5 mol%(Ag-Cr)/Ga_2O_3	0.33	0.43	0.77
1.0 mol%(Ag-Cr)/Ga_2O_3	0.88	0.81	1.09
2.0 mol%(Ag-Cr)/Ga_2O_3	1.60	1.3	1.23

In order to clarify the effect of the Cr species, I adjusted the loading amounts of Ag and Cr on the surface of Ga_2O_3. Figure 2a shows the formation rates of H_2, O_2, and CO in the photocatalytic conversion of CO_2 for different loading amounts of Ag. More specifically, a marginal loading amount of Ag with Cr on the surface of Ga_2O_3 drastically improved the formation rate of CO: it increased with an increase in the loading amount of Ag from 0 to 1.0 mol% and slightly decreased on further increasing the loading amount of Ag. In contrast, the formation rate of H_2 showed a slight increase for Ag loading amounts of 0.05 to 2.0 mol% and dramatically increased at 5.0 mol%. This significant

change was assumed to be due to the fact that all Ag co-catalyst could not have been covered by the Cr species in the case of 5.0 mol% Ag@Cr/Ga_2O_3 because the loading amount of Cr was kept at 1.0 mol%. Figure 2b shows the formation rates of H_2, O_2, and CO in the photocatalytic conversion of CO_2 for different loading amounts of Cr. As can be seen, the formation rate of CO initially increased and then began to decrease at 2.0 mol% loading. The formation rate of H_2 decreased upon increasing the loading amount of Cr and became stable after the loading amount of Cr reached 1.0 mol%. This result suggests that the addition of Cr species into the Ag co-catalyst suppressed the evolution of H_2 and enhanced the formation rate of CO. However, an excess amount suppressed not only the formation of H_2 but also that of CO.

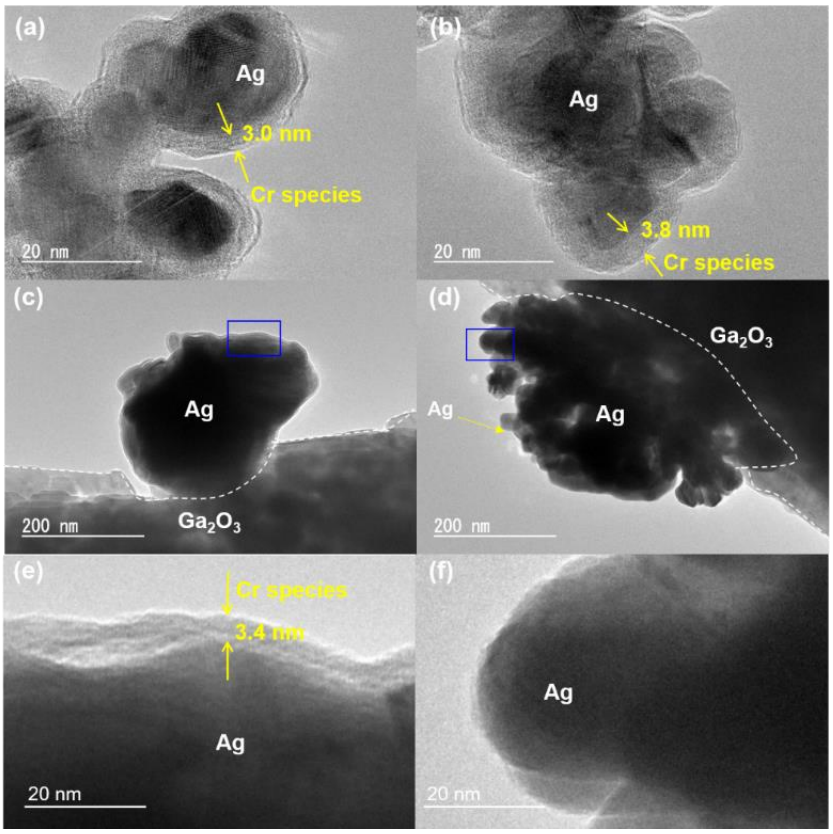

Figure 3 TEM images of Ag-Cr/Ga_2O_3 with different loading amounts of Ag: a) 0.05 mol%, (b) 0.1 mol%, (c) and (e) 1.0 mol%; (d) and (f) 5.0 mol%. ((e) and (f) are the enlarged TEM images of the blue rectangular in Figures (c) and (d), respectively). The loading amount of Cr is kept to 1.0 mol% (molar ratio of Cr to Ga).

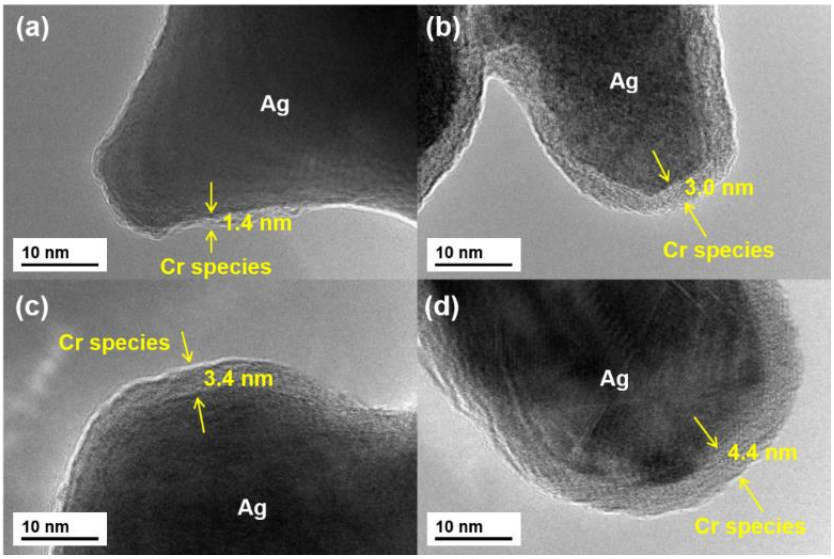

Figure 4 TEM images of Ag-Cr/Ga_2O_3 with different loading amounts of Cr: (a) 0.1 mol%, (b) 0.5 mol%, (c) 1.0 mol%; (d) 3.0 mol%. The loading amount of Ag is kept to 1.0 mol% (molar ratio of Ag to Ga).

TEM images of these catalysts showed that the Ag particles had formed aggregates ranging in size from several dozens of nanometers to hundreds of nanometers, depending on loading amount of Ag (Figure 3). Unsurprisingly, the thickness of the Cr shell increased upon increasing the loading amount of Cr (Figure 4). When the loading amount of Ag was high, such as 5.0 mol%, while that of Cr was kept at 1.0 mol%, the Ag particles became larger than those formed using a loading amount of Ag lower than 5.0 mol%, suggesting that, in this case, it was difficult to cover all the Ag nanoparticles by the Cr species introduced (Figures 3d and 3f). The exposed Ag particles would facilitate the formation of H_2, because Ag/Ga_2O_3 favors the evolution of H_2 and the Ag co-catalyst would increase the backward reaction for the photocatalytic conversion of CO_2.[33] As a result of both the Ag and Cr loading amounts being optimal, Ag(1.0 mol%)@Cr(1.0 mol%)/Ga_2O_3 exhibited the highest formation rate of CO (480 μmol h^{-1}) and selectivity toward CO evolution (83.8%). In order to enhance the formation of CO and suppress the production of H_2, it is critical to completely wrap all Ag particles with sufficient Cr species. In this respect, an appropriate Ag-Cr ratio needs to be determined.

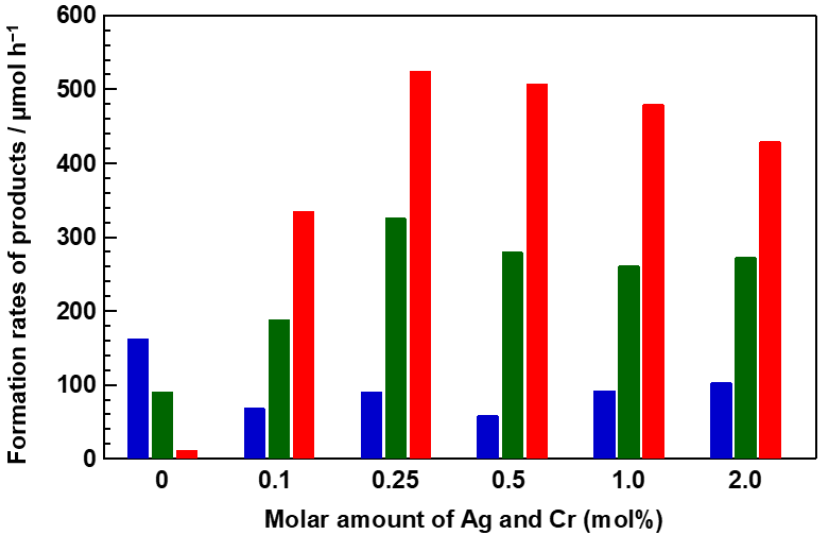

Figure 5 Formation rates of H_2 (blue), O_2 (green), and CO (red) for the photocatalytic conversion of CO_2 in H_2O over x mol% Ag@Cr/Ga_2O_3 (x = 0.1. 0.25, 0.5, 1.0, 2.0). The actual amounts of Ag and Cr in various Ag@Cr/Ga_2O_3 samples estimated by ICP-OES were shown in Table 3.

Figure 5 shows the formation rates of H_2, O_2, and CO for the photocatalytic conversion of CO_2 by H_2O over *x* mol% Ag@Cr/Ga_2O_3 (x = 0, 0.1, 0.25, 0.5, 1.0, 2.0). The loading amounts of both Ag and Cr were fixed to be the same (Ag-Cr = 1.0) because the high formation rate of CO and good selectivity toward CO evolution were obtained using Ag(1.0 mol%)@Cr(1.0 mol%)/Ga_2O_3. When bare Ga_2O_3 was modified with very small amounts of Ag and Cr (0.1 mol%), a large amount of CO was suddenly generated and the production of H_2 was suppressed. The formation rate of CO increased with an increase in the loading amounts of both Ag and Cr and plateaued at 0.25 mol%. Notably, the highest formation rate of CO (525 μmol h^{-1}) with good selectivity toward CO evolution (85.2%) was achieved over 0.25 mol% Ag@Cr/Ga_2O_3. As described above, almost the same activity and selectivity have already been obtained using 1.0 mol% loading, which indicates that one-fourth of the loading amount of Ag used initially was enough to achieve the relatively high activity and selectivity. However, the TON increased fourfold in this case and was as high as 167 for 5 h.

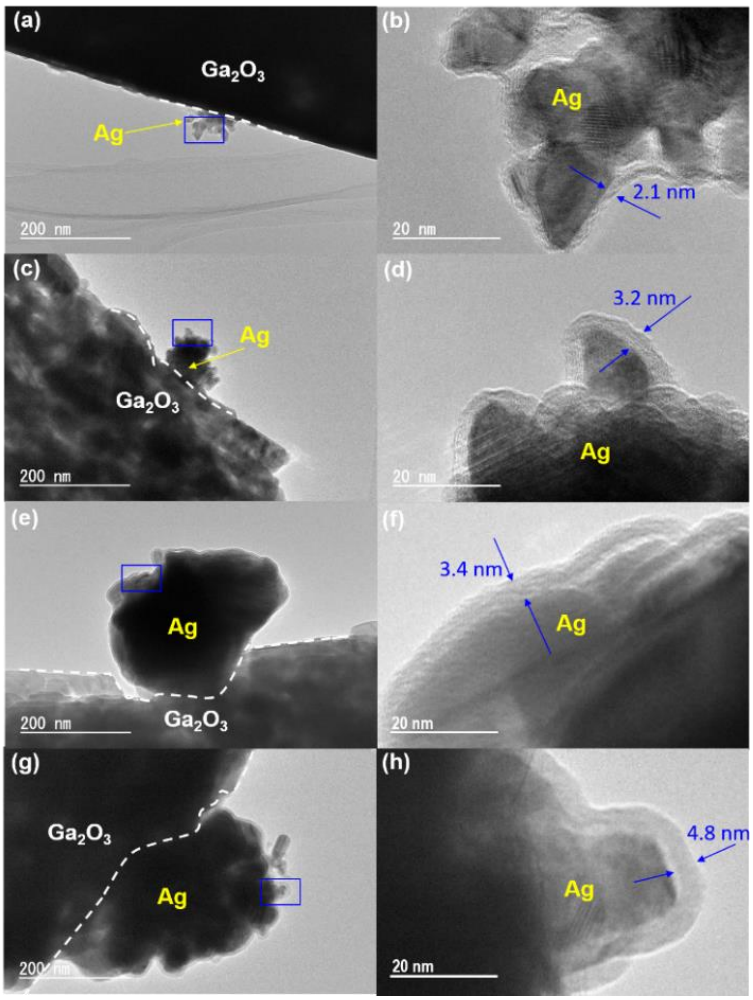

Figure 6 TEM images of x mol% (Ag@Cr)/Ga_2O_3. x = (a), (b) 0.1; (c), (d) 0.25; (e), (f) 1.0; and (g), (h) 2.0.

Figure 6 shows the TEM images of different *x* mol% Ag@Cr/Ga_2O_3 samples. When the loading amounts of Ag and Cr were low, Ag particles tens of nanometers in size were uniformly covered by the Cr shell. Increase in the loading amounts of Ag and Cr led to the aggregation of Ag particles from tens of nanometers to hundreds of nanometers in size, which indicates that the specific surface of one Ag particle decreased. Consequently, the thickness of the $Cr(OH)_3{\cdot}xH_2O$ shells increased from 2.1 to 4.8 nm upon increasing the loading amounts of Ag and Cr. I found that the thickness of the $Cr(OH)_3{\cdot}xH_2O$ shell covering the surface of the Ag particles significantly affected the photocatalytic performances in the conversion of CO_2 over Ag@Cr/Ga_2O_3.

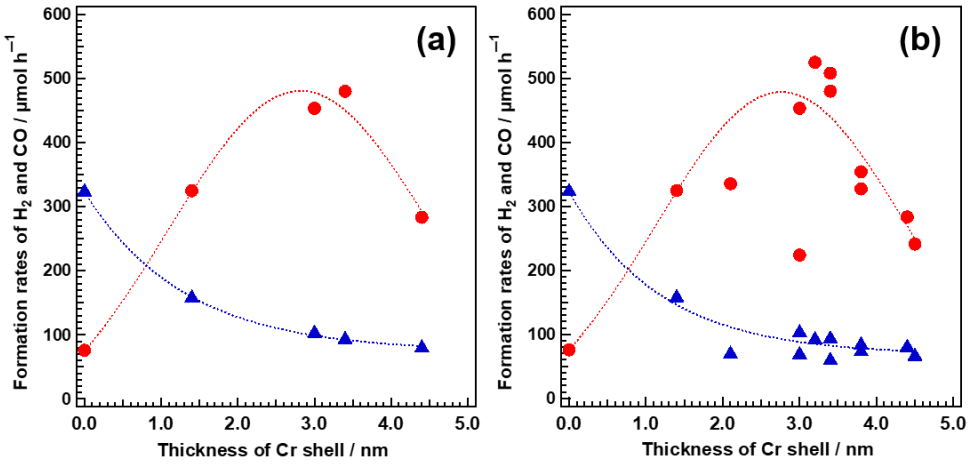

Figure 7 Dependence of the formation rates of CO (red solid circles) and H_2 (blue solid triangles) on the thickness of the $Cr(OH)_3{\cdot}xH_2O$ shell: (a) based on Figures 1b and S3, in which the amount of Ag is almost constant; (b) based on Figures 1, 2, S2, and S3, with various loading amount of Ag and Cr. The red and blue dotted lines represent the fitting curves for red and blue solid circles, respectively.

In order to eliminate the influence of the Ag structure, I maintained a constant loading amount of Ag in the investigation on the dependence of the formation rates of CO and H_2, i.e., the reduction products, on the thickness of the $Cr(OH)_3{\cdot}xH_2O$ shell, based on Figures 2b and 4. According to the obtained results, the formation rate of CO was found to increase upon increasing the Cr layer thickness from 0 to about 2.9 nm, from the beginning of the Cr coating to the point when the Cr layer thickness reached 2.9 nm. The formation rate of the H_2 curve matched well the exponential fitting curve, indicating that the formation rate of H_2 decreased upon increasing the thickness of the Cr layer, with a first-order dependence (Figure 7a). Furthermore, Figure 7b shows the dependence of the formation rates of CO and H_2 on the thickness of the $Cr(OH)_3{\cdot}xH_2O$ shell, based on Figures 2-6, in which both the Ag structure and thickness of the $Cr(OH)_3{\cdot}xH_2O$ shell were different. Surprisingly, the dependence of the formation rates of CO and H_2 on the thickness of the $Cr(OH)_3{\cdot}xH_2O$ shell showed very similar tendency as to when the structure of Ag was constant. When considering the fitting curves of the formation rates of CO, one can see that the highest formation rate of CO was achieved when the thickness of the $Cr(OH)_3{\cdot}xH_2O$ shell was about 2.8 nm. This result indicates that the thickness of the $Cr(OH)_3{\cdot}xH_2O$ shell covering the Ag particles displayed a greater influence on the formation rate of CO than on the structure of the Ag particles for the photocatalytic conversion of CO_2 over

Ag@Cr/Ga_2O_3. Based on the fitting curves and actual results, I concluded that the optimal thickness of the $Cr(OH)_3{\cdot}xH_2O$ shell to achieve the high formation rate of CO was in the range of 2.8–3.2 nm. Generally, the formation rate of products depends on the number of active sites. However, in our case, the active sites for the evolution of H_2 did not vanish, because, as Domen et al.[42, 43] reported, H^+, which is necessary for the reduction of CO_2 ($CO_2 + 2H^+ + 2e^- \rightarrow CO + 2H_2O$), can go through the thin Cr layer. Therefore, I expected that the concentration of CO_2 can be kept at a high level by using a thin Cr layer around the active sites so that the electrons generated by the charge transfer can go out through and reach the surface of the Ag co-catalyst.

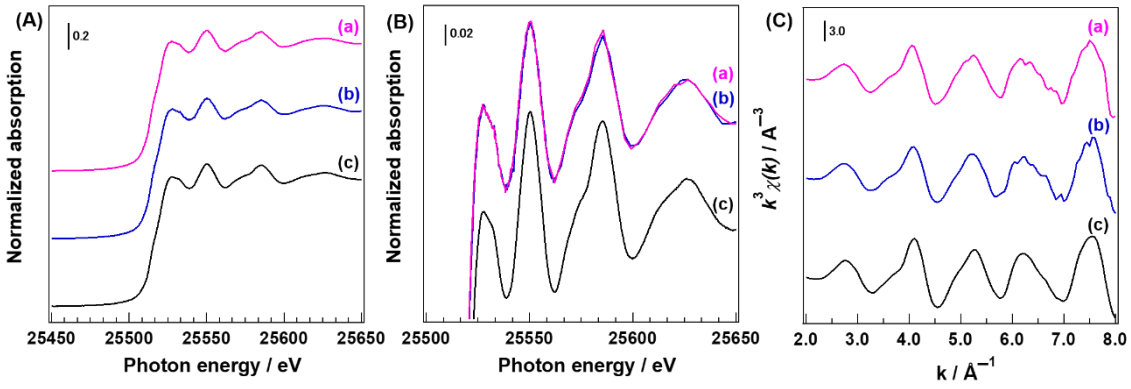

Figure 8 (A), (B) Ag K-edge XANES and (C) EXAFS spectra of (a) 1.0 mol% Ag@Cr/Ga_2O_3 after photoirradiation for 5 h (pink), (b) as-prepared 1.0 mol% Ag@Cr/Ga_2O_3 (blue), and (c) Ag foil (black) ((B) is the overlapped and enlarged Ag K-edge XANES spectrum in the photon energy range of 25500–25650 eV in (A)).

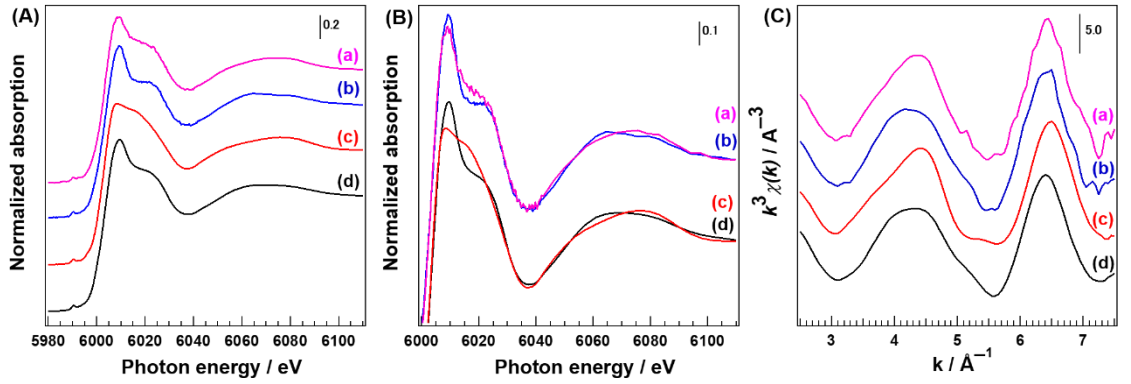

Figure 9 (A), (B) Cr K-edge X-ray absorption near edge structure (XANES) and (C) extended Cr K-edge XAFS (EXAFS) spectra of (a) 1.0 mol% Ag@Cr/Ga_2O_3 after photoirradiation for 5 h (pink), (b)

as-prepared 1.0 mol% Ag@Cr/Ga_2O_3 (blue), (c) $Cr(OH)_x(CO_3)_y$ (red), and (d) $Cr(OH)_3{\cdot}xH_2O$ (black) ((B) is the overlapped and enlarged Cr K-edge XANES spectrum in the photon energy range of 6000–6100 eV in (A)).

XAFS measurements were used to identify the chemical states and changes in the local structures of the Ag and Cr species on the surface of Ga_2O_3 during the photocatalytic conversion of CO_2. The Ag K-edge X-ray absorption near edge structure (XANES) and extended Ag K-edge XAFS (EXAFS) spectra shown in Figure 8 indicate that the Ag particles were in Ag^0 state, which was very stable during the photocatalytic conversion of CO_2 for 5 h. In addition, Figure 9 shows the Cr K-edge XANES spectra of 1.0 mol% Ag@Cr/Ga_2O_3 before and after photoirradiation for 5 h, with those of $Cr(OH)_3{\cdot}xH_2O$ and $Cr(OH)_x(CO_3)_y$ as references. The XANES spectrum of the as-prepared Ag@Cr/Ga_2O_3 was fairly consistent with that of $Cr(OH)_3{\cdot}xH_2O$, as reported previously.[33] Since the Cr K-edge XANES spectra of the $Cr(OH)_3{\cdot}xH_2O$ and $Cr(OH)_x(CO_3)_y$ references were very similar, in order to determine the changes after the photocatalytic conversion of CO_2 over Ag@Cr/Ga_2O_3, I overlapped their spectra and then compared them with the references (Figure 9B). The Cr K-edge XANES spectrum of Ag@Cr/Ga_2O_3 after photoirradiation for 5 h showed a lower absorption at 6010 eV and higher absorption at 6017 eV of white line, as compared with that obtained for the as-prepared Ag@Cr/Ga_2O_3. The corresponding Cr K-edge EXAFS spectrum in Figure 9C shows a slight change in the oscillation between 3.0 and 7.4 $Å^{-1}$ for the as-prepared Ag@Cr/Ga_2O_3 sample after photoirradiation for 5 h. This spectrum was consistent with that of $Cr(OH)_x(CO_3)_y$, thus indicating that the $Cr(OH)_3{\cdot}xH_2O$ shell covering the Ag co-catalyst absorbs CO_2 dissolved in the solution and transforms into $Cr(OH)_x(CO_3)_y$. Heald *et al.*[37] have reported that $Cr(OH)_3{\cdot}xH_2O$ could be converted into chromium carbonic compounds in the presence of a large amount of carbonate species. Notably, the differences between the Cr K-edge XANES and EXAFS spectra of $Cr(OH)_3{\cdot}xH_2O$ and $Cr(OH)_x(CO_3)_y$ reported in this paper were consistent with their results. When $Cr(OH)_3{\cdot}xH_2O$ was treated in an aqueous solution of $NaHCO_3$ under a flow of CO_2, it changed to $Cr(OH)_x(CO_3)_y$. In that case, the XANES and EXAFS spectra showed the same trend as that of Ag@Cr/Ga_2O_3. Therefore, I concluded that the $Cr(OH)_3{\cdot}xH_2O$ species in 1.0 mol% Ag@Cr/Ga_2O_3 changed to $Cr(OH)_x(CO_3)_y$ in the $NaHCO_3$ solution under CO_2 flow during the photocatalytic conversion of CO_2. The formation of the $Cr(OH)_x(CO_3)_y$ shell significantly improved the concentration of carbon species on the surface of

the Ag active sites.

Since the reduction of CO_2 to CO and the reduction of protons into H_2 in the aqueous solution are two competitive processes, increasing the concentration of carbon species around the active sites would be beneficial to the reduction of CO_2. In this respect, I expected that the formation of CO could be promoted and that of H_2 could be suppressed by covering the Ag active sites with a $Cr(OH)_3{\cdot}xH_2O$ shell of suitable thickness. Moreover, because the Cr shell is not permeable to O_2, as previously reported,[42, 44] it appreciably suppresses the backward reaction of the photocatalytic conversion of CO_2,[33] which, in turn, further improves the photocatalytic activity for the evolution of CO.

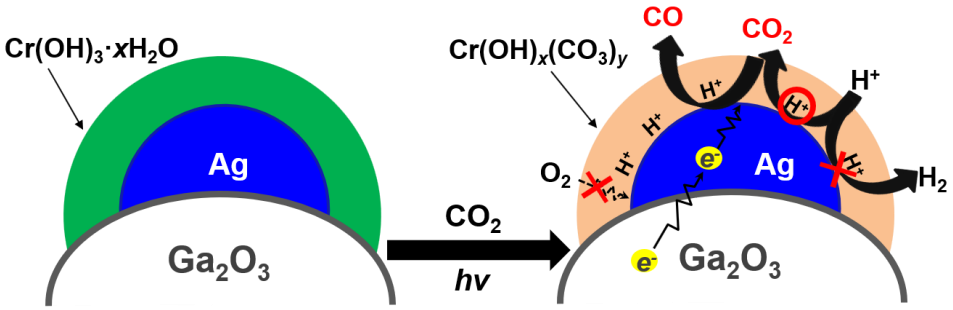

Scheme 1 Schematic illustration of the mechanism for the photocatalytic conversion of CO_2 into CO on $Ag@Cr/Ga_2O_3$

Here, I propose a mechanism for the photocatalytic conversion of CO_2 into CO on $Ag@Cr/Ga_2O_3$ (Scheme 1), according to which the CO_2 molecules dissolved in an aqueous solution of $NaHCO_3$ were incorporated into the $Cr(OH)_3{\cdot}xH_2O$ shell. This is followed by the formation of $Cr(OH)_x(CO_3)_y$, which indicates that CO_2-related species were liberally stored found around the Ag co-catalyst and were promptly supplied to the active sites. Therefore, CO_2 can be preferentially reduced into CO using two generated electrons and protons, because CO_2 is captured at the active site consistently. An increase in the amount of Cr can also lead to an increase in the thickness of the $Cr(OH)_3{\cdot}xH_2O$ shell (Figure 4), which makes it difficult for the carbon species and protons to permeate the $Cr(OH)_3{\cdot}xH_2O$ layer and reach the surface of Ag active site. Additionally, because the Cr species was not in favor of inducing the migration of photogenerated electrons from the bulk to the surface of the catalyst,[45] the evolution of CO will be inhibited if the Cr shell is too thick. Only a Cr shell of suitable thickness loaded on the surface of the Ag core would provide the best photocatalytic performance for the conversion of CO_2.

Table 4 Photocatalytic conversion of CO_2 by H_2O over different photocatalysts.[b]

Catalyst	Co-catalyst	Formation rates of products / μmol h^{-1}			Selec. toward CO (%)	Consumed e^-/h^+
		H_2	O_2	CO		
$NaTaO_3$	Ag	248.4	154.2	67.7	21.4	1.02
	Ag@Cr	43.7	118.8	194.8	81.7	1.00
$ZnGa_2O_4$	Ag	2.8	30.2	59.5	95.5	1.03
	Ag@Cr	18.8	147.6	295.9	94.0	1.06
$ZnGa_2O_4/Ga_2O_3$	Ag	8.9	56.6	108.0	92.4	1.03
	Ag@Cr	17.6	116.7	218.7	92.6	1.01

[b] Photocatalyst powder: 0.5 g, reaction solution volume: 1.0 L, additive: 0.1 M $NaHCO_3$, Ag loading amount: 0.25 mol% (Ag/Ga), Cr loading amount: 0.25 mol% (Cr/Ga), CO_2 flow rate: 30 mL min^{-1}, light source: 400 W high-pressure Hg lamp.

Next, in order to confirm the general versatility of the Ag@Cr co-catalyst, I investigated further the photocatalytic performances of other Ag@Cr core-shell-structured co-catalyst-loaded photocatalysts such as $NaTaO_3$, $ZnGa_2O_4$, and $ZnGa_2O_4/Ga_2O_3$ for the conversion of CO_2. As shown in Table 4, only Ag-loaded $ZnGa_2O_4$ and $ZnGa_2O_4/Ga_2O_3$ showed high selectivity toward CO evolution, as reported in our previous work.[16, 20] After loading the Ag@Cr dual co-catalyst, the formation rate of CO improved significantly with high selectivity. Surprisingly, in the case of $NaTaO_3$, which has been reported to show high activity for overall water splitting,[46, 47] the formation rate of H_2 was dramatically suppressed whereas that of CO improved. This result suggests that the thin $Cr(OH)_3{\cdot}xH_2O$ layer suppresses the production of H_2 from H_2O as well as improves the formation rate of CO even in cases involving solid-state materials showing good activity for overall water splitting, such as Ga_2O_3 and $NaTaO_3$. The Ag@Cr core-shell-structured co-catalyst modification method provides a general strategy for significantly improving the efficiency of the photocatalytic conversion of CO_2 into CO by H_2O.

Conclusion

In this study, the functions of the Ag and Cr species in the photocatalytic conversion of CO_2 were clearly investigated. Ag acted as an active site for the photocatalytic conversion of CO_2 into CO, exhibiting better photocatalytic performance than other metals, such as Au, Pt, Cu, and Pd. Notably, the $Cr(OH)_3{\cdot}xH_2O$ layer on the surface of $Ag@Cr/Ga_2O_3$ changed to $Cr(OH)_x(CO_3)_y$ during the photocatalytic conversion of CO_2. According to the obtained results, a high amount of Ag and Cr would not be conducive to improving the activity for the photocatalytic conversion of CO_2. Notably, the most critical factor in the stated reaction was to ensure that the Ag particles were surrounded by a Cr shell of suitable thickness. The highest photocatalytic activity (525.3 μmol h^{-1}) with good selectivity toward CO evolution (85.2%) and high $TON_{CO/Ag}$ (167/5 h) was achieved over 0.25 mol% $Ag@Cr/Ga_2O_3$. Based on these results, I believe that this Ag@Cr dual co-catalyst modification strategy can be widely used to increase the photocatalytic activity and selectivity toward CO evolution through photocatalytic conversion of CO_2 by H_2O in an efficient and sustainable way.

References

1. J. L. White, M. F. Baruch, J. E. Pander Iii, Y. Hu, I. C. Fortmeyer, J. E. Park, T. Zhang, K. Liao, J. Gu, Y. Yan, T. W. Shaw, E. Abelev and A. B. Bocarsly, *Chem. Rev.*, 2015, **115**, 12888-12935.
2. J. Low, J. Yu and W. Ho, *J. Phys. Chem. Lett*, 2015, **6**, 4244-4251.
3. W. Tu, Y. Zhou and Z. Zou, *Adv. Mater.*, 2014, **26**, 4607-4626.
4. Z. Jiang, T. Xiao, V. á. Kuznetsov and P. á. Edwards, *Philos. Trans. R. Soc. London, Ser. A*, 2010, **368**, 3343-3364.
5. H. Arakawa, M. Aresta, J. N. Armor, M. A. Barteau, E. J. Beckman, A. T. Bell, J. E. Bercaw, C. Creutz, E. Dinjus and D. A. Dixon, *Chem. Rev.*, 2001, **101**, 953-996.
6. J. Barber, *Chem. Soc. Rev.*, 2009, **38**, 185-196.
7. G. Centi, S. Perathoner, G. Winè and M. Gangeri, *Green Chem.*, 2007, **9**, 671-678.
8. M. Halmann, *Nature*, 1978, **275**, 115-116.

9. T. Inoue, A. Fujishima, S. Konishi and K. Honda, *Nature*, 1979, **277**, 637-638.
10. K. Iizuka, T. Wato, Y. Miseki, K. Saito and A. Kudo, *J. Am. Chem. Soc.*, 2011, **133**, 20863-20868.
11. W.-N. Wang, W.-J. An, B. Ramalingam, S. Mukherjee, D. M. Niedzwiedzki, S. Gangopadhyay and P. Biswas, *J. Am. Chem. Soc.*, 2012, **134**, 11276-11281.
12. S. N. Habisreutinger, L. Schmidt-Mende and J. K. Stolarczyk, *Angew. Chem. Int. Ed.*, 2013, **52**, 7372-7408.
13. H. Nakanishi, K. Iizuka, T. Takayama, A. Iwase and A. Kudo, *ChemSusChem*, 2017, **10**, 112-118.
14. S. C. Yan, S. X. Ouyang, J. Gao, M. Yang, J. Y. Feng, X. X. Fan, L. J. Wan, Z. S. Li, J. H. Ye and Y. Zhou, *Angew. Chem.*, 2010, **122**, 6544-6548.
15. I. Shown, H.-C. Hsu, Y.-C. Chang, C.-H. Lin, P. K. Roy, A. Ganguly, C.-H. Wang, J.-K. Chang, C.-I. Wu and L.-C. Chen, *Nano Lett.*, 2014, **14**, 6097-6103.
16. K. Teramura, Z. Wang, S. Hosokawa, Y. Sakata and T. Tanaka, *Chem. – Eur. J.*, 2014, **20**, 9906-9909.
17. Z. Wang, K. Teramura, Z. Huang, S. Hosokawa, Y. Sakata and T. Tanaka, *Catal. Sci. Technol.*, 2016, **6**, 1025-1032.
18. Z. Wang, K. Teramura, S. Hosokawa and T. Tanaka, *Appl. Catal. B*, 2015, **163**, 241-247.
19. K. Teramura, H. Tatsumi, Z. Wang, S. Hosokawa and T. Tanaka, *Bull. Chem. Soc. Jpn.*, 2015, **88**, 431-437.
20. Z. Wang, K. Teramura, S. Hosokawa and T. Tanaka, *J. Mater. Chem. A*, 2015, **3**, 11313-11319.
21. Z. Huang, K. Teramura, H. Asakura, S. Hosokawa and T. Tanaka, *J. Mater. Chem. A*, 2017, **5**, 19351-19357.
22. S. Iguchi, K. Teramura, S. Hosokawa and T. Tanaka, *Catal. Sci. Technol.*, 2016, **6**, 4978-4985.
23. R. Pang, K. Teramura, H. Asakura, S. Hosokawa and T. Tanaka, *Appl. Catal. B*, 2017, **218**, 770-778.
24. V. P. Indrakanti, J. D. Kubicki and H. H. Schobert, *Energy Environ. Sci.*, 2009, **2**, 745-758.
25. S. C. Roy, O. K. Varghese, M. Paulose and C. A. Grimes, *ACS Nano*, 2010, **4**, 1259-1278.
26. M. Asadi, B. Kumar, A. Behranginia, B. A. Rosen, A. Baskin, N. Repnin, D. Pisasale, P. Phillips, W. Zhu and R. Haasch, *Nat. Commun.*, 2014, **55**:4470, DOI: 10.1038/ncomms5470.

27. Q. Lu, J. Rosen, Y. Zhou, G. S. Hutchings, Y. C. Kimmel, J. G. Chen and F. Jiao, *Nat. Commun.*, 2014, **55**:3242, DOI: 10.1038/ncomms4242.

28. C.-W. Tsai, H. M. Chen, R.-S. Liu, K. Asakura and T.-S. Chan, *J. Phys. Chem. C*, 2011, **115**, 10180-10186.

29. S. t. Neaţu, J. A. Maciá-Agulló, P. Concepción and H. Garcia, *J. Am. Chem. Soc.*, 2014, **136**, 15969-15976.

30. Q. Zhai, S. Xie, W. Fan, Q. Zhang, Y. Wang, W. Deng and Y. Wang, *Angew. Chem.*, 2013, **125**, 5888-5891.

31. X. Zhang, F. Han, B. Shi, S. Farsinezhad, G. P. Dechaine and K. Shankar, *Angew. Chem. Int. Ed.*, 2012, **51**, 12732-12735.

32. J. Yang, D. Wang, H. Han and C. Li, *Acc. Chem. Res.*, 2013, **46**, 1900-1909.

33. R. Pang, K. Teramura, H. Tatsumi, H. Asakura, S. Hosokawa and T. Tanaka, *Chem. Commun.*, 2018, **54**, 1053-1056.

34. K. Maeda, D. Lu, K. Teramura and K. Domen, *Energy Environ. Sci.*, 2010, **3**, 470-477.

35. K. Maeda, D. Lu, K. Teramura and K. Domen, *J. Mater. Chem.*, 2008, **18**, 3539-3542.

36. T. Kanazawa and K. Maeda, *ACS Appl. Mater. Interfaces*, 2016, **8**, 7165-7172.

37. D. Rai, D. A. Moore, N. J. Hess, K. M. Rosso, L. Rao and S. M. Heald, *J. Solution Chem.*, 2007, **36**, 1261-1285.

38. K. Teramura and T. Tanaka, *Phys. Chem. Chem. Phys.*, 2018, **20**, 8423-8431.

39. S. Kozuch and J. M. L. Martin, *ACS Catalysis*, 2012, **2**, 2787-2794.

40. K. Maeda, K. Teramura, H. Masuda, T. Takata, N. Saito, Y. Inoue and K. Domen, *J. Phys. Chem. B*, 2006, **110**, 13107-13112.

41. K. Maeda, K. Teramura, D. Lu, N. Saito, Y. Inoue and K. Domen, *Angew. Chem.*, 2006, **118**, 7970-7973.

42. M. Yoshida, K. Takanabe, K. Maeda, A. Ishikawa, J. Kubota, Y. Sakata, Y. Ikezawa and K. Domen, *J. Phys. Chem. C*, 2009, **113**, 10151-10157.

43. K. Maeda, K. Teramura, D. Lu, N. Saito, Y. Inoue and K. Domen, *J. Phys. Chem. C*, 2007, **111**, 7554-7560.

44. K. Maeda, A. Xiong, T. Yoshinaga, T. Ikeda, N. Sakamoto, T. Hisatomi, M. Takashima, D. Lu,

M. Kanehara and T. Setoyama, *Angew. Chem.*, 2010, **122**, 4190-4193.

45. K. Maeda, K. Teramura, N. Saito, Y. Inoue and K. Domen, *J. Catal.*, 2006, **243**, 303-308.

46. H. Kato and A. Kudo, *Catal. Lett.*, 1999, **58**, 153-155.

47. H. Kato and A. Kudo, *J. Phys. Chem. B*, 2001, **105**, 4285-4292.

Chapter 5

Effect of Cr species on photocatalytic stability during the conversion of CO_2 by H_2O

Abstract

$Ag@Cr/Ga_2O_3$ is one of the most active photocatalysts for the photocatalytic conversion of CO_2 by H_2O; however, the formation rate of CO steadily decreases with increasing photoirradiation time. In this study, the reasons for the decreasing CO evolution were investigated in detail. The formation rate of CO was strongly dependent on the amount of Cr^{3+} in $Ag@Cr/Ga_2O_3$. Dissolution of Cr^{3+} during the reaction led to a decrease in the thickness of the $Cr(OH)_3 \cdot xH_2O$ shell. The Cr^{3+} in $Ag@Cr/Ga_2O_3$ was oxidized to dissolvable Cr^{6+} during the photocatalytic conversion of CO_2 in a $NaHCO_3$ aqueous solution under UV light irradiation. $NaHCO_3$ as an additive facilitated the dissolution of Cr^{3+}.

Introduction

The anthropogenic emission of carbon dioxide (CO_2) into the atmosphere undoubtedly increases the global mean temperature, which in turn leads to a wide range of climate impacts.[1-6] Thus, there is an urgent need to accelerate the carbon cycle to solve energy and environmental problems. The photocatalytic conversion of CO_2 with H_2O into renewable solar fuels such as CO, HCOOH, HCHO, CH_3OH, and CH_4 (so-called artificial photosynthesis), is a promising approach to solve both energy and environmental issues that has attracted great attention since the 1970s.[7-12] However, there are two main challenges for the photocatalytic conversion of CO_2 by H_2O: (1) CO_2 is a very stable, linear, and centrally symmetric molecule, making it extremely difficult to convert into other compounds; and (2) photocatalytic water splitting occurs more easily than the photocatalytic conversion of CO_2 in an aqueous solution, leading to lower CO_2 conversion selectivity.[13-15] Since Kudo and coworkers reported that the photocatalytic conversion of CO_2 into CO precedes the conversion of H^+ into H_2 in an aqueous solution over Ag-loaded $BaLa_4Ti_4O_{15}$,[9] numerous photocatalysts have been reported for the highly selective photocatalytic conversion of CO_2 into CO using H_2O as an electron donor.[10, 16-19] Unfortunately, photocatalytic activity for the conversion of CO_2 is still quite low, far less than what is required for actual applications.

Recently, I reported a core-shell-structured $Ag@Cr(OH)_3{\cdot}xH_2O$ co-catalyst loaded-Ga_2O_3 ($Ag@Cr/Ga_2O_3$), which exhibited very high activity toward CO evolution (> 480 $\mu mol{\cdot}h^{-1}$) for the photocatalytic conversion of CO_2 where H_2O is used as an electron donor. The $Cr(OH)_3{\cdot}xH_2O$ shell on the surface of the Ag co-catalyst increased the adsorption of CO_2 and suppressed the backward reaction for the photocatalytic conversion of CO_2.[20-21] Modification of $Ag@Cr(OH)_3{\cdot}xH_2O$ co-catalyst on the surface of photocatalysts seems a promising approach to improve the formation rate of CO and simultaneously suppress the formation rate of H_2 for the photocatalytic conversion of CO_2 by H_2O. However, it has been reported that Cr^{3+} can be oxidized by some oxidants (e.g., O_2, manganese oxides, and hydroxyl radicals) to form soluble Cr^{6+}, which is toxic, pollutes the environment, and harms creatures.[22-25] Therefore, it is important to evaluate the stability of chromium-containing materials. Moreover, the stability of the photocatalyst is of great significance for evaluating its photocatalytic and practical performance. Maeda et al. have reported that the formation rates of H_2 and O_2 decreased with

increasing photoirradiation time beyond 10 h for the photocatalytic water splitting over Rh-Cr/$(Ga_{1-x}Zn_x)(N_{1-x}O_x)$.[26] Some reports have established that Cr^{3+} can be more easily oxidized to Cr^{6+} in the presence of alkali metal oxides or alkali metal salts.[27-29] Thus, it is proposed that $Cr(OH)_3 \cdot xH_2O$ in Ag@Cr/Ga_2O_3 will be oxidized to Cr^{6+} during the photocatalytic conversion of CO_2 in an aqueous solution containing $NaHCO_3$ under UV-light irradiation. Herein I investigated the Cr species present during the photocatalytic conversion of CO_2 and focused on the influence of Cr in Ag@Cr/Ga_2O_3 on structure and valence stability.

Experimental

Preparation of Ag@Cr/Ga_2O_3

Ag@Cr/Ga_2O_3 was prepared as described in our previous paper.[20] Briefly, 1.0 g of Ga_2O_3 (Kojundo, 99.99%) powder was dispersed in 1.0 L of ultra-pure water containing the necessary amount of $AgNO_3$ and $Cr(NO_3)_3$. The suspension was purged with Ar gas and then irradiated under a 400 W high-pressure Hg lamp with Ar gas flowing for 1.0 h, followed by filtration and drying at room temperature (~298 K).

Photocatalytic conversion of CO_2

The photocatalytic conversion of CO_2 was carried out using a flow system with an inner-irradiation-type reaction vessel at ambient pressure. The synthesized photocatalyst (0.5 g) was dispersed in ultrapure water (1.0 L) containing 0.1 M $NaHCO_3$. CO_2 was bubbled into the solution at a flow rate of 30 $mL \cdot min^{-1}$. The suspension was illuminated using a 400 W high-pressure Hg lamp with a quartz filter connected to a water-cooling system. The amount of CO evolved was analyzed by a flame ionization detector-GC with a methanizer (FID-GC, Shimadzu Corp; ShinCarbon ST column, N_2 carrier). The amount of evolved H_2 and O_2 were detected using a thermal conductivity detector-gas chromatography system (TCD-GC, Shimadzu Corp; MS-5A column, Ar carrier). The selectivity toward CO evolution compared to H_2 evolution and the balance between the consumed electrons (e^-) and holes (h^+) can be expressed by Eqn. (1) and (2), respectively:[10]

$$\text{Selectivity toward CO evolution (\%)} = 100 \times 2\boldsymbol{R}_{\mathbf{CO}}/(2\boldsymbol{R}_{\mathbf{CO}} + 2\boldsymbol{R}_{\mathbf{H2}}) \quad (1)$$

Consumed $e^-/h^+ = (2\boldsymbol{R}_{CO} + 2\boldsymbol{R}_{H2})/4\boldsymbol{R}_{O2}$ (2)

Here, $\boldsymbol{R}_{CO}$ and $\boldsymbol{R}_{H2}$ represent the formation rates of CO and H_2, respectively.

Characterization

The crystal phases of the samples were observed by powder X-ray diffractometry (XRD, Rigaku Multiflex) with Cu Kα radiation (λ = 0.154 nm) at a scan rate of $2°\cdot min^{-1}$. The morphology of the Ag@Cr co-catalyst was observed by transmission electron microscopy (TEM, JEM-2100F). Inductively coupled plasma-optical emission spectrometry (ICP-OES, iCAP7400, Thermo Fisher Scientific, Inc) was used for determining the composition of Ag and Cr in $Ag@Cr/Ga_2O_3$. Absorbance spectra were obtained using a multi-scan UV-Vis spectrophotometer (MCPD−7700, Ohtsuka, Japan).

Determination of Cr^{6+}

Cr^{6+} content was analyzed by a spectrophotometric standard addition method using 1,5-diphenylcarbazide (DPC).[30-31] If Cr^{6+} is present in the sample solution, it reacts with DPC to produce a pink color in an acidic solution. The DPC solution was prepared by dissolving 0.05 g of DPC (Wako pure chemical, Japan) in 10 mL of acetone, and then dispersing 1.0 mL of this DPC solution in 50 mL of H_2O. An aliquot (0.2 mL) of the sample solution was delivered into 5 mL of sulfuric acid (0.1 mol L^{-1}) containing 0.8 mL of the DPC solution. After the mixture remained stable for 5 min, the transmittance spectrum was measured using a multi-scan UV-Vis spectrophotometer (MCPD−7700, Ohtsuka, Japan). K_2CrO_4 standard solutions (1, 2, 5, 10, and 50 ppm) were used as reference solutions. The concentration of Cr^{6+} in solution was quantified by measuring the absorbance of the DPC-Cr^{6+} complex formed at 543 nm.

Results and discussion

Figure 1 shows the time course of the formation rates of CO, H_2, and O_2 during the photocatalytic conversion of CO_2 by H_2O over $Ag@Cr/Ga_2O_3$. In addition to CO and H_2 as the reduction products, a stoichiometric amount of O_2 as the oxidation product was obtained, suggesting that H_2O serves as the electron donor for the photocatalytic conversion of CO_2. After photoirradiation for 1 h, the formation rate of CO was as high as 494 $\mu mol\cdot h^{-1}$ with a selectivity toward CO evolution of ~87%. However, the rate decreased exponentially from 494 $\mu mol\cdot h^{-1}$ to 221 $\mu mol\cdot h^{-1}$ as photoirradiation time increased

from 1 h to 20 h. Conversely, the rate of H_2 formation remained stable after photoirradiation for 20 h, which led to a decrease in the selectivity toward CO evolution.

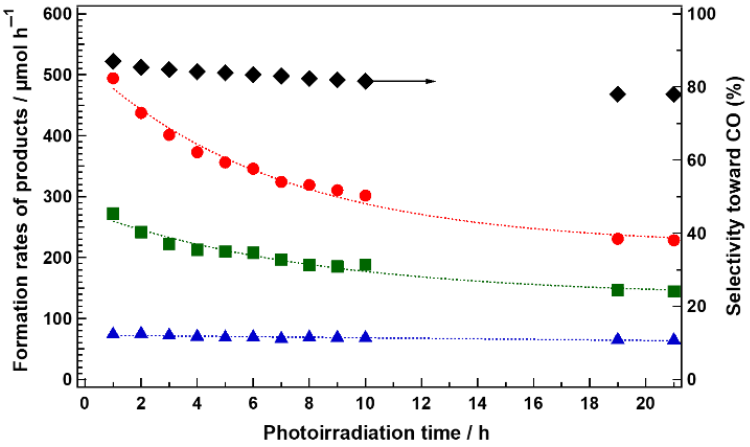

Figure 1 Time course of the formation rates of H_2 (blue triangles), O_2 (green squares), CO (red circles), and selectivity toward CO (black diamonds) evolution for the photocatalytic conversion of CO_2 in H_2O over Ag@Cr/Ga_2O_3. The theoretical loading amounts of both Ag and Cr are 1.0 mol% (molar ratio to Ga).

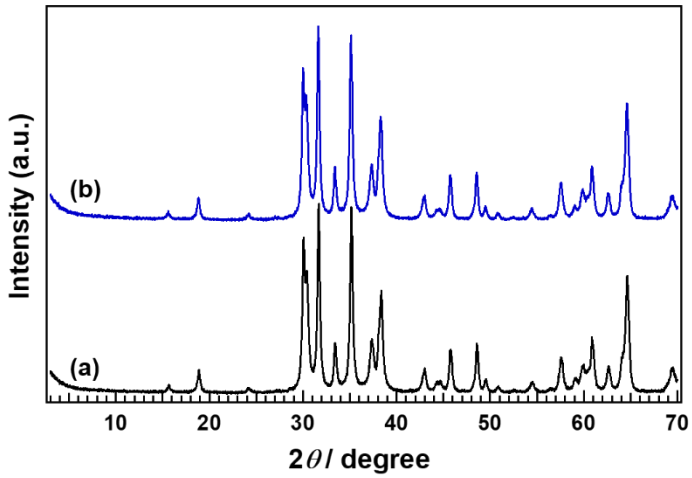

Figure 2 XRD patterns of Ag@Cr/Ga_2O_3 samples: (a) as prepared; (b) after photoirradiation for 5 h.

The XRD patterns of Ag@Cr/Ga_2O_3 before and after photocatalytic reaction for 5 h showed no obvious change (Figure 5), which indicates that the Ga_2O_3 photocatalyst is stable during the photocatalytic conversion of CO_2. We have already reported that the modification of Ga_2O_3 with Cr species resulted in a thin layer of $Cr(OH)_3{\cdot}xH_2O$ on the surface of the Ag co-catalyst, remarkably

enhancing the formation rate and selectivity toward CO evolution as compared to that of Ag/Ga_2O_3.[20] Thus, the decreasing rate of CO formation during photocatalytic conversion of CO_2 is expected to be related to changes to the surface $Cr(OH)_3{\cdot}xH_2O$.

The composition of Ag and Cr loaded on the surface of $Ag@Cr/Ga_2O_3$ with different photoirradiation times was determined by ICP-OES, as shown in Figure 3a. Although 1.0 mol% Ag^+ and 1.0 mol% Cr^{3+} were added during the photodeposition process, 0.86 mol% Ag and 0.81 mol% Cr^{3+} were actually loaded on the surface of Ga_2O_3. The Ag content on $Ag@Cr/Ga_2O_3$ slightly decreased with increasing photoirradiation time from 1 h to 20 h. Conversely, the Cr^{3+} content decreased rapidly to less than half of the original amount within the initial three hours of photoirradiation, ultimately decreasing by nearly three-quarters the original amount within 20 h. Figure 3b shows the dependence of Cr^{3+} in $Ag@Cr/Ga_2O_3$ on the formation rate of CO with different photoirradiation times. The decrease of CO evolved shows a linear dependence on the dissolution rates of Cr^{3+}, which suggests that the decreasing formation rate of CO is mainly due to the dissolution of Cr^{3+} on the surface of $Ag@Cr/Ga_2O_3$.

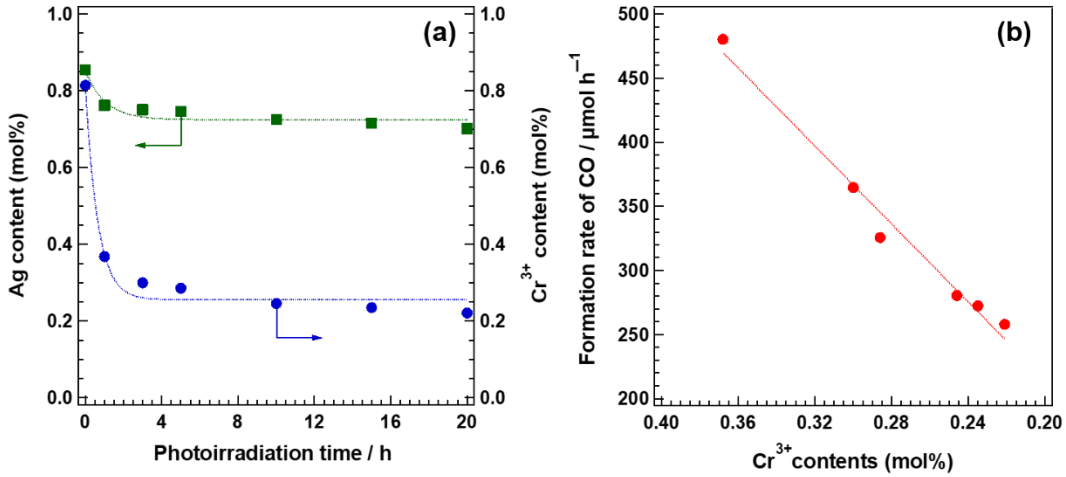

Figure 3 (a) Content of Ag (green square) and Cr^{3+} (blue circle) on the surface of $Ag@Cr/Ga_2O_3$; (b) dependence of Cr^{3+} content in $Ag@Cr/Ga_2O_3$ on the formation rate of CO.

Figure 4 shows the TEM images of the thickness of the $Cr(OH)_3{\cdot}xH_2O$ shell on $Ag@Cr/Ga_2O_3$ after different photoirradiation times (i.e., 0, 5, 10, and 20 h). The thickness of the $Cr(OH)_3{\cdot}xH_2O$ shell decreased from 4.8 nm to 2.0 nm when the photoirradiation time increased from 0 h to 20 h. This

suggests that the dissolution of Cr^{3+} in Ag@Cr/Ga_2O_3 directly leads to a decrease in the thickness of the $Cr(OH)_3 \cdot xH_2O$ shell. In our previous work, I have confirmed that the thin $Cr(OH)_3 \cdot xH_2O$ layer on the Ag co-catalyst surface easily transformed to $Cr(OH)_x(CO_3)_y$ during photocatalytic conversion of CO_2 in an aqueous $NaHCO_3$ solution.[20] The formation of $Cr(OH)_x \cdot (CO_3)_y$ increases the concentration of carbon species on the surface of the Ag active site, which is beneficial for the formation of CO and suppression of H_2. However, the dissolution of Cr^{3+} led to a decrease in the thickness of the $Cr(OH)_3 \cdot xH_2O$ layer with increasing photoirradiation time, undoubtedly influencing the adsorption of CO_2, and therefore, the formation rate of CO decreased.

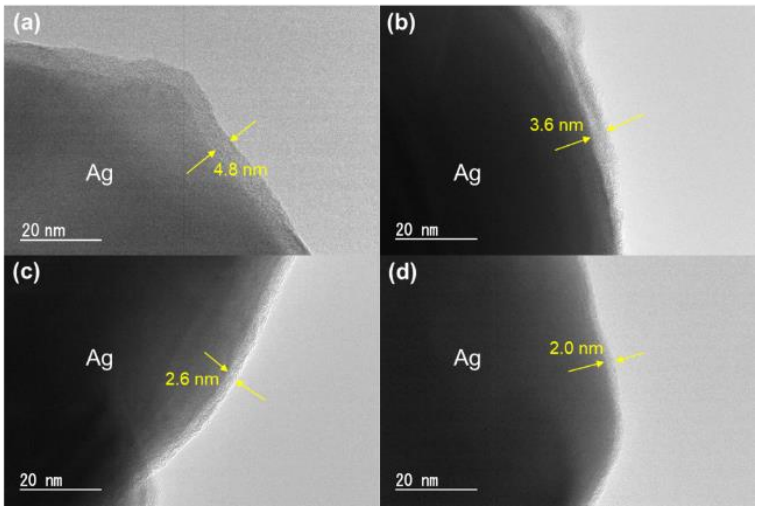

Figure 4 TEM images of the thickness of $Cr(OH)_3 \cdot xH_2O$ shell on Ag@Cr/Ga_2O_3 after different photoirradiation times: (a) 0 h; (b) 5 h; (c) 10 h; (d) 20 h.

Because Cr^{3+} can be oxidized to Cr^{6+} by some strong oxidants, the Cr^{6+} content in the solutions was analyzed at different photoirradiation times by a spectrophotometric standard addition method using 1,5-diphenylcarbazide (DPC). The colorless solution after photoirradiation for 1 h turned pink in an acidic DPC solution, indicating the presence of Cr^{6+} (Figure 5 insert). An intense absorption peak around 543 nm was observed in the UV-Vis absorption spectra (Figure 5), which is assigned to the formation of a DPC-Cr^{6+} complex.[30, 31] The Cr^{6+} content in the solutions with different photoirradiation times was estimated using the absorbance at 543 nm. The amount of Cr^{6+} dissolved in solution increased exponentially, while the amount of Cr^{3+} on the Ag@Cr/Ga_2O_3 surface estimated by ICP-OES decreased exponentially when the photoirradiation time increased from 1 h to 20 h as shown in Figure

5. I calculated the total amount of Cr^{3+} and Cr^{6+} detected during different photoirradiation times (Figure 5), which was close to the detected amount of Cr^{3+} species loaded on $Ag@Cr/Ga_2O_3$ after photodeposition (0.81 mol%). This suggests that the Cr^{3+} species on the surface of $Ag@Cr/Ga_2O_3$ is oxidized to Cr^{6+} during the photocatalytic conversion of CO_2.

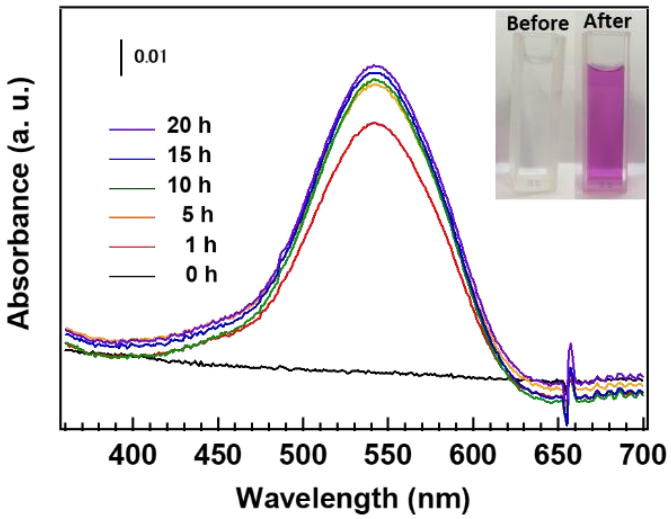

Figure 5 UV−Vis spectra of reacted solutions at different photoirradiation times. The inset picture is of the solutions before photoirradiation (colorless) and after photoirradiation (pink) for 1 h in an acidic DPC solution.

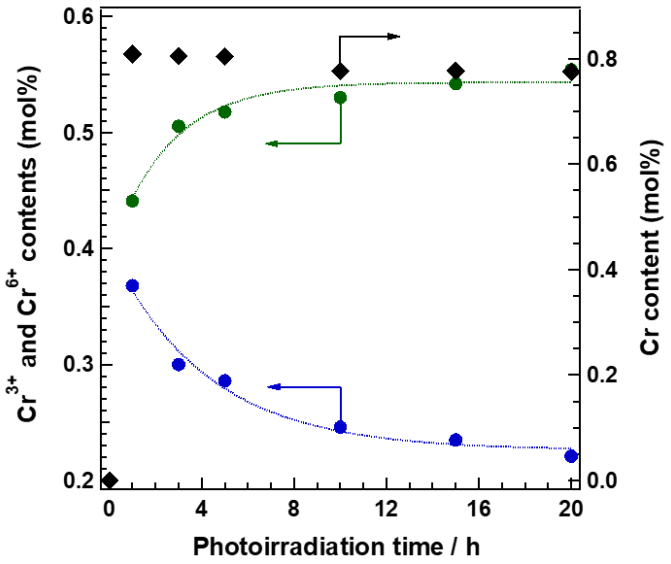

Figure 6 Content of Cr^{3+} in $Ag@Cr/Ga_2O_3$ (blue circle); Cr^{6+} in reaction solution (green circle) estimated by ICP-OES and DPC methods, respectively; and the sum of Cr^{3+} and Cr^{6+} detected (black diamond) with different photoirradiation times.

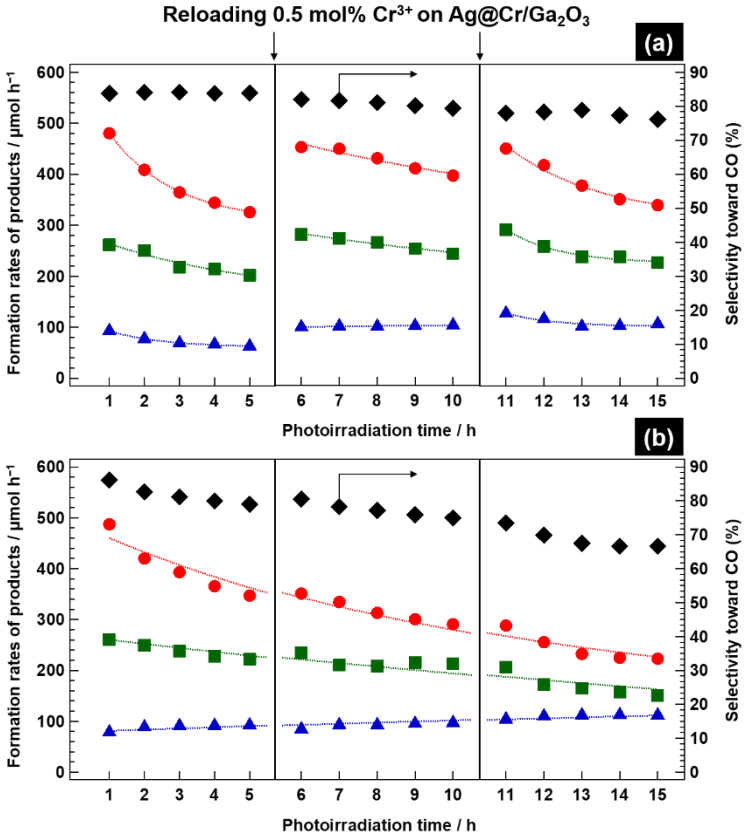

Figure 7 The formation rates of H_2 (blue triangle), O_2 (green square), and CO (red circle), and the selectivity toward CO evolution (black diamond) for the photocatalytic conversion of CO_2 by H_2O over various Ag@Cr/Ga_2O_3: (a) after photoirradiation for 5 h, Ag@Cr/Ga_2O_3 was filtered and dried, and then 0.5 mol% Cr^{3+} was reloaded; this was repeated twice; (b) after photoirradiation for 5 h, Ag@Cr/Ga_2O_3 was filtered and dried, then reused without loading Cr^{3+}.

From Figure 3, it is evident that ~0.5 mol% Cr^{3+} species were oxidized into dissolvable Cr^{6+} in the solution after photoirradiation for 5 h. In order to further verify the effect of Cr^{3+} on the formation rate of CO, Ag@Cr/Ga_2O_3 was filtered and dried after photoirradiation for 5 h, and then 0.5 mol% Cr^{3+} was reloaded on the surface of Ag@Cr/Ga_2O_3 following the photodeposition method.[25] Figure 7a shows the formation rates of H_2, O_2, and CO, and the selectivity toward CO evolution for the photocatalytic conversion of CO_2 by H_2O after reloading Cr^{3+} twice. The formation rate of CO gradually decreased with photoirradiation over 5 h, whereas it significantly increased after reloading 0.5 mol% Cr^{3+} in Ag@Cr/Ga_2O_3. The selectivity toward CO evolution was comparable with that of the previous 5 hours. Even if I repeated this Cr^{3+} reloading process for a second time, it also tended to

be similar to the first reloading, thus decreasing CO activity could be recovered by reloading 0.5 mol% Cr^{3+} in Ag@Cr/Ga_2O_3. During the durability test when Cr was not reloaded, as shown in Figure 7b, the formation rate of CO decreased and formation rate of H_2 increased, which led to a decrease in the selectivity toward CO evolution. This result further confirms that the dissolution of Cr^{3+} on the surface of Ag@Cr/Ga_2O_3 leads to a decrease in the formation rate of CO, however, this loss could be compensated by reloading supplementary Cr^{3+} in Ag@Cr/Ga_2O_3.

Table 1 Formation rates of products, consumed h^+ and the detected Cr^{6+} in reaction solutions under different conditions after photoirradiation for 1 h.

Entry	Experimental condition	Formation rates of products / μmol h^{-1}			Consumed h^+ / μmol h^{-1}	Molar ratio of Cr^{6+} to Ga / mol%
		H_2	O_2	CO		
1	Ag-Cr/Ga_2O_3 + $NaHCO_3$ + CO_2 + O_2 + dark	0.0	0.0	0.0	0.0	0.00
2	Ag-Cr/Ga_2O_3 + $NaHCO_3$ + CO_2 + dark	0.0	0.0	0.0	0.0	0.00
3	Ag-Cr/Ga_2O_3 + $NaHCO_3$ + CO_2 + hv	73.8	272.4	494.3	1089.6	0.44
4	Ag-Cr/Ga_2O_3 + $NaHCO_3$ + Ar + hv	607.3	295.2	3.1	1180.8	0.61
5	Ag-Cr/Ga_2O_3 + H_2O + CO_2 + hv	59.1	32.9	5.9	131.6	0.01
6	Ag-Cr/Ga_2O_3 + H_2O + Ar + hv	119.1	57.6	0.0	230.4	0.02
7	Ag-Cr/Ga_2O_3 + H_2SO_4 + Ar + hv	148.4	68.8	0.0	275.2	0.03
8	[a]Cr^{3+} + $NaHCO_3$ + CO_2 + hv	–	–	–	–	0.64
9	[a]Cr^{3+} + H_2O + Ar + hv	–	–	–	–	0.45
10	Ag/Ga_2O_3 + [b]CrO_4^{2-} + $NaHCO_3$ + Ar + hv	–	–	–	–	0.68
11	Ag/Ga_2O_3 + [b]CrO_4^{2-} + H_2O + Ar + hv	–	–	–	–	0.06

[a] The adding amount of $Cr(NO_3)_3$ is 1.0 mol% (molar ratio of Cr to Ga).

[b] The adding amount of K_2CrO_4 is 1.0 mol% (molar ratio of Cr to Ga).

Verbinnen et al. have reported that the leaching of Cr^{6+} from the initial Cr^{3+} was elevated in the

presence of alkali and alkaline earth salts.[27] To investigate the effect of $NaHCO_3$ additives on the oxidation of Cr^{3+} during the photocatalytic conversion of CO_2, we compared the generated amounts of Cr^{6+} under various reaction conditions, as shown in Table 1. From Entries 1 and 2, it can be seen that Cr^{3+} does not convert to Cr^{6+} under dark conditions, whether or not in the presence of O_2. When $NaHCO_3$ was used as an additive, a considerable amount of Cr^{3+} was oxidized to Cr^{6+} under UV light irradiation. Zhang et al. have reported that holes could transfer to Ag species from the semiconductor,[32] and we can see that the generated amount of Cr^{6+} increased with an increase in the amount of consumed h^+ (Entries 3 and 4). It should be noted that although the absence of $NaHCO_3$ resulted in a low consumption rate of h^+, the generated amount of Cr^{6+} in the reaction solution was much lower than that in the presence of $NaHCO_3$ (Entries 5-7). Therefore, we consider that $NaHCO_3$ as an additive has a critical impact on the generation of Cr^{6+} during photocatalytic conversion of CO_2. In fact, Cr^{3+} is easily oxidized to Cr^{6+} under UV light irradiation even without any photocatalyst (Entries 8 and 9). Prof. Maeda's group has used CrO_4^{2-} as the chromium precursor to load Cr_2O_3 on the photocatalyst surface via a photodeposition method.[33-35] This indicates that Cr^{6+} can also be reduced to Cr^{3+} under photoirradiation. To verify this assumption in our system, we added 1.0 mol% (molar ratio of Cr to Ga) of K_2CrO_4 into the suspension of Ag/Ga_2O_3. After photoirradiation for 1 h, only a small amount of Cr^{6+} was detected in solution (Entry 10), which indicates that most of the Cr^{6+} was reduced under UV light irradiation. Nevertheless, the Cr^{6+} species was difficult to reduce and still remained in solution after photoirradiation for 1 h in the presence of $NaHCO_3$. The above results suggest that the presence of $NaHCO_3$ as an additive inhibits the reduction of the generated Cr^{6+}, resulting in a large amount of detected Cr^{6+}.

Conclusion

The formation rate of CO for the photocatalytic conversion of CO_2 over $Ag@Cr/Ga_2O_3$, where H_2O acts as an electron donor, decreased with increasing photoirradiation time. The decrease of CO evolved exhibited strong dependence on the dissolution rate of Cr^{3+}. It was found that the dissolution of Cr^{3+} in $Ag@Cr/Ga_2O_3$ leads to a decrease in the thickness of the $Cr(OH)_3{\cdot}xH_2O$ shell. Cr^{3+} in

Ag@Cr/Ga_2O_3 was oxidized to soluble Cr^{6+} during the photocatalytic conversion of CO_2 in an aqueous $NaHCO_3$ solution under UV light irradiation. The presence of $NaHCO_3$ suppressed the reduction of generated Cr^{6+}, which greatly improved the dissolution of Cr^{3+}. Our study provides meaningful insight into understanding the mechanism of photocatalytic conversion of CO_2 and the corrosion process of Cr-containing photocatalysts.

References

1. C. Dong, C. Lian, S. Hu, Z. Deng, J. Gong, M. Li, H. Liu, M. Xing and J. Zhang, *Nat. Commun.*, 2018, **9**, 1252.
2. J. Ran, M. Jaroniec and S. Z. Qiao, *Adv. Mater.*, 2018, **30**, 1704649.
3. R. Shwom, C. Isenhour, R. C. Jordan, A. M. McCright and J. M. Robinson, *Front. Ecol. Environ.*, 2017, **15**, 377-384.
4. K. Li, B. Peng and T. Peng, *ACS Catalysis*, 2016, **6**, 7485-7527.
5. E. A. Gilmore, *Current Climate Change Reports*, 2017, **3**, 193-199.
6. M. Mikkelsen, M. Jørgensen and F. C. Krebs, *Energy Environ. Sci.*, 2010, **3**, 43-81.
7. M. Halmann, *Nature*, 1978, **275**, 115-116.
8. T. Inoue, A. Fujishima, S. Konishi and K. Honda, *Nature*, 1979, **277**, 637-638.
9. K. Iizuka, T. Wato, Y. Miseki, K. Saito and A. Kudo, *J. Am. Chem. Soc.*, 2011, **133**, 20863-20868.
10. K. Teramura and T. Tanaka, *Phys. Chem. Chem. Phys.*, 2018, **20**, 8423-8431.
11. H. Tong, S. Ouyang, Y. Bi, N. Umezawa, M. Oshikiri and J. Ye, *Adv. Mater.*, 2012, **24**, 229-251.
12. Y. Hao and A. Steinfeld, *Sci. Bull.*, 2017, **62**, 1099-1101.
13. J. L. White, M. F. Baruch, J. E. Pander Iii, Y. Hu, I. C. Fortmeyer, J. E. Park, T. Zhang, K. Liao, J. Gu, Y. Yan, T. W. Shaw, E. Abelev and A. B. Bocarsly, *Chem. Rev.*, 2015, **115**, 12888-12935.
14. M. Cokoja, C. Bruckmeier, B. Rieger, W. A. Herrmann and F. E. Kuehn, *Angew. Chem. Int. Ed.*, 2011, **50**, 8510-8537.
15. S. C. Roy, O. K. Varghese, M. Paulose and C. A. Grimes, *ACS Nano*, 2010, **4**, 1259-1278.
16. R. Pang, K. Teramura, H. Asakura, S. Hosokawa and T. Tanaka, *Appl. Catal. B*, 2017, **218**, 770-778.

17. Z. Wang, K. Teramura, S. Hosokawa and T. Tanaka, *J. Mater. Chem. A*, 2015, **3**, 11313-11319.
18. Z. Huang, K. Teramura, H. Asakura, S. Hosokawa and T. Tanaka, *J. Mater. Chem. A*, 2017, **5**, 19351-19357.
19. Y. Zhao, G. Chen, T. Bian, C. Zhou, G. I. Waterhouse, L. Z. Wu, C. H. Tung, L. J. Smith, D. O'Hare and T. Zhang, *Adv. Mater.*, 2015, **27**, 7824-7831.
20. R. Pang, K. Teramura, H. Tatsumi, H. Asakura, S. Hosokawa and T. Tanaka, *Chem. Commun.*, 2018, **54**, 1053-1056.
21. R. Pang, K. Teramura, H. Asakura, S. Hosokawa and T. Tanaka, *ACS Sustainable Chem. Eng.*, 2019, **7**, 2083-2090.
22. M. Hassan, F. Ahmad and Z. A. El-Fattah, *J. Alloys Compd.*, 2018, **750**, 320-327.
23. F. C. Richard and A. C. Bourg, *Water Res.*, 1991, **25**, 807-816.
24. A. D. Apte, V. Tare and P. Bose, *J. Hazard. Mater.*, 2006, **128**, 164-174.
25. Z. Zhao, J. D. Rush, J. Holcman and B. H. Bielski, *Radiat. Phys. Chem.*, 1995, **45**, 257-263.
26. K. Maeda, K. Teramura, N. Saito, Y. Inoue and K. Domen, *J. Catal.*, 2006, **243**, 303-308.
27. B. Verbinnen, P. Billen, M. Van Coninckxloo and C. Vandecasteele, *Environ. Sci. Technol.*, 2013, **47**, 5858-5863.
28. P. Biedenkopf, M. Bischoff and T. Wochner, *Mater. Corros.*, 2000, **51**, 287-302.
29. A. F. Stam, R. Meij, H. te Winkel, R. J. v. Eijk, F. E. Huggins and G. Brem, *Environ. Sci. Technol.*, 2011, **45**, 2450-2456.
30. J. C. Tayone, *Int. J. Sci. Res.*, 2015, **19**, 426-432.
31. J. C. R. JoZo Carlos de Andrade, Celio Pasquini and N ivaldi Baccan, *Analyst*, 1983, **108**, 621-625.
32. F. Zhang, K. Maeda, T. Takata and K. Domen, *Chem. Commun.*, 2010, **46**, 7313-7315.
33. T. Kanazawa and K. Maeda, *ACS Appl. Mater. Interfaces*, 2016, **8**, 7165-7172.
34. K. Maeda, A. Xiong, T. Yoshinaga, T. Ikeda, N. Sakamoto, T. Hisatomi, M. Takashima, D. Lu, M. Kanehara and T. Setoyama, *Angew. Chem.*, 2010, **122**, 4190-4193.
35. K. Maeda, K. Teramura, D. Lu, N. Saito, Y. Inoue and K. Domen, *J. Phys. Chem. C*, 2007, **111**, 7554-7560.

Chapter 6

Remarkable enhancement of CO evolution by Ca modification technique for photocatalytic conversion of CO_2 by H_2O

Abstract

In this study, I used a Ca modification strategy to synthesize Ga_2O_3-based photocatalysts in order to achieve highly efficient photocatalytic conversion of CO_2 into CO by H_2O. With this strategy, the formation rates of CO and H_2 can be controlled by varying the amount of Ca species on the Ga_2O_3 surface. I found that the formation rate of CO was enhanced while the formation of H_2 was suppressed during photocatalytic conversion of CO_2 by H_2O at low amounts of Ca. In contrast, excessive amounts of Ca reduced the photocatalytic activity and selectivity toward CO evolution due to the large amounts of $CaGa_4O_7$ generated on the Ga_2O_3 surface. The Fourier transform infrared spectra confirmed that CaO was formed on the Ga_2O_3 surface for low amounts of Ca, which enhanced CO_2 adsorption at the Ga_2O_3 surface. The presence of $CaGa_4O_7$ generated on the Ga_2O_3 surface enhanced the total photocatalytic efficiency; however, this photocatalyst only showed photocatalytic activity toward H_2 evolution. By exploiting the high CO_2 adsorption of CaO and the high photocatalytic efficiency of Ga_2O_3_$CaGa_4O_7$, I achieved a very high formation rate of CO (835 μmol h^{-1}) and high selectivity toward CO evolution (94.5%) for the Ag-Cr/CaO/Ga_2O_3_$CaGa_4O_7$ photocatalyst.

Introduction

Carbon dioxide (CO_2) concentrations in the atmosphere have increased dramatically over the past few centuries due to the combustion of carbon-rich fossil fuels such as coal, oil, and natural gas. As a major anthropogenic greenhouse gas, the ever-increasing CO_2 emissions are detrimental to the environment, which will affect global climate and ecosystems.[1] Therefore, there is an critical need to mitigate CO_2 emissions in order to achieve sustainable development. Ever since the pioneering works on photocatalytic conversion of CO_2 into formic acid (HCOOH) and methyl alcohol (CH_3OH) over semiconductors by Halmann and Inoue et al.,[2, 3] the photocatalytic conversion of CO_2 into other valuable feedstocks at ambient temperatures and pressures has attracted considerable attention from the scientific community as a feasible strategy for CO_2 storage and conversion.[4-8]

In general, the photocatalytic conversion of CO_2 using a heterogeneous catalyst consists of three main steps. First, the CO_2 molecules are adsorbed on the photocatalyst surface (Eqn. 1). Second, the photogenerated electrons react with the adsorbed CO_2 species and protons (H^+) to produce hydrocarbon products such as carbon monoxide (CO) (Eqn. 2) and the photogenerated holes are consumed by the oxide species such as additional sacrificing reagents or water (H_2O) (Eqn. 3). Third, the products are desorbed from the photocatalyst surface. As an economic and environmental resource, H_2O is an ideal electron donor and source of H^+ for photocatalytic conversion of CO_2.[7] However, because the redox potential of H/H_2 is more positive than that of CO_2/CO, the generation of H_2 from H^+ (Eqn. 4) is preferable for photocatalytic conversion of CO_2 into CO (Eqn. 2), where H_2O is used as the electron donor.[7, 9] Hence, it is necessary to evaluate the selectivity of the photocatalyst toward H_2 and CO evolutions during photocatalytic conversion of CO_2 by H_2O (Eqn. 5). In addition, it is crucial to obtain the stoichiometric amounts of O_2 (oxidation product), H_2 and/or CO (reduction products) to confirm that the H_2O functions as an electron donor (Eqn. 6).[10]

$$CO_2\,(g) \rightarrow CO_2\,(ad) \quad (1)$$

$$CO_2\,(ad) + 2H^+ + 2e^- \rightarrow CO + H_2O \quad (2)$$

$$2H_2O \rightarrow O_2 + 4H^+ + 4e^- \quad (3)$$

$$2H^+ + 2e^- \rightarrow H_2 \quad (4)$$

$$\text{Selectivity toward CO evolution (\%)} = 100 \times 2\boldsymbol{R}_{\mathbf{CO}}/(2\boldsymbol{R}_{\mathbf{CO}} + 2\boldsymbol{R}_{\mathbf{H2}}) \quad (5)$$

Consumed $e^-/h^+ = (2\boldsymbol{R}_{CO} + 2\boldsymbol{R}_{H2})/4\boldsymbol{R}_{O2}$ (6)

Here, $\boldsymbol{R}_{CO}$ $\boldsymbol{R}_{H2}$, and $\boldsymbol{R}_{O2}$ represent the formation rates of CO, H_2, and O_2, respectively.[10]

To the best of our knowledge, Kudo et al.[11] were the first to report the synthesis of $Ag/BaLa_4Ti_4O_{15}$ photocatalyst, which had higher selectivity toward CO evolution than that toward H_2 evolution and the stoichiometric amount of O_2 evolved as an oxidation product during the photocatalytic conversion of CO_2 by H_2O. Since then, various heterogeneous photocatalysts have been reported for highly selective photocatalytic conversion of CO_2 into CO with H_2O as the electron donor.[12-20] Nevertheless, the photocatalytic efficiency for CO_2 conversion is still rather low because of the high thermodynamic stability of the CO_2 linear molecules. Based on the processes involved in the photocatalytic conversion of CO_2 described previously, it can be deduced that the photocatalytic activity of the photocatalyst for CO_2 conversion can be improved by increasing the CO_2 adsorption, charge separation, and desorption of products.

According to a few published reports,[21-23] the photocatalytic activity and selectivity of the photocatalyst during the conversion of CO_2 into CO by H_2O can be enhanced by modifying its surface using CO_2 adsorbents such as alkaline earth metals (Ca, Sr, and Ba). However, to date, there are no breakthroughs in the photocatalytic efficiency of the photocatalysts synthesized using this approach. Very recently, I proposed an Ag-Cr dual co-catalyst modification strategy, which is a facile approach to enhance the photocatalytic efficiency of photocatalysts during the conversion of CO_2 into CO with H_2O as the electron donor.[24] In this work, I report the remarkable increase in the photocatalytic efficiency of Ga_2O_3-based photocatalysts for CO_2 conversion, where I modified the Ga_2O_3 surface with Ca species and Ag-Cr was used as the co-catalyst. With this approach, I achieved a high formation rate of CO (835 μmol h^{-1}) per 0.5 g of catalyst and high selectivity toward CO evolution (> 94.5%) during photocatalytic conversion of CO_2 by H_2O. I also conducted a systematic investigation on the role of the Ca species in enhancing the photocatalytic efficiency.

Experimental

Preparation of Ag-Cr/Ga_2O_3_Ca

The Ca-modified Ga_2O_3 (Ga_2O_3_Ca) was prepared using an ammonia precipitation method

reported by Sakata et al.[25] In this method, $Ga(NO_3)_3 \cdot nH_2O$ (12.6 g) was dissolved in deionized water or $CaCl_2$-ultrapure water solution (200 mL) at various molar concentrations. Hydroxylation was carried out by dripping the ammonium hydroxide solution until the pH value reached 9.1. The hydroxides obtained were centrifuged and dried overnight. The Ga_2O_3_Ca was obtained by calcining the precursor at 1273 K for 10 h. The Ag-Cr/Ga_2O_3_Ca was synthesized using the photodeposition method reported in our previous work.[24] In this method, the as-prepared Ga_2O_3_Ca powder (1.0 g) was dispersed in ultrapure water (1.0 L) containing the necessary amounts of silver nitrate ($AgNO_3$) and chromium(III) nitrate ($Cr(NO_3)_3$). The suspension was purged with Ar gas and irradiated under a 400 W high-pressure Hg lamp with Ar gas flowing for 1.0 h, followed by filtration and drying at a room temperature of ~298 K. The Ag/Ga and Cr/Ga molar ratios were the same, with a value of 1.0 mol%. Next, the Ga_2O_3 surface was modified with Ca (0.62 mol%) using the impregnation method. In this method, the as-prepared Ga_2O_3 (1.5 g) was homogeneously dispersed in calcium chloride ($CaCl_2$) aqueous solution (20 mL), followed by evaporation at 358 K (to remove water) and calcination in air at 1273 K for 6 h.

Characterization

The as-prepared Ga_2O_3_Ca samples were characterized using the following instruments: X-ray diffractometer (XRD, Model: Multiflex, Rigaku Corporation, Japan) with Cu Kα radiation (λ = 0.154 nm), X-ray photoelectron spectrometer (XPS, Model: ESCA 3400, Shimadzu Corporation, Japan) with Mg Kα radiation, field-emission scanning electron microscope (FESEM, Model: SU-8220, Hitachi High-Technologies Corporation, Japan), and field-emission transmission electron microscope (FETEM, Model: JEM-2100F, JEOL Ltd, Japan). The Brunauer-Emmett-Teller (BET) surface areas of the photocatalyst samples were measured based on their N_2 adsorption isotherms at 77 K using a volumetric gas adsorption measuring instrument (Model: BELSORP-miniII, MicrotracBEL Corp. (formerly BEL Japan, Inc.), Japan). Prior to the measurements, each sample was evacuated at 473 K for 1 h using a sample pretreatment system (Model: BELPREP-vacII, MicrotracBEL Corp. (formerly BEL Japan, Inc.), Japan). Inductively coupled plasma optical emission spectrometer (ICP-OES, Model: iCAP7400, Thermo Fisher Scientific, USA) was used to determine the actual amounts of Ca modified on the Ga_2O_3 surface. The Fourier transform infrared (FTIR) spectra of the adsorbed carbon species were recorded using an FTIR spectrometer (Model: FT/IR-4700, JASCO International Co., Ltd., Japan)

equipped with a mercury-cadmium-tellurium (MCT) detector and cooled by liquid N_2 in transmission mode at 303 K. Each sample (~30 mg) was pressed into a wafer (diameter: 10 mm) and introduced into the instrument in a cylindrical glass cell with calcium fluoride (CaF_2) windows. The wafer was evacuated at 673 K for 30 min before measurements, followed by treatment under ~40 Torr of O_2 for 30 min, and the wafer was subsequently evacuated for 30 min and cooled to 303 K. The data for each FTIR spectrum were obtained from 128 scans with a resolution of 4 cm^{-1}.

Photocatalytic reaction

The photocatalytic reduction of CO_2 was carried out using a flow system with an inner irradiation-type reaction vessel. The synthesized photocatalyst (0.5 g) was dispersed in ultrapure water (1.0 L) containing 0.1 M sodium bicarbonate ($NaHCO_3$). The CO_2 was bubbled into the solution at a flow rate of 30 mL min^{-1}. The suspension was illuminated using a 4000-W high-pressure Hg lamp with a quartz filter and the assembly was connected to a water-cooling system. The amounts of evolved H_2 and O_2 were detected using a thermal conductivity detector-gas chromatography system (TCD-GC, Model: GC-8A, Shimadzu Corporation, Japan) with a 5A molecular sieve (MS 5A) column, where Ar was used as the carrier gas. The amount of evolved CO was analyzed using a flame ionization detector-gas chromatography system (FID-GC, Model: GC-8A, Shimadzu Corporation, Japan) with a methanizer and ShinCarbon ST column, where N_2 was used as the carrier gas. A high-performance liquid chromatograph (HPLC, Model: LC-4000, JASCO, USA) was used to detect the presence of liquid products.

Results and discussion

Material characterization. The actual amounts of Ca species loaded into Ga_2O_3 at different $CaCl_2$ concentrations were measured using the ICP-OES and the results are presented in Table 1. I found that almost all of the Ca species could be loaded into the Ga_2O_3 when the $CaCl_2$ concentration was less than 0.001 mol L^{-1}. However, not all of the Ca species could be loaded into Ga_2O_3 at higher $CaCl_2$ concentrations. It shall be noted that even if I did not add any $CaCl_2$ during the preparation of Ga_2O_3, trace amounts of Ca were detected in Ga_2O_3, which is likely due to Ca impurities present in the

experimental vessels or precursor reagents. Hereinafter, I named the Ca-loaded Ga_2O_3 photocatalysts as Ga_2O_3_Ca_x (x = 0.32, 0.62, 1.1, 1.6, 2.1, 3.3 mol%) based on the Ca/Ga molar ratios measured by the ICP-OES.

Table 1 Comparison between the calculated Ca/Ga molar ratios and those measured by ICP-OES at different $CaCl_2$ concentrations.

$CaCl_2$ concentration (mol L^{-1})	**Ca/Ga molar ratio (mol%) (Calculated)**	**Ca/Ga molar ratio (mol%) (ICP-OES)**
0.0000	0.00	0.056
0.0005	0.31	0.32
0.0010	0.63	0.62
0.0020	1.3	1.1
0.0030	2.0	1.6
0.0050	3.3	2.1
0.0100	6.5	3.3

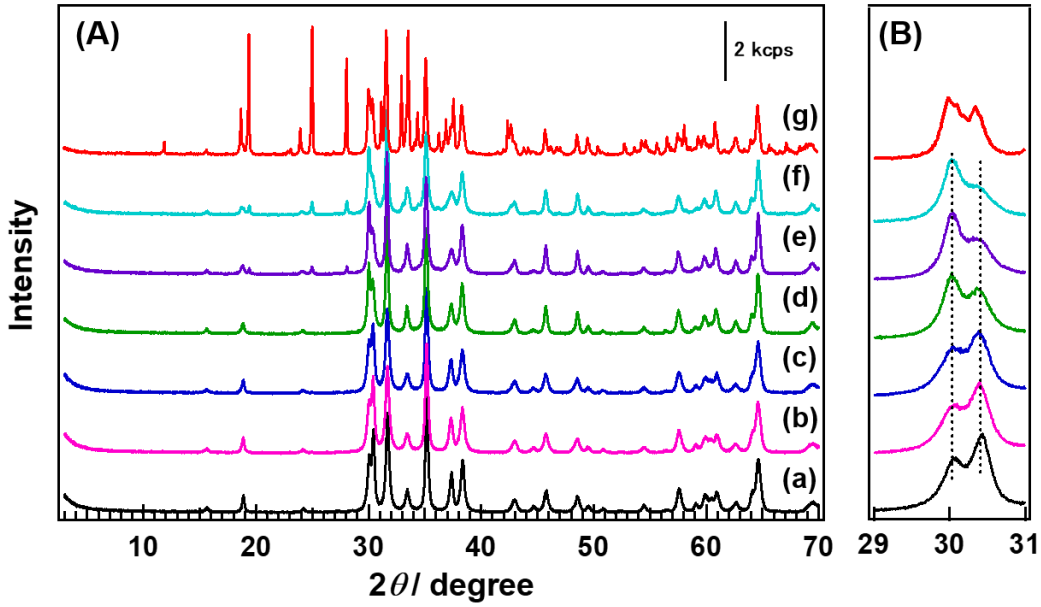

Figure 1 (A) X-ray diffractograms and (B) enlarged X-ray diffractograms at a diffraction angle 2θ of 29–31°C for (a) bare Ga_2O_3, Ga_2O_3_Ca_x with a Ca/Ga molar ratio x of (b) 0.32 mol%, (c) 0.62 mol%, (d) 1.1 mol%, (e) 2.1 mol%, and (f) 3.3 mol%, and (g) $CaGa_4O_7$.

Figure 1A shows the XRD patterns of the bare Ga_2O_3, Ga_2O_3_Ca_*x*, and $CaGa_4O_7$ samples. There were gradual changes in the diffraction peaks assigned to the (020), (311), (400), (002), and (330) facets of $CaGa_4O_7$ (JSPDS01-071-1613) with an increase in the amount of Ca species. In general, a high Ca loading is favorable for the formation of $CaGa_4O_7$. Figure 1B shows the enlarged XRD patterns at a diffraction angle 2θ of 29–31°. I observed that there were no obvious shifts in the diffraction peaks for all Ga_2O_3_Ca_*x* samples compared with those of the bare Ga_2O_3. Because the ionic radius of Ca^{2+} (0.099 nm) is larger than that of Ga^{3+} (0.062 nm), the unshifted peak position in the X-ray diffractograms implies that the Ca^{2+} does not act as a dopant in the bulk Ga_2O_3 lattice. However, there was an obvious increase in the peak intensity at $2\theta = 30.1°$ whereas there was an apparent decrease in the peak intensity at $2\theta = 30.5°$ with an increase in the amount of Ca species, indicating that the amount of Ca plays a role in altering the morphology of Ga_2O_3.

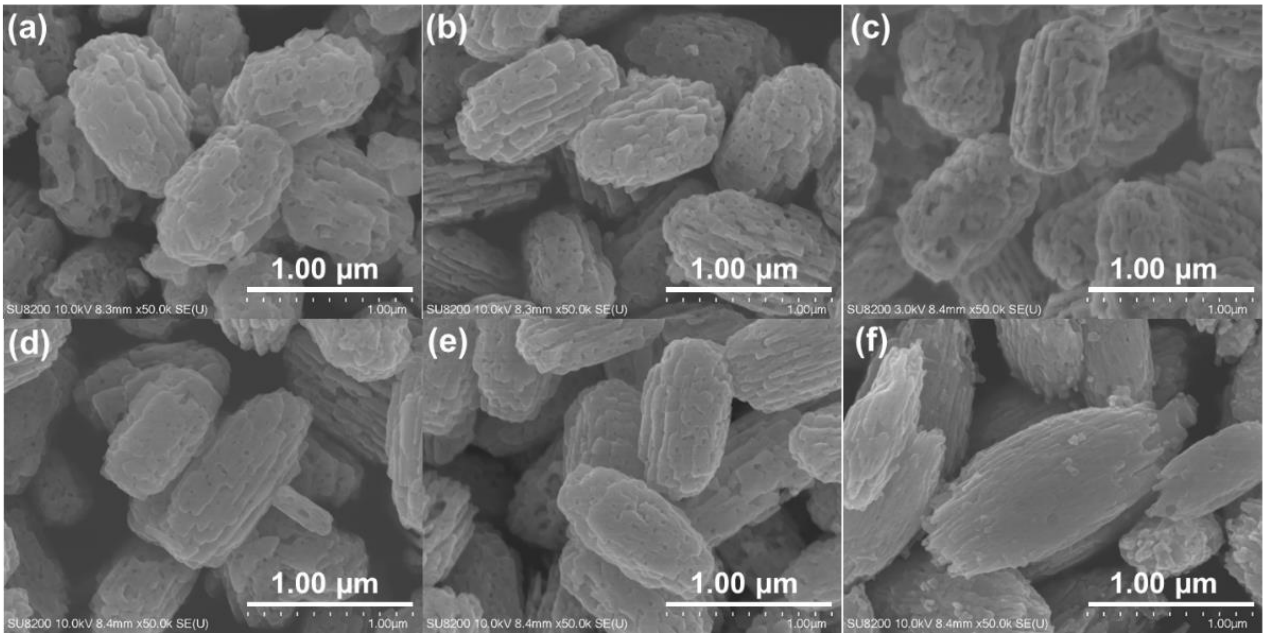

Figure 2 SEM images for (a) bare Ga_2O_3 and Ga_2O_3_Ca_*x* with a Ca/Ga molar ratio *x* of (b) 0.32 mol%, (c) 0.62 mol%, (d) 1.1 mol%, (e) 2.1 mol%, and (f) 3.3 mol%.

I confirmed the morphological changes of the Ga_2O_3 by SEM, as shown in Figure 2. It can be seen that both ends of the Ga_2O_3 nanoparticles were gradually sharpened and the surface of the Ga_2O_3

nanoparticles became smoother as the amount of Ca species increased. The increase in the smoothness of the Ga_2O_3 surface with an increase in the Ca/Ga molar ratio resulted in a decrease in the BET specific surface area of Ga_2O_3_Ca_*x* (Figure 3). This can be attributed to the modification of $CaGa_4O_7$ since I have confirmed from the X-ray diffractograms that the Ca species was not doped into the Ga_2O_3 lattice. I further measured the Ca 2p XPS spectra of the Ga_2O_3_Ca_*x* samples and the results are shown in Figure 4. The increase in the peak intensity of the Ca 2p XPS spectra indicates that the Ca species on the Ga_2O_3 surfaces increased as the amount of Ca increased. In addition, the peak locations in the Ca 2p XPS spectra of the Ga_2O_3_Ca_*x* samples were similar to those of $CaGa_4O_7$. This suggests that a thin $CaGa_4O_7$ layer forms on the Ga_2O_3 surface and the thickness of this thin layer increases with an increase in the amount of Ca.

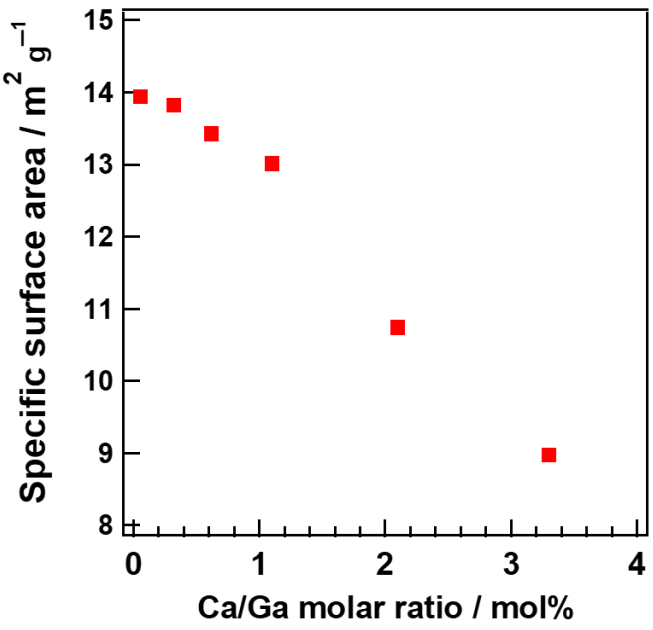

Figure 3 BET specific surface areas for Ga_2O_3_Ca_*x* with a Ca/Ga molar ratio *x* of 0.056, 0.32, 0.62, 1.1, 2.1, and 3.3 mol%.

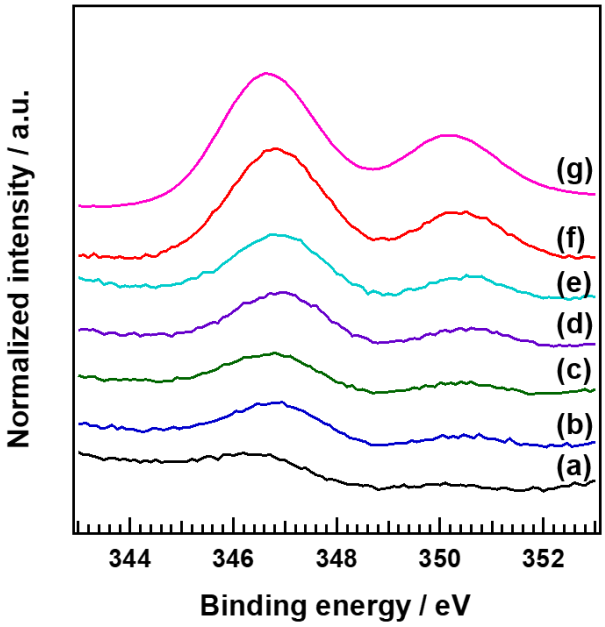

Figure 4 Ca 2p XPS spectra for (a) bare Ga_2O_3, Ga_2O_3_Ca_*x* with a Ca/Ga molar ratio *x* of (b) 0.62 mol%, (c) 1.1 mol%, (d) 2.1 mol%, and (e) 3.3 mol%, (f) $CaGa_4O_7$, and (g) CaO.

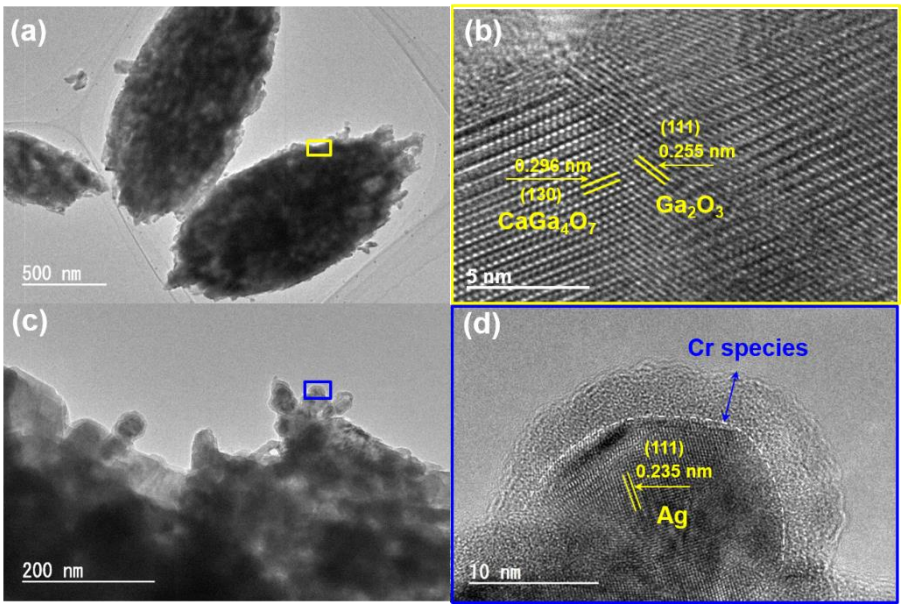

Figure 5 TEM images for (a) Ga_2O_3_Ca_3.3 and (c) Ag-Cr/Ga_2O_3_Ca_3.3. HRTEM images for (b) Ga_2O_3_Ca_3.3 and (d) Ag-Cr/Ga_2O_3_Ca_3.3. It shall be noted that (b) and (d) represent the enlarged TEM images of the marked areas in (a) and (c), indicated by the yellow and blue boxes, respectively.

The close linkage between the $CaGa_4O_7$ and Ga_2O_3 was further confirmed from the TEM and high-resolution TEM (HRTEM) images (Figures 5a and 5b). The marked lattice spaces of 0.296 and 0.255 nm in Figure 5b correspond to the (130) and (111) planes of $CaGa_4O_7$ and Ga_2O_3, respectively. Ag-Cr co-catalyst with a core-shell structure was successfully loaded onto the Ga_2O_3_Ca surface using the photodeposition method (Figures 5c and 5d), which is consistent with the results of our previous work.[24]

Photocatalytic conversion of CO_2. Figure 6 shows the formation rates of CO, H_2, and O_2, as well as the selectivity toward CO evolution for the Ag-Cr/Ga_2O_3, Ag-Cr/Ga_2O_3_Ga_*x,* and Ag-Cr/$CaGa_4O_7$ photocatalysts during the photocatalytic conversion of CO_2 by H_2O. In these photocatalytic systems, no liquid products were detected in the reaction solutions, and H_2, O_2, and CO were detected as gaseous products during the photocatalytic reactions. Stoichiometric amounts of H_2 and CO (reduction products) and O_2 (oxidation product) were obtained, indicating that H_2O serves as the electron donor. The amount of Ca species was found had a significant effect on the formation rates of H_2 and CO. The formation rate of CO increased when the Ca/Ga molar ratio was increased from 0.0 mol% to 1.1 mol% whereas it decreased when the Ca/Ga molar ratio was increased from 1.6 mol% to 3.3 mol% (Figures 6a–6g). In contrast, the formation rate of H_2 of the Ag-Cr/Ga_2O_3_Ca_*x* samples increased monotonically with an increase in the amount of Ca species. The Ag-Cr/$CaGa_4O_7$ photocatalyst only showed activity for the H_2 evolution derived from water splitting (Figure 6h). It is apparent that the formation rates of H_2 were lower for the Ag-Cr/Ga_2O_3_Ca_*x* photocatalysts with lower Ca/Ga molar ratios compared to that for Ag-Cr/Ga_2O_3 during the photocatalytic conversion of CO_2. I observed that the Ag-Cr/Ga_2O_3_Ga_1.1 photocatalyst had the highest formation rate of CO (794 μmol h^{-1}) and the selectivity toward CO evolution was more than 82%.

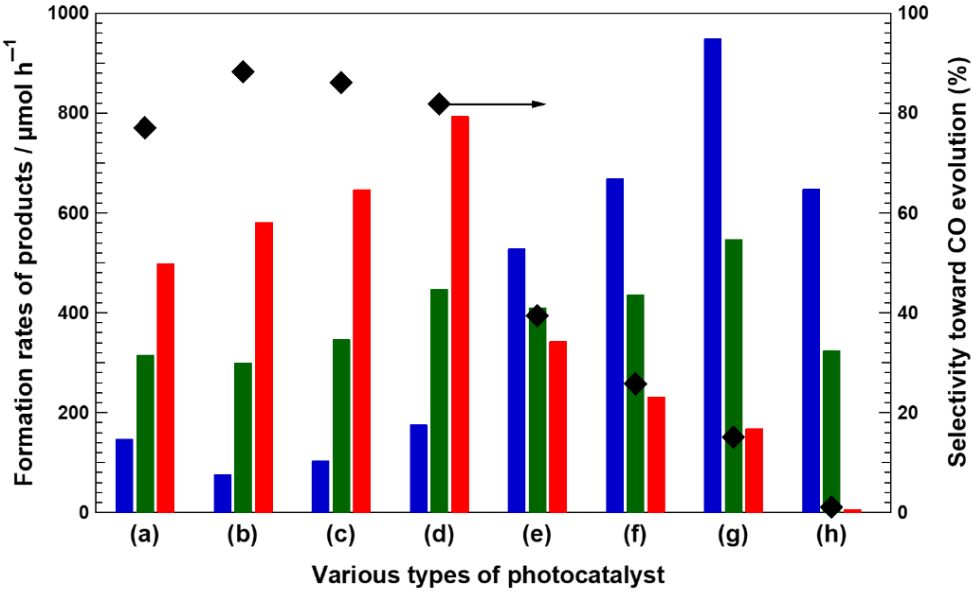

Figure 6 Formation rates of H_2 (blue bars), O_2 (green bars), and CO (red bars) and selectivity toward CO evolution (black diamonds) for the (a) Ag-Cr/Ga_2O_3, Ag-Cr/Ga_2O_3_Ca_*x* with a Ca/Ga molar ratio *x* of (b) 0.32 mol%, (c) 0.62 mol%, (d) 1.1 mol%, (e) 1.6 mol%, (f) 2.1 mol%, and (g) 3.3 mol%, and (h) Ag-Cr/$CaGa_4O_7$ during the photocatalytic conversion of CO_2 by H_2O. Amount of photocatalyst: 0.5 g; Volume of reaction solution (H_2O): 1.0 L; Additive: 0.1 M $NaHCO_3$; CO_2 flow rate: 30 mL min^{-1}; Light source: 400 W high-pressure Hg lamp.

Various controlled experiments were carried out to confirm the source of CO_2 during the photocatalytic conversion of CO_2 by H_2O and the results are shown in Figure 7. There were no appreciable amounts of products detected in dark conditions or in the absence of a photocatalyst. In addition, H_2 was the main product formed when Ar gas was used instead of CO_2 or in the absence of $NaHCO_3$. The results obtained from the controlled experiments confirmed that the evolved CO originated from the gaseous CO_2 introduced to the samples and not from carbon contaminants.

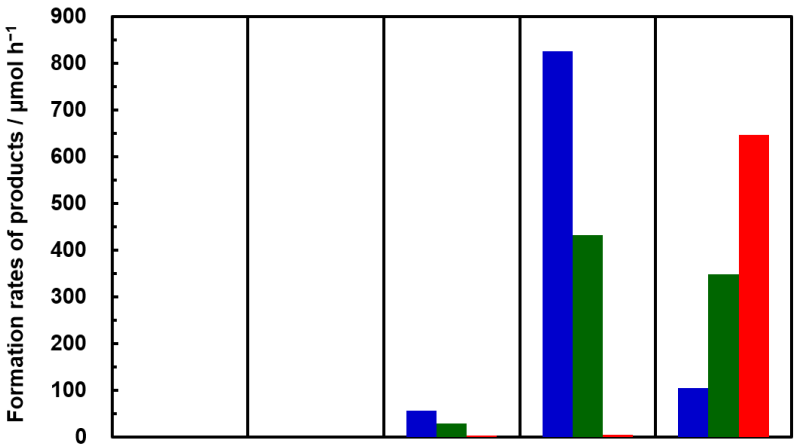

	1	2	3	4	5
Light	×	○	○	○	○
Photocatalyst	○	×	○	○	○
$NaHCO_3$	○	○	×	○	○
CO_2	○	○	○	×	○
all	○	○	○	○	○

Figure 7 Formation rates of H_2 (blue bars), O_2 (green bars), and CO (red bars) for the Ag-Cr/Ga_2O_3_Ca_0.62 photocatalyst during photocatalytic conversion of CO_2. The data markers ○ and × indicate the presence and absence of each component, respectively. Amount of photocatalyst: 0.5 g; Volume of reaction solution (H_2O): 1.0 L; Additive: 0.1 M $NaHCO_3$; CO_2 flow rate: 30 mL min^{-1}; Light source: 400 W high-pressure Hg lamp.

Based on the XRD results (Figure 1) and SEM images (Figure 2), the increase in the amount of Ca species led to changes in the Ga_2O_3 structure for the Ca-modified Ga_2O_3 synthesized using the ammonia precipitation method. To confirm that the improvement in the photocatalytic conversion of CO_2 by H_2O is due to modification of the Ga_2O_3 surface by the Ca species, I modified the Ga_2O_3 surface with 0.62 mol% of Ca using the impregnation method. This method ensures that the structure of Ga_2O_3_Ca is the same as that of bare Ga_2O_3. Figure 8 shows the formation rates of H_2, O_2, and CO during the photocatalytic conversion of CO_2 by H_2O for the Ag-Cr/Ga_2O_3_Ca_0.62 photocatalysts prepared by the ammonia precipitation and impregnation method. The formation rate of CO and selectivity toward CO evolution for the Ag-Cr/Ga_2O_3_Ca_0.62 photocatalyst prepared by the impregnation method were similar to those for the Ag-Cr/Ga_2O_3_Ca_0.62 prepared by the ammonia precipitation method. The results confirmed that the modification of the Ga_2O_3 surface with Ca species contributes to the improved CO evolution during photocatalytic conversion of CO_2 by H_2O. However,

the formation rate of CO will decrease and H_2 will become the main product if excessive amounts of Ca are loaded onto the photocatalyst surface.

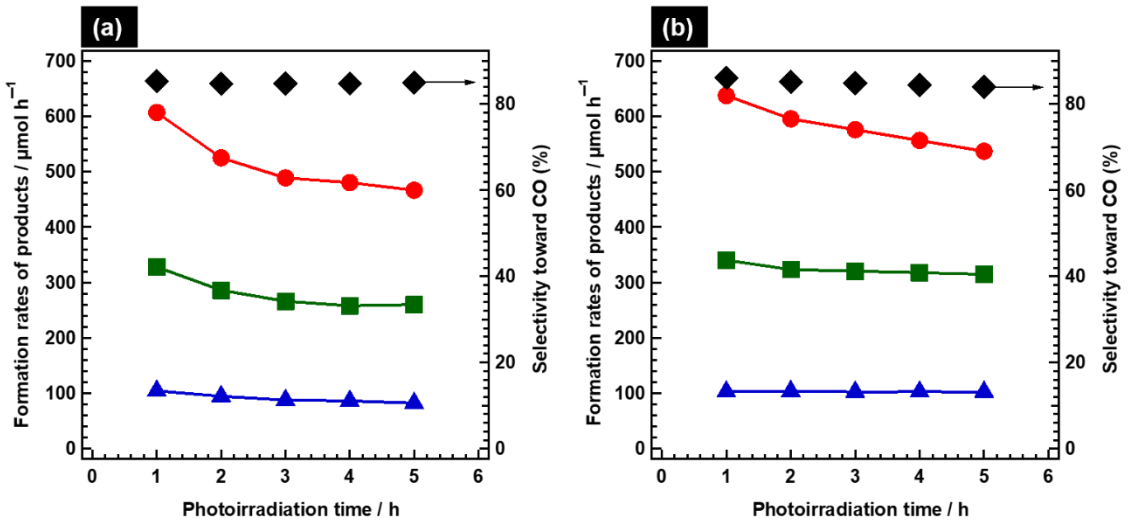

Figure 8 Formation rates of CO (red circles), O_2 (green squares), H_2 (blue triangles) evolutions, and selectivity toward CO evolution (black diamonds) over Ag-Cr/Ga_2O_3_Ca_0.62 prepared using (a) ammonia precipitation and (b) impregnation method. Photocatalyst amount: 0.5 g, reaction solution volume: H_2O (1.0 L), additive: 0.1 M $NaHCO_3$, CO_2 flow rate: 30 mL min^{-1}, light source: 400 W high-pressure Hg lamp.

Role of the Ca species. To gain a better understanding on the higher formation rate of CO and lower formation rate of H_2 during photocatalytic conversion of CO_2 by H_2O for the Ca modified-Ga_2O_3 with lower Ca/Ga molar ratios compared to those for bare Ga_2O_3, I characterized the samples by FTIR spectroscopy, which is an effective technique to investigate the CO_2 species adsorbed on the surface of a material. Figure 9 shows the FTIR spectra of the CO_2-adsorbed samples after introducing ~0.2 Torr of CO_2. When CO_2 was introduced to the Ga_2O_3 sample, three absorbance peaks were observed at 1634, 1432, and 1225 cm^{-1}, which can be ascribed to asymmetric CO_3 stretching vibrations [$\nu_{as}(CO_3)$], symmetric CO_3 stretching vibrations [$\nu_s(CO_3)$] of monodentate bicarbonate species (m-HCO_3-Ga), and OH deformation vibrations [δ(OH)], respectively.[26-28] The absorbance peaks at 1699 and 1636 cm^{-1} for the CO_2-adsorbed CaO sample can be attributed to bridging carbonate stretching and asymmetric CO_3 stretching vibrations [$\nu_{as}(CO_3)$] of the bicarbonate species, respectively. The

broad structureless absorbance peaks between 1480 and 1318 cm^{-1} can be attributed to symmetric and asymmetric CO_3 stretching of unidentate carbonate, as well as symmetric CO_3 stretching [$\nu_s(CO_3)$] of bicarbonate.[29-33] When the Ga_2O_3 surface was modified with a small amount of Ca species, absorbance peaks were observed at 1225, 1433, and 1633 cm^{-1}, which can be attributed to the adsorption of CO_2 on Ga_2O_3. In addition, absorbance peaks were observed at 1320, 1408, 1589, and 1694 cm^{-1}, which can be attributed to the adsorption of CO_2 on CaO and $CaGa_4O_7$ after CO_2 was introduced to the Ga_2O_3_Ca_0.62 sample. Based on the Ca 2p XPS spectra (Figure 4), I confirmed that $CaGa_4O_7$ was present on the Ga_2O_3 surface. The results also indicated that CaO was generated on the Ga_2O_3 surface modified with low amounts of Ca species. However, when the Ga_2O_3 surface was modified with high amounts of Ca species, the absorbance peaks attributed to CO_2 adsorption on Ga_2O_3 were very low and mainly broad absorbance peaks at 1630 and 1325 cm^{-1} were observed, which were derived from the adsorption of CO_2 on $CaGa_4O_7$.

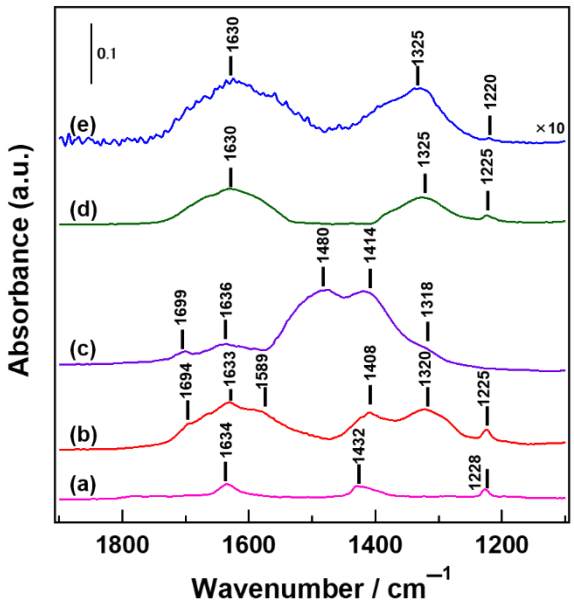

Figure 9 FTIR spectra of the CO_2-adsorbed (a) Ga_2O_3, (b) Ga_2O_3_Ca_0.62, (c) CaO, (d) Ga_2O_3_Ca_3.3, and (e) $CaGa_4O_7$ after introducing ~0.2 Torr of CO_2.

Figure 10 shows the FTIR spectra of the CO_2-adsorbed Ga_2O_3, Ga_2O_3_Ca_0.62, Ga_2O_3_Ca_3.3, and $CaGa_4O_7$ samples after introducing the same amount of CO_2 within a range of 0.1–40.0 Torr. The CO_2 adsorption on the Ga_2O_3_Ca_0.62 surface was significantly higher than that on the Ga_2O_3 surface

due to the adsorption of CO_2 at both Ga and Ca sites. However, the $CaGa_4O_7$ surface was not conducive for CO_2 adsorption and therefore, the CO_2 adsorption on the Ga_2O_3_Ca_3.3 surface was lower than that on the Ga_2O_3_Ca_0.62 surface, as indicated by the OH deformation vibration band [δ(OH)] at 1225 cm^{-1}. which is known to be an intermediate species for photocatalytic conversion of CO_2 by H_2O.[34] Because the photocatalytic conversion of H^+ into H_2 and conversion of CO_2 into CO are two competing processes in an aqueous solution, the low adsorption of CO_2 at the base site leads to low photocatalytic activity and selectivity toward CO evolution during photocatalytic conversion of CO_2 by H_2O. Consequently, the $CaGa_4O_7$-covered Ga_2O_3 showed high selectivity toward H_2 evolution as well as a very low formation rate of CO during photocatalytic conversion of CO_2 into CO. In addition, the high photocatalytic efficiency of CO_2 conversion for the Ga_2O_3_Ca_0.62 photocatalyst is likely due to the high adsorption of CO_2 at the base site of Ga_2O_3_Ca_0.62.

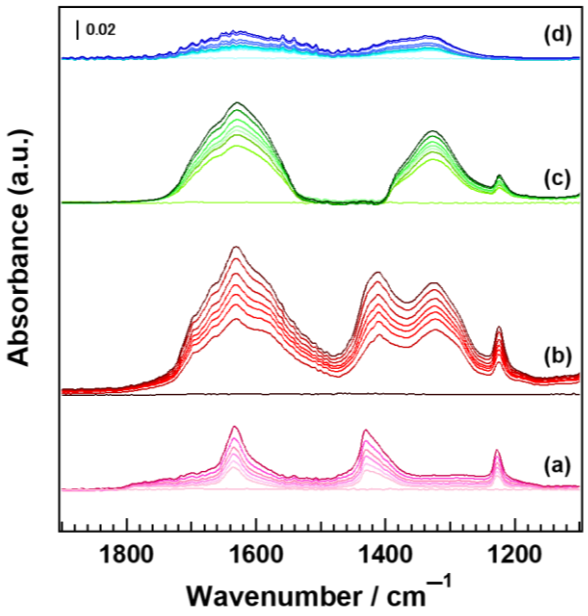

Figure 10 FTIR spectra for the CO_2-adsorbed (a) Ga_2O_3, (b) Ga_2O_3_Ca_0.62, (c) Ga_2O_3_Ca_3.3, and (d) $CaGa_4O_7$ samples after introducing the same amount of CO_2 within a range of 0.1–40.0 Torr.

The photocatalytic efficiency of various Ag-Cr/CaO/Ga_2O_3 photocatalysts was investigated in order to demonstrate that the presence of CaO on the Ga_2O_3 surface provides a conducive environment to enhance the photocatalytic activity and selectivity during the photocatalytic conversion of CO_2 into

CO. Figure 11 shows the formation rates of H_2, O_2, and CO as well as the selectivity toward CO evolution for various photocatalysts during photocatalytic conversion of CO_2. I found that the Ga_2O_3_Ca_1.1 photocatalyst (with a low amount of CaO generated on the Ga_2O_3 surface) significantly enhanced the formation rate of CO during the photocatalytic conversion of CO_2 by H_2O compared with the bare Ga_2O_3 (Figures 11a and 11b). However, when 1.1 mol% of CaO was physically loaded on the Ga_2O_3 by grinding (1.1mol%CaO/Ga_2O_3) and then the Ag-Cr co-catalyst was loaded onto the CaO/Ga_2O_3 surface, there were no significant changes in the formation rate of CO and selectivity toward CO evolution compared with those for the bare Ga_2O_3 (Figures 11c and 11b). Because CaO-loaded Ga_2O_3 without calcination can easily dissolve in H_2O, I increased the CaO loading on the Ga_2O_3 surface to 70 mol% and observed that there was an increase in the formation rate of CO and there was a decrease in the formation of H_2 for the Ag-Cr/70mol%CaO/Ga_2O_3 photocatalyst obtained using the same grinding method (Figure 11d). However, when I mixed 70 mol% of CaO with the prepared Ag-Cr/Ga_2O_3, I observed that there was no improvement in the photocatalytic activity and selectivity during the conversion of CO_2 into CO by H_2O regardless if I mixed them by grinding (Figure 11e) or if I mixed them directly in the reaction solution (Figure 11f). This indicates that the addition of CaO onto the Ga_2O_3 surface enhances the formation rate of CO and suppresses the formation of H_2 during the photocatalytic conversion of CO_2 by H_2O. In addition, the tight junction between the Ga_2O_3, CaO, and Ag-Cr co-catalyst is crucial to improve the photocatalytic activity and selectivity of the photocatalyst for the conversion of CO_2 into CO.

In my previous work,[24] I had confirmed that Ag works as an active site while the chromium hydroxide layer outside the Ag core increases the CO_2 adsorption.[35] Thus, the Ag-Cr co-catalyst should be loaded at the interface of CaO and Ga_2O_3, which will facilitate the adsorbed CO_2 species on the CaO to contact with the Ag active site, and further lead to high photocatalytic activity and selectivity during the photocatalytic conversion of CO_2 into CO. It shall be noted that even though the formation rate of CO was enhanced for the Ag-Cr/70mol%CaO/Ga_2O_3 photocatalyst compared with that for the Ag-Cr/Ga_2O_3 photocatalyst, the formation rate of CO was still significantly lower than that for the Ag-Cr/Ga_2O_3_Ca_1.1 photocatalyst. Because $CaGa_4O_7$ can form easily after calcination of CaO and Ga_2O_3 at high temperatures, both $CaGa_4O_7$ and CaO were generated on the Ga_2O_3_Ca_1.1 surface, as shown in the X-ray diffractograms (Figure 1), Ca 2p XPS spectra (Figure 4), and FTIR spectra (Figure 10). I

believe that the high photocatalytic efficiency for the Ag-Cr/Ga_2O_3_Ca_1.1 photocatalyst during the conversion of CO_2 is not only due to the high CO_2 adsorption at the CaO site, but also due to the presence of $CaGa_4O_7$.

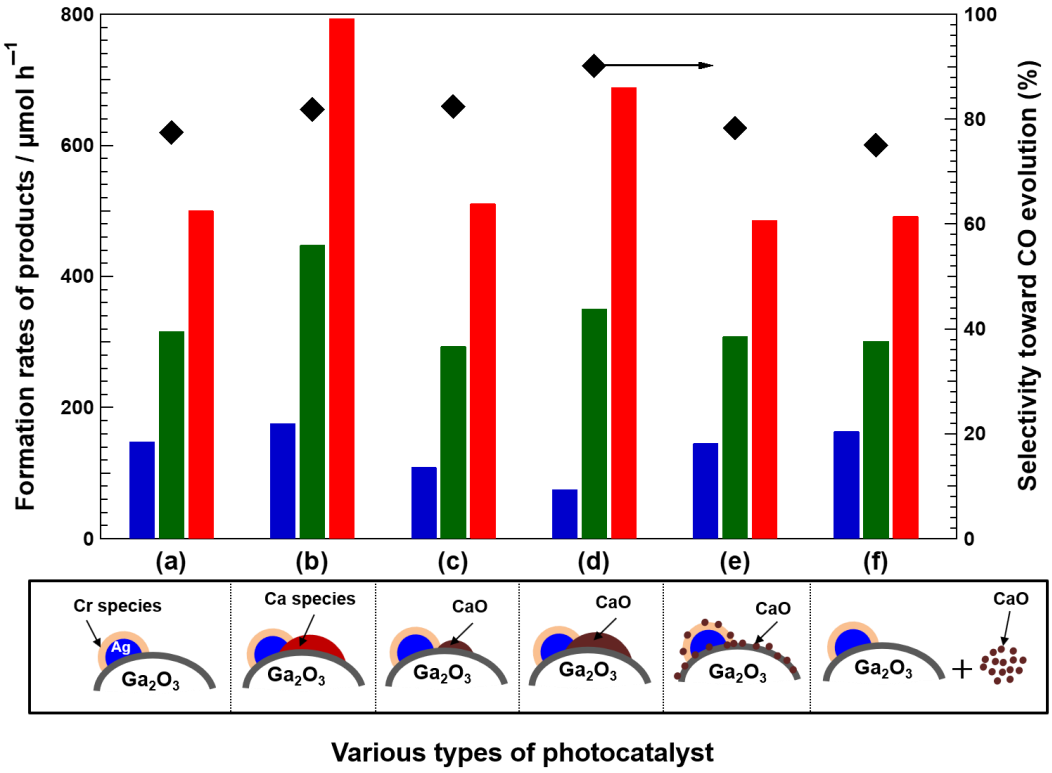

Figure 11 Formation rates of H_2 (blue bars), O_2 (green bars), and CO (red bars), as well as selectivity toward CO evolution (black diamonds) for various photocatalysts: (a) Ga_2O_3, (b) Ga_2O_3_Ca_1.1, (c) Ga_2O_3 physically mixed with 1.1 mol% of CaO (with grinding), (d) Ga_2O_3 physically mixed with 70 mol% of CaO (with grinding), (e) Ag-Cr/Ga_2O_3 physically mixed with 70 mol% of CaO (with grinding), (f) Ga_2O_3 physically mixed with 70 mol% of CaO (without grinding) before being added into the reaction solution. Schematics of various types of photocatalysts are shown in (a)–(f). The photocatalysts in (a)–(e) were loaded with Ag-Cr co-catalyst. Amount of photocatalyst: 0.5 g; Volume of reaction solution (H_2O): 1.0 L; Additive: 0.1 M $NaHCO_3$; CO_2 flow rate: 30 mL min^{-1}; Light source: 400 W high-pressure Hg lamp.

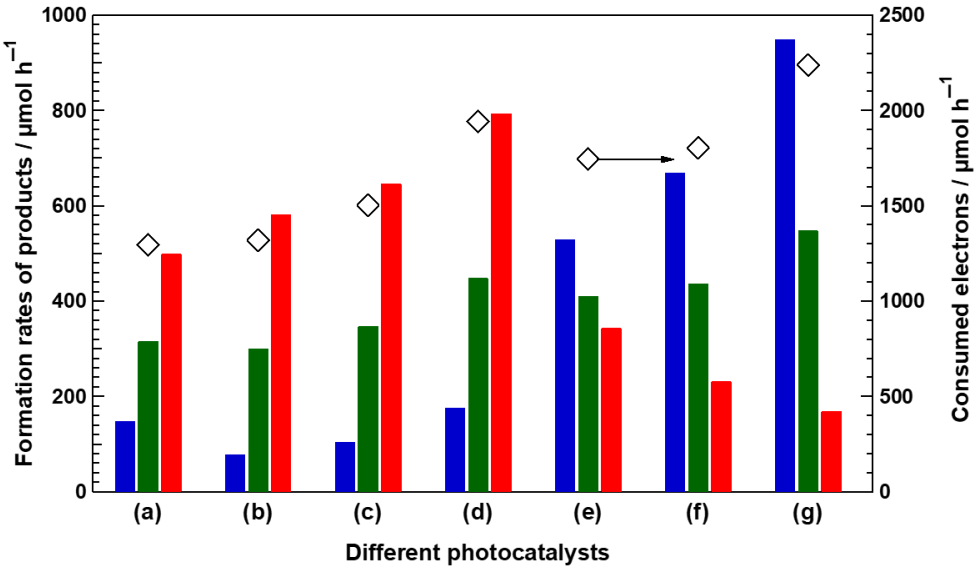

Figure 12 Formation rates of H_2 (blue bars), O_2 (green bars), and CO (red bars), as well as the consumed electrons (open diamonds) for (a) Ag-Cr/Ga_2O_3, Ag-Cr/Ga_2O_3_Ca_*x* with a Ca/Ga molar ratio *x* of (b) 0.32 mol%, (c) 0.62 mol%, (d) 1.1 mol%, (e) 1.6 mol%, (f) 2.1 mol%, and (g) 3.3 mol%, and (h) Ag-Cr/$CaGa_4O_7$ during photocatalytic conversion of CO_2 by H_2O. Amount of photocatalyst: 0.5 g; Volume of reaction solution (H_2O): 1.0 L; Additive: 0.1 M $NaHCO_3$; CO_2 flow rate: 30 mL min^{-1}; Light source: 400 W high-pressure Hg lamp.

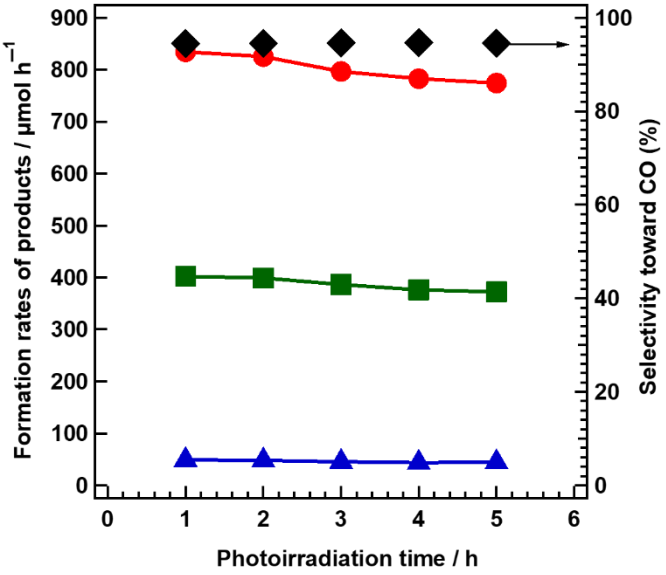

Figure 13 Formation rates of H_2 (blue triangles), O_2 (green squares), and CO (red circles), and selectivity toward CO evolution (black diamonds) during the photocatalytic conversion of CO_2 by H_2O for the

Ga_2O_3_$CaGa_4O_7$ photocatalyst physically mixed and 70 mol% of CaO with Ag-Cr as the co-catalyst. These results were obtained after photoirradiation for 5 h. Amount of photocatalyst: 0.5 g; Volume of reaction solution (H_2O): 1.0 L; Additive: 0.1 M $NaHCO_3$; CO_2 flow rate: 30 mL min^{-1}; Light source: 400 W high-pressure Hg lamp.

As shown in Figure 12, the total amount of consumed electrons increased with an increase in the amount of $CaGa_4O_7$ on the Ga_2O_3 surface. Moreover, even though the $CaGa_4O_7$ showed high selectivity toward H_2 evolution, the formation rate of H_2 for $CaGa_4O_7$ was significantly lower than that for Ga_2O_3_Ca_3.3 (Ga_2O_3_$CaGa_4O_7$). This indicates that the presence of $CaGa_4O_7$ on the Ga_2O_3 surface enhances the overall photocatalytic efficiency during CO_2 conversion and water splitting. I expect that by exploiting the high CO_2 adsorption of CaO and the high photocatalytic efficiency of Ga_2O_3_$CaGa_4O_7$, the photocatalytic activity and selectivity of the photocatalyst can be further improved to maximize the conversion of CO_2 into CO by H_2O. Figure 13 shows the formation rates of H_2, O_2, and CO during the photocatalytic conversion of CO_2 by H_2O for the Ga_2O_3_$CaGa_4O_7$ photocatalyst physically mixed with 70 mol% of CaO with Ag-Cr as the co-catalyst. I achieved a very high formation rate of CO (835 μmol h^{-1}) and the selectivity toward CO evolution was more than 94.5%. This confirms that the modification of the Ga_2O_3 surface by the CaO and $CaGa_4O_7$ can significantly enhance the formation rate of CO and selectivity toward CO evolution during photocatalytic conversion of CO_2 by H_2O because of the high CO_2 adsorption of CaO and the high photocatalytic efficiency of Ga_2O_3_$CaGa_4O_7$.

Conclusions

In this work, I used a facile Ca modification strategy to synthesize Ga_2O_3-based photocatalysts in order to achieve highly efficient photocatalytic conversion of CO_2 into CO by H_2O. When the Ga_2O_3 surface was modified with a small amount of Ca, both CaO and $CaGa_4O_7$ formed on the Ga_2O_3 surface, which improved the photocatalytic activity and selectivity for the conversion of CO_2 into CO by H_2O. However, excessive amounts of Ca resulted in the formation of $CaGa_4O_7$ on the Ga_2O_3 surface, which decreased the formation rate of CO and selectivity toward CO evolution because $CaGa_4O_7$ only showed

activity for water splitting. The highest formation rate of CO (794 μmol h^{-1}) was achieved for the Ag-Cr/Ga_2O_3_Ga_1.1 with a selectivity toward CO evolution of more than 82% during photocatalytic conversion of CO_2 by H_2O. I physically mixed Ga_2O_3_$CaGa_4O_7$ with CaO and Ag-Cr co-catalyst to exploit the high CO_2 adsorption of CaO and high photocatalytic efficiency of Ga_2O_3_$CaGa_4O_7$ and indeed, a very high formation rate of CO (835 μmol h^{-1}) and selectivity toward CO evolution (94.5%) were obtained during photocatalytic conversion of CO_2 by H_2O. I believe that the Ca modification strategy can be used to modify the surface of other photocatalysts in order to achieve a highly efficient photocatalytic conversion of CO_2 by H_2O.

References

1. R. K. Pachauri, M. R. Allen, V. R. Barros, J. Broome, W. Cramer, R. Christ, J. A. Church, L. Clarke, Q. Dahe and P. Dasgupta, *Climate change 2014: synthesis report. Contribution of Working Groups I, II and III to the fifth assessment report of the Intergovernmental Panel on Climate Change*, IPCC, 2014.
2. M. Halmann, *Nature*, 1978, **275**, 115-116.
3. T. Inoue, A. Fujishima, S. Konishi and K. Honda, *Nature*, 1979, **277**, 637-638.
4. K. Li, B. Peng and T. Peng, *ACS Catalysis*, 2016, **6**, 7485-7527.
5. M. Mikkelsen, M. Jørgensen and F. C. Krebs, *Energy Environ. Sci.*, 2010, **3**, 43-81.
6. M. Cokoja, C. Bruckmeier, B. Rieger, W. A. Herrmann and F. E. Kuehn, *Angew. Chem. Int. Ed.*, 2011, **50**, 8510-8537.
7. J. L. White, M. F. Baruch, J. E. Pander Iii, Y. Hu, I. C. Fortmeyer, J. E. Park, T. Zhang, K. Liao, J. Gu, Y. Yan, T. W. Shaw, E. Abelev, and A. B. Bocarsly, *Chem. Rev.*, 2015, **115**, 12888-12935.
8. J. Barber, *Chem. Soc. Rev.*, 2009, **38**, 185-196.
9. P. S. Surdhar, S. P. Mezyk and D. A. Armstrong, *J. Phys. Chem.*, 1989, **93**, 3360-3363.
10. K. Teramura and T. Tanaka, *Phys. Chem. Chem. Phys.*, 2018, **20**, 8423-8431.
11. K. Iizuka, T. Wato, Y. Miseki, K. Saito and A. Kudo, *J. Am. Chem. Soc.*, 2011, **133**, 20863-20868.
12. T. Takayama, A. Iwase and A. Kudo, *Bull. Chem. Soc. Jpn.*, 2015, **88**, 538-543.

13. H. Nakanishi, K. Iizuka, T. Takayama, A. Iwase and A. Kudo, *ChemSusChem*, 2017, **10**, 112-118.
14. H. Yoshida, L. Zhang, M. Sato, T. Morikawa, T. Kajino, T. Sekito, S. Matsumoto and H. Hirata, *Catal. Today*, 2015, **251**, 132-139.
15. A. Anzai, N. Fukuo, A. Yamamoto and H. Yoshida, *Catal. Commun.*, 2017, **100**, 134-138.
16. Z. Wang, K. Teramura, Z. Huang, S. Hosokawa, Y. Sakata and T. Tanaka, *Catal. Sci. Technol.*, 2016, **6**, 1025-1032.
17. K. Teramura, Z. Wang, S. Hosokawa, Y. Sakata and T. Tanaka, *Chem. – Eur. J.*, 2014, **20**, 9906-9909.
18. Z. Wang, K. Teramura, S. Hosokawa and T. Tanaka, *J. Mater. Chem. A*, 2015, **3**, 11313-11319.
19. Z. Huang, K. Teramura, S. Hosokawa and T. Tanaka, *Appl. Catal. B*, 2016, **199**, 272-281.
20. R. Pang, K. Teramura, H. Asakura, S. Hosokawa and T. Tanaka, *Appl. Catal. B*, 2017, **218**, 770-778.
21. K. Teramura, H. Tatsumi, Z. Wang, S. Hosokawa and T. Tanaka, *Bull. Chem. Soc. Jpn.*, 2015, **88**, 431-437.
22. Z. Huang, K. Teramura, H. Asakura, S. Hosokawa and T. Tanaka, *J. Mater. Chem. A*, 2017, **5**, 19351-19357.
23. H. Tatsumi, K. Teramura, Z. Huang, Z. Wang, H. Asakura, S. Hosokawa and T. Tanaka, *Langmuir*, 2017, **33**, 13929-13935.
24. R. Pang, K. Teramura, H. Tatsumi, H. Asakura, S. Hosokawa and T. Tanaka, *Chem. Commun.*, 2018, **54**, 1053-1056.
25. Y. Sakata, T. Hayashi, R. Yasunaga, N. Yanaga and H. Imamura, *Chem. Commun.*, 2015, **51**, 12935-12938.
26. H. Tsuneoka, K. Teramura, T. Shishido and T. Tanaka, *J. Phys. Chem. C*, 2010, **114**, 8892-8898.
27. S. E. Collins, M. A. Baltanás and A. L. Bonivardi, *J. Catal.*, 2004, **226**, 410-421.
28. S. E. Collins, M. A. Baltanás and A. L. Bonivardi, *J. Phys. Chem. B*, 2006, **110**, 5498-5507.
29. Y. Fukuda and K. Tanabe, *Bull. Chem. Soc. Jpn.*, 1973, **46**, 1616-1619.
30. R. Philipp and K. Fujimoto, *J. Phys. Chem.*, 1992, **96**, 9035-9038.
31. G. Busca and V. Lorenzelli, *Mater. Chem.*, 1982, **7**, 89-126.

32. A. Tsyganenko and V. Filimonov, *J. Mol. Struct.*, 1973, **19**, 579-589.

33. G. Busca, J. Lamotte, J. C. Lavalley and V. Lorenzelli, *J. Am. Chem. Soc.*, 1987, **109**, 5197-5202.

34. K. Teramura, K. Hori, Y. Terao, Z. Huang, S. Iguchi, Z. Wang, H. Asakura, S. Hosokawa and T. Tanaka, *J. Phys. Chem. C*, 2017, **121**, 8711-8721.

35. R. Pang, K. Teramura, H. Asakura, S. Hosokawa and T. Tanaka, *ACS Sustainable Chem. Eng.*, 2019, **7**, 2083-2090.

Summary

In this thesis, the author is dedicated to high active and high selective photocatalytic conversion of CO_2 by H_2O over heterogeneous catalysts, such as $SrNb_2O_6$ and Ga_2O_3. It was found that the morphology, bandgap structures, crystal structure, and surface states of catalyst, co-catalysts modified on the catalyst, and additives in the reaction solution show great effect on the photocatalytic activity and selectivity for the conversion of CO_2 by H_2O. The general conclusion of this thesis is as follows:

In chapter 1, well-shaped $SrNb_2O_6$ nanorod and $SrNb_2O_7$ nanoflake were fabricated using a flux method. High selectivity (greater than 95%) toward the photocatalytic evolution of CO over $Ag/SrNb_2O_6$ was observed, while H_2 was the main product over $Ag/SrNb_2O_7$. It was found that the preparation methods of $SrNb_2O_6$, loading method of Ag co-catalyst significantly affected the photocatalytic activity and selectivity for the conversion of CO_2 into CO by H_2O over $Ag/SrNb_2O_6$. Due to the anisotropic property of $SrNb_2O_6$ nanorod, the Ag co-catalysts was selectively re-deposited on the top of $SrNb_2O_6$ nanorod during photoirradiation, although the Ag particles were uniformly loaded on the $SrNb_2O_6$ nanorod surface via a chemical reduction method. The separation of the reduction and oxidation sites was considered to be crucial for the highly active and selective photocatalytic conversion of CO_2 into CO with water as an electron donor.

In chapter 2, the photocatalytic performance for the conversion of CO_2 over $Ag/SrNb_2O_6$ with various bicarbonate salts as carbon sources was investigated. The selectivity toward CO evolution was higher than 87% for the photocatalytic conversion of CO_2 with bicarbonate salts as additives. Notably, the formation rate of CO was as high as 287 μmol h^{-1} with a selectivity toward CO evolution of higher than 94.1% when NH_4HCO_3 was used as an additive under the bubbling of Ar instead of CO_2. The formation rate of CO showed a good correspondence with [CO_2(aq)], indicating that the CO_2(aq) obtained by the dissociation of HCO_3^- was the actual reactant for the photocatalytic conversion of CO_2. In contrast, the HCO_3^- species in the aqueous solution was beneficial for improving the photocatalytic activity and selectivity toward CO evolution by increasing the adsorption of carbon-related species on the surface of the photocatalyst and/or suppressing the backward reaction for the photocatalytic conversion of CO_2.

Chapter 3 presents that a core-shell structured Ag-Cr dual co-catalyst loaded-Ga_2O_3 showed much

higher formation rate of CO (480 μmol h^{-1}) and selectivity toward CO evolution (83.8%) for the photocatalytic conversion of CO_2, as compared to that of bare Ga_2O_3, Ag/Ga_2O_3, Cr/Ga_2O_3 and other Ag-metals/Ga_2O_3. Stoichiometric amounts of CO and H_2 as reduction products, and O_2 as oxidation product were obtained, which indicated that H_2O functioned as an electron donor for the photocatalytic conversion of CO_2. An isotopic labeling experiment using $^{13}CO_2$ confirmed that the CO evolution originated from the CO_2 introduced in the gas phase rather than residual carbon contaminants. The modification of Ga_2O_3 by Cr species provided a thin layer of Cr_2O_3 on the surface of the Ag co-catalyst, which drastically suppressed the backward reaction ($CO + O_2 \rightarrow CO_2$) during the photocatalytic conversion of CO_2 by H_2O.

Chapter 4 describes the effects of Ag and Cr species on the photocatalytic conversion of CO_2 by H_2O over Ag@Cr/Ga_2O_3. Ag worked as an active site for the photocatalytic conversion of CO_2 into CO, exhibiting better photocatalytic performance than other metals, such as Au, Pt, Cu, and Pd. Notably, the $Cr(OH)_3{\cdot}xH_2O$ layer on the surface of Ag@Cr/Ga_2O_3 changed to $Cr(OH)_x(CO_3)_y$ during the photocatalytic conversion of CO_2, which increased the CO_2 adsorption on the Ag active sites. Furthermore, it was found that the most critical factor in the stated reaction was to ensure that the Ag particles were surrounded by a Cr shell of suitable thickness. The highest photocatalytic activity (525.3 μmol h^{-1}) with good selectivity toward CO evolution (85.2%) and high $TON_{CO/Ag}$ (167/5 h) was achieved over 0.25 mol% Ag@Cr/Ga_2O_3. In addition to Ga_2O_3, the Ag@Cr co-catalyst modification strategy could also be applied to other photocatalyst materials such as $NaTaO_3$, $ZnGa_2O_4$, and $ZnGa_2O_4$/Ga_2O_3 for the highly effective photocatalytic conversion of CO_2 to CO when using H_2O as an electron donor.

In Chapter 5, the effects of Cr species on photocatalytic stability during the conversion of CO_2 by H_2O were demonstrated. It was suggested that the formation rate of CO steadily decreased with the increasing of photoirradiation time. Cr^{3+} in Ag@Cr/Ga_2O_3 was oxidized to soluble Cr^{6+} during the photocatalytic conversion of CO_2 in a $NaHCO_3$ aqueous solution under UV light irradiation, which led to a decrease in the thickness of the $Cr(OH)_3{\cdot}xH_2O$ shell. Based on the results in chapter 4, the $Cr(OH)_x(CO_3)_y$ shell with suitable thickness was critical to ensure the high formation rate of CO, therefore, the decrease in the formation rate of CO for the photocatalytic conversion of CO_2 by H_2O was attributed to the dissolution Cr^{3+} in Ag@Cr/Ga_2O_3.

In chapter 6, a very high formation rate of CO (835 μmol h^{-1}) with high selectivity (94.5%) was achieved for the photocatalytic conversion of CO_2 by H_2O over calcium modified Ga_2O_3 with Ag@Cr as a co-catalyst. It was found that both CaO and $CaGa_4O_7$ were generated on the Ga_2O_3 surface when the modification amount of calcium was low. CaO greatly increased the CO_2 adsorption on Ga_2O_3, consequently, the formation rate of CO was enhanced and the formation of H_2 was suppressed for the photocatalytic conversion of CO_2 by H_2O in this case. However, excessive Ca modification caused only $CaGa_4O_7$ loaded on the Ga_2O_3 surface, which decreased the formation rate of CO and selectivity toward CO evolution because H_2 was the main product for the photocatalytic conversion of CO_2 by H_2O over Ag@Cr/$CaGa_4O_7$.

In summary, the morphology, crystal facet, and surface compositions of photocatalyst, the co-catalysts loaded on the photocatalyst, and the additives in the reaction solution have great influence on the activity, selectivity, and stability for the photocatalytic conversion of CO_2. Photocatalyst with special structure such as nanorod (chapter 1 and 2), loading suitable co-catalyst such as Ag@Cr dual co-catalyst (chapter 3 and 4), and surface modification of CO_2 absorbers (such as CaO) on photocatalyst (chapter 6) are found to achieve the enhancement of photocatalytic activity and selectivity toward CO evolution for the conversion of CO_2 by H_2O. Moreover, it should be noted that although additives such as $NaHCO_3$ is beneficial for improving the photocatalytic activity and selectivity by increasing the adsorption of carbon-related species on the photocatalyst and/or suppressing the backward reaction for the photocatalytic conversion of CO_2, it may also react with the catalyst and/or co-catalyst to affect the photocatalytic activity and stability for the conversion of CO_2 in an aqueous solution (chapter 2 and 5).

List of publications

Chapter 1

1. Highly selective photocatalytic conversion of CO_2 by water over Ag-loaded $SrNb_2O_6$ nanorods
   Rui Pang, Kentaro Teramura, Hiroyuki Asakura, Saburo Hosokawa, and Tsunehiro Tanaka.
   Applied Catalysis B Environmental, 2017, **218**, 770-778.

Chapter 2

2. Evaluation of intermediate species for the photocatalytic conversion of CO_2 with bicarbonate as a carbon source over $Ag/SrNb_2O_6$
   Rui Pang, Kentaro Teramura, Hiroyuki Asakura, Saburo Hosokawa, and Tsunehiro Tanaka.
   ACS applied Energy Materials, submitted.

Chapter 3

3. Modification of Ga_2O_3 by Ag-Cr core-shell cocatalyst enhances photocatalytic CO evolution for the conversion of CO_2 by H_2O
   Rui Pang, Kentaro Teramura, Hiroyuki Tatsumi, Hiroyuki Asakura, Saburo Hosokawa, and Tsunehiro Tanaka.
   Chemical Communications, 2018, **54**, 1053-1056.

Chapter 4

4. Chromium hydroxide layer on Ag cocatalyst surface for highly selective photocatalytic conversion of CO_2 by H_2O
   Rui Pang, Kentaro Teramura, Hiroyuki Asakura, Saburo Hosokawa, and Tsunehiro Tanaka.
   ACS Sustainable Chemistry & Engineering, 2019, **7**, 2083-2090.

Chapter 5

5. Effect of Cr species on photocatalytic stability during the conversion of CO_2 by H_2O
   Rui Pang, Kentaro Teramura, Hiroyuki Asakura, Saburo Hosokawa, and Tsunehiro Tanaka.

The Journal of Physical Chemistry C, 2019, **123**, 2894-2899.

Chapter 6

6. Remarkably enhancement of CO evolution by a calcium modification technique for photocatalytic conversion of CO_2 by H_2O

   Rui Pang, Kentaro Teramura, Hiroyuki Asakura, Saburo Hosokawa, and Tsunehiro Tanaka.

   Journal of the American Chemical Society, to be submitted.